Cell

Sympathetic-epithelial crosstalk governs tissue-resident memory T cell immunosurveillance in the skin

Graphical abstract

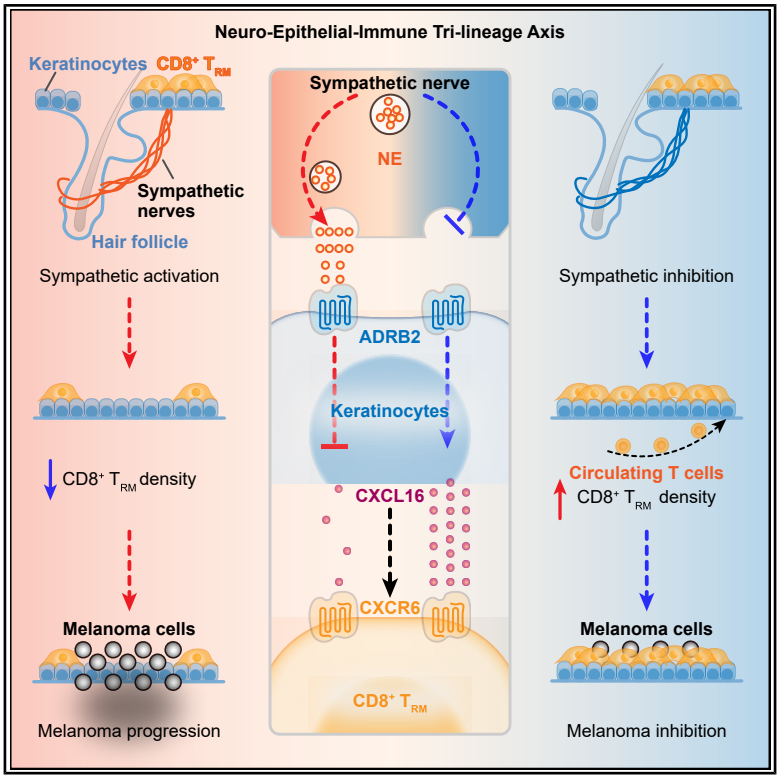

Highlights

- Sympathetic nerves regulate skin CD8$^+$ T_{RM} cell density by targeting keratinocytes
- Norepinephrine-ADRB2 signaling restricts the formation of CD8$^+$ T_{RM} cells
- Epithelial CXCL16 orchestrates CD8$^+$ T_{RM} recruitment and positioning in the skin
- This neuro-epithelial axis can tune regional immunosurveillance against melanoma

Authors

Peng Zhang, Juju Miao, Haoyue Yu, ..., Ping Yang, Ting Zhou, Bing Zhang

Correspondence

zhouting@westlake.edu.cn (T.Z.), zhangbing@westlake.edu.cn (B.Z.)

In brief

Sympathetic nerves regulate skin immunity by engaging keratinocytes to modulate the density of tissue-resident memory T cells. This neuro-epithelial axis can enable the nervous system to dynamically tune local immunosurveillance in barrier tissues against emerging cancers.

Zhang et al., 2026, Cell *189*, 1323–1340
March 5, 2026
https://doi.org/10.1016/j.cell.2025.12.043

Cell

CellPress

Article

Sympathetic-epithelial crosstalk governs tissue-resident memory T cell immunosurveillance in the skin

Peng Zhang,[1,3,5,8] Juju Miao,[2,4,8] Haoyue Yu,[1,3] Hualin Yu,[1,3] Chao Liu,[1,3] Luming Zhao,[2,3] Ping Yang,[7] Ting Zhou,[2,3,*] and Bing Zhang[1,3,5,6,9,*]

[1]School of Life Sciences, Westlake University, Hangzhou, Zhejiang, China
[2]School of Medicine, Westlake University, Hangzhou, Zhejiang, China
[3]Westlake Laboratory of Life Sciences and Biomedicine, Hangzhou, Zhejiang, China
[4]Fudan University Shanghai, Shanghai, China
[5]Research Center for Industries of the Future, Westlake University, Hangzhou, Zhejiang, China
[6]Shenzhen Medical Academy of Research and Translation (SMART), Shenzhen, China
[7]Department of Dermatology-Venereology, Affiliated Hangzhou First People's Hospital, School of Medicine, Westlake University, Hangzhou, Zhejiang, China
[8]These authors contributed equally
[9]Lead contact
*Correspondence: zhouting@westlake.edu.cn (T.Z.), zhangbing@westlake.edu.cn (B.Z.)
https://doi.org/10.1016/j.cell.2025.12.043

SUMMARY

Effective host defense and immunosurveillance at barrier tissues require coordinated functions of multiple cell types. Here, we show that in the skin, sympathetic nerves engage with epidermal keratinocytes to regulate the local density of tissue-resident memory CD8$^+$ T (T_{RM}) cells, thereby influencing regional cancer immunosurveillance. Sympathetic nerves do not communicate directly with CD8$^+$ T_{RM} cells. Instead, they form synapse-like structures near basal keratinocytes and dynamically modulate epithelial-derived signals essential for skin CD8$^+$ T_{RM} formation via norepinephrine-ADRB2 signaling. Reduced sympathetic tone elevates epithelial-derived signals to promote CD8$^+$ T_{RM} development in the skin epithelium, while heightened sympathetic activity during acute stress dampens this process. Our findings unveil a neuro-epithelial-immune tri-lineage axis that calibrates local CD8$^+$ T_{RM} abundance in the skin, enabling rapid adjustment of immunosurveillance strength at the barrier interface by inputs from the sympathetic nervous system.

INTRODUCTION

Barrier tissue immunity is orchestrated by a dynamic interplay between static structural components and motile immune cells. Epithelial cells establish a physical barrier and relay signals to underlying tissues, while immune cells continuously surveil these interfaces. Nerves, which densely innervate barrier tissues and convey both sensory and autonomic signals, have emerged as critical regulators of epithelial integrity and immune surveillance.[1,2] Through bidirectional communication with epithelial and immune cells, the nervous system helps maintain tissue homeostasis and orchestrates adaptive responses to physiological changes or pathogenic insults.[3–5] However, the mechanisms underlying the cooperation of these three lineages, epithelial, immune, and neural, during homeostasis and disease remain largely unknown.

Skin-resident memory CD8$^+$ T (T_{RM}) cells are key immune sentinels predominantly stationed within skin epithelial compartments throughout the body.[6–10] They originate as antigen-activated effector T cells (T_{EFF}) in lymphoid organs in response to commensal microbiota, pathogens, or malignant cells. A subset of these T_{EFF} subsequently migrates to the skin, guided by tissue-homing chemokines and adhesion molecules.[11,12] Once in the skin, these cells receive local signals such as transforming growth factor beta (TGF-β) and interleukin-15 (IL-15), which trigger metabolic reprogramming and upregulation of residency markers CD69, integrin αE (CD103), and α1 (CD49a), thereby establishing residency.[12–15] CD8$^+$ T_{RM} cells lodge in the interfollicular epidermis and upper hair follicles, where they rapidly secrete effector cytokines like tumor necrosis factor-alpha (TNF-α) and interferon-gamma (IFN-γ) upon local antigen re-encounter or other inflammatory stimuli.[16] Through this "sense-and-alarm" mechanism, T_{RM} cells not only execute immediate protective functions but also amplify local immune responses by recruiting and activating other immune cells.[16–18] The protective capacity of T_{RM} cells is closely tied to their abundance. An ample T_{RM} pool provides robust local immunity, whereas insufficient T_{RM} can permit pathogen dissemination or tumor progression.[19–21]

Recent findings underscore the crucial role of CD8$^+$ T_{RM} cells in cancer immunosurveillance, particularly in restraining early-stage melanomas.[22,23] Consistent with this, higher densities of CD69$^+$ CD103$^+$ CD8$^+$ T_{RM}-like cells within human tumors are often associated with improved patient outcomes.[24,25] Despite these, the epithelial and neural signals influencing the abundance and strategic positioning of skin CD8$^+$ T_{RM} cells remain elusive.

The peripheral nervous system is increasingly recognized as a pivotal orchestrator of immune responses at barrier sites such as the gut, lungs, and skin.[26–30] At these interfaces, diverse sensory and sympathetic nerve fibers closely interact with immune cells to modulate inflammation and maintain tissue homeostasis.[31–35] However, it remains unclear whether CD8$^+$ T_{RM} cells are subject to neural regulation. Peripheral nerves release neurotransmitters and neuropeptides, such as acetylcholine and calcitonin gene-related peptide (CGRP), which can bind to receptors on immune cells to regulate their function.[36] Nevertheless, it is unknown whether T_{RM} cells themselves directly receive such neural signals. Furthermore, as neuronal outputs respond rapidly to environmental and physiological changes, how these signals impact T_{RM} cell dynamics and local immunosurveillance in barrier tissues remains unknown.

In this study, we investigated how epithelial, immune, and neural signals integrate to coordinate barrier tissue immunity in the skin. We found that cutaneous sympathetic nerves interact closely with epidermal keratinocytes but rarely directly contact CD8$^+$ T_{RM} cells. These sympathetic fibers form synapse-like structures near the basal layer of epidermis and modulate epithelial-derived molecular signals that orchestrate CD8$^+$ T_{RM} cell recruitment and positioning in the skin barrier. Through this indirect mechanism, sympathetic nerves calibrate the size of the T_{RM} cell pool in the skin and consequently tune local immunosurveillance against nascent cancer cells. Our findings highlight a synergistic interaction between the nervous and immune systems mediated by skin epithelium, revealing a neuro-epithelial-immune axis that adjusts tissue immunosurveillance strength according to systemic neural inputs. Elucidating this mechanism is crucial for understanding regionalized immunosurveillance and the earlier steps of tumor development in tissues. These insights could also inform new strategies such as transient regional nerve blockade or topical adrenergic antagonists to boost long-lived T_{RM} protection against infections or to enhance immune containment of emerging cancers.[37–39]

RESULTS

Sympathetic nerve inhibition dramatically increases skin CD8$^+$ T_{RM} cells

To investigate whether skin CD8$^+$ T_{RM} cells are influenced by peripheral nerve signals in mice, we first examined their distribution relative to epithelial cells and sympathetic nerves, a major peripheral nerve type in the skin. Immunofluorescence staining confirmed that CD8$^+$ T_{RM} cells were predominantly located in the interfollicular epidermis and upper hair follicles (~90%),[40–42] without direct contact with sympathetic nerves (Figure 1A). Flow cytometry analysis confirmed that most of these CD8$^+$ T cells expressed skin T_{RM} markers such as CD69 and CD103, along with TNF-α and IFN-γ[12] (Figures 1B and S1A). Whole-mount immunofluorescence staining further illustrated dense networks of sympathetic innervation throughout the skin epithelium, where CD8$^+$ T_{RM} cells were interspersed (Figure 1C). To examine whether cutaneous sympathetic signals affect CD8$^+$ T_{RM} cells, we used 6-hydroxydopamine (6-OHDA, a selective neurotoxin) to eliminate sympathetic nerves in the skin[43] (Figure S1B). Sympathetic ablation significantly increased CD8$^+$ T_{RM} cell numbers in the skin (Figure 1D). This increase was most pronounced in the epidermal compartments, with a modest rise in the dermis (Figure 1E). T_{RM} cell numbers remained elevated for at least 6 weeks while sympathetic nerves were absent (Figures 1E, S1C, and S1D) and then gradually declined by 14 weeks as sympathetic fibers started to reinnervate the skin (Figures S1E and S1F). A similar CD8$^+$ T_{RM} increase was observed following genetic sympathetic nerve ablation using *DBH^{Cre}; ROSA^{iDTR}* mice (Figure S1G). CD8$^+$ T_{RM} increase was consistent in both male and female mice and evident in aged mice (Figures S1H and S1I). Furthermore, sympathetic ablation did not significantly alter local levels of acetylcholine, CGRP, or serotonin in the skin (Figures S1J and S1K). Moreover, ablating cutaneous sensory nerves using *TRPV1^{Cre}; ROSA^{iDTR}* mice or *Nav1.8^{Cre}; ROSA^{iDTR}* mice did not affect skin CD8$^+$ T_{RM} cell numbers (Figures S1L and S1M). Together, these data suggest that cutaneous sympathetic nerves, though not directly touching CD8$^+$ T_{RM} cells, play an important role in regulating their abundance.

To determine whether neuronal signals from sympathetic nerves affect skin CD8$^+$ T_{RM} cells, we utilized a chemogenetic approach with the DREADDs (designer receptors exclusively activated by designer drugs) system.[44,45] We generated *DBH^{Cre}; R26-LSL-Gi-DREADD* mice (Gi-DREADD), in which the engineered $G\alpha_i$/o-protein-coupled receptor is expressed in sympathetic neurons and inhibits their activity upon administration of clozapine N-oxide (CNO) (Figures 2A and S2A). Systemic sympathetic inhibition via intraperitoneal CNO injection induced a rapid increase in skin CD8$^+$ T cells (Figure 2B). This effect was transient, with CD8$^+$ T cells in both the epidermis and dermis rising significantly within 2 days after the initial CNO administration, remaining elevated for approximately 1 week, and returning to baseline by 2 weeks (Figures 2C, S2B, and S2C). Flow cytometry confirmed that the expanded population consisted predominantly of CD69$^+$ CD103$^+$ CD8$^+$ T_{RM} cells (Figures 2D and S2D–S2F). These T_{RM} cells were functionally competent, expressing normal levels of effector molecules (IFN-γ, TNF-α, and granzyme B) without changes in exhaustion markers (PD-1 and TIM-3) (Figures S2G and S2H). Meanwhile, other major cutaneous immune populations were largely unchanged (Figure S2I). To further characterize these T_{RM} cells, we fluorescence-activated cell sorting (FACS)-purified T cells from the back skin of control and Gi-DREADD mice and performed 10× Chromium single-cell RNA sequencing. Transcriptomic analysis confirmed that CD8$^+$ T_{RM} cells constituted the dominant population among all T cells in both control and Gi-DREADD mice, showing high expression of canonical residency markers and transcription factors, such as *Cd69*, *Itgae* (CD103), *Znf683* (Hobit), *Cxcr6*, *Itgal* (LFA-1), and *Nr4a1*, along with low levels of *Ccr7*, *Klrg1* (killer cell lectin-like receptor G1), *Sell* (CD62L), and *S1pr1* (Figures 2E, S2J, and S2K).[13,46–49] Direct comparison showed no significant

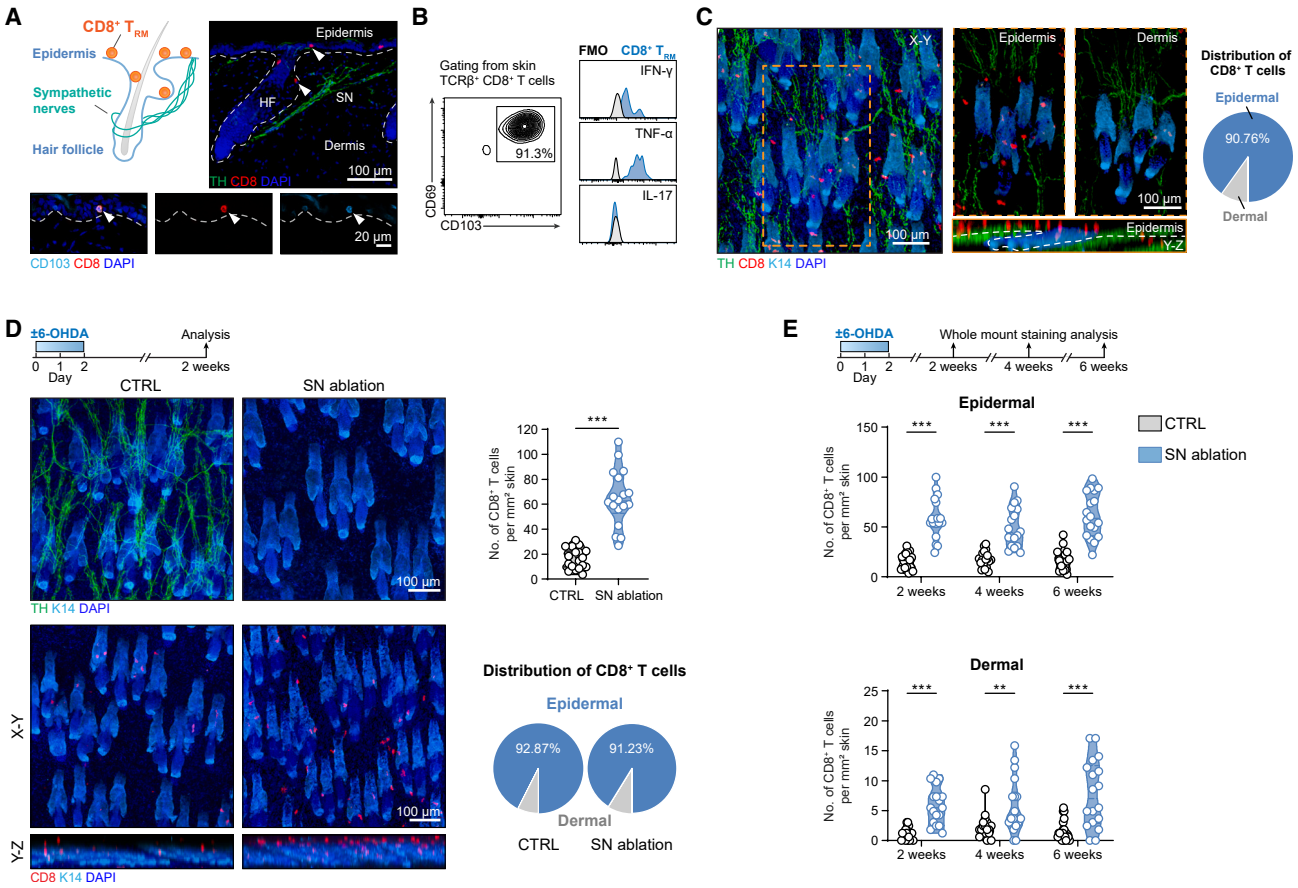

Figure 1. Ablation of sympathetic nerves increases CD8$^+$ T_{RM} cells in skin

(A) Schematic and immunofluorescence staining for sympathetic nerves (SNs) and CD8$^+$ T_{RM} cells in mouse back skin. Antibodies stained: tyrosine hydroxylase (TH, green, a marker for SN), CD8 (red), and CD103 (light blue, a marker for T_{RM} cells). HFs, hair follicles.

(B) Flow cytometry analysis of skin CD8$^+$ T_{RM} cells for TNF-α, IFN-γ, and IL-17.

(C) Whole-mount staining of SN and CD8$^+$ T cells in mouse back skin. Right: distribution of CD8$^+$ T cells in the epidermis and dermis (n = 56 skin areas from 9 mice). K14, keratin 14.

(D) Whole-mount staining of SN and CD8$^+$ T cells in the skin of control and 6-OHDA-treated mice (SN ablation), with quantification and distribution of CD8$^+$ T cells (n = 18 skin areas from 3 mice per group, two-tailed unpaired t test).

(E) Quantification of epidermal and dermal CD8$^+$ T cells at 2, 4, and 6 weeks after SN ablation (n = 18 skin areas from 3 mice per group, two-way ANOVA). Violin plots show the distribution with individual data points; horizontal lines indicate the median and interquartile range; $^{**}p < 0.01$, $^{***}p < 0.001$.

See also Figure S1.

differences in core functional or exhaustion-related gene expression between CD8$^+$ T_{RM} cells from control and Gi-DREADD mice (Figure S2K). Moreover, they clustered together with previously identified skin CD8$^+$ T_{RM} cells in single-cell RNA sequencing (scRNA-seq) datasets[50] and displayed transcriptomic signatures resembling T_{RM} cells, rather than naive or effector T cells (Figure S2L). Together, chemogenetic sympathetic silencing causes a reversible surge in skin CD8$^+$ T_{RM} cells without overtly altering their identity or functional state.

We next asked whether the increase in CD8$^+$ T_{RM} cells depends on local sympathetic signals in the skin rather than systemic effects. To address this, we intradermally injected CNO into a small area on the back of Gi-DREADD mice,[43] while injecting saline into a mirrored area on the opposite side as a control (Figure 2F). In these mice, local CNO delivery led to a significantly higher density of CD8$^+$ T_{RM} cells at the CNO-injected site compared with the saline-injected site (Figure 2F). This demonstrates that inhibiting sympathetic signals locally in the skin is sufficient to increase the CD8$^+$ T_{RM} population (Figure 2G).

Sympathetic-epithelial communication regulates local CD8$^+$ T_{RM} cell abundance

As part of the autonomic nervous system, the sympathetic nervous system maintains tonic activity to support essential life activities such as heart rate and blood flow.[51] Sympathetic nerves release norepinephrine (NE), which binds to adrenergic receptors on target cells and activates downstream signaling pathways that regulate various cellular processes (Figure 3A). To test whether inhibiting NE-adrenergic receptor signaling locally in the skin mimics the effects of sympathetic inhibition on CD8$^+$ T_{RM} cells, we administered nadolol, a β blocker targeting both β1- and β2-adrenergic receptors, intradermally into one side of

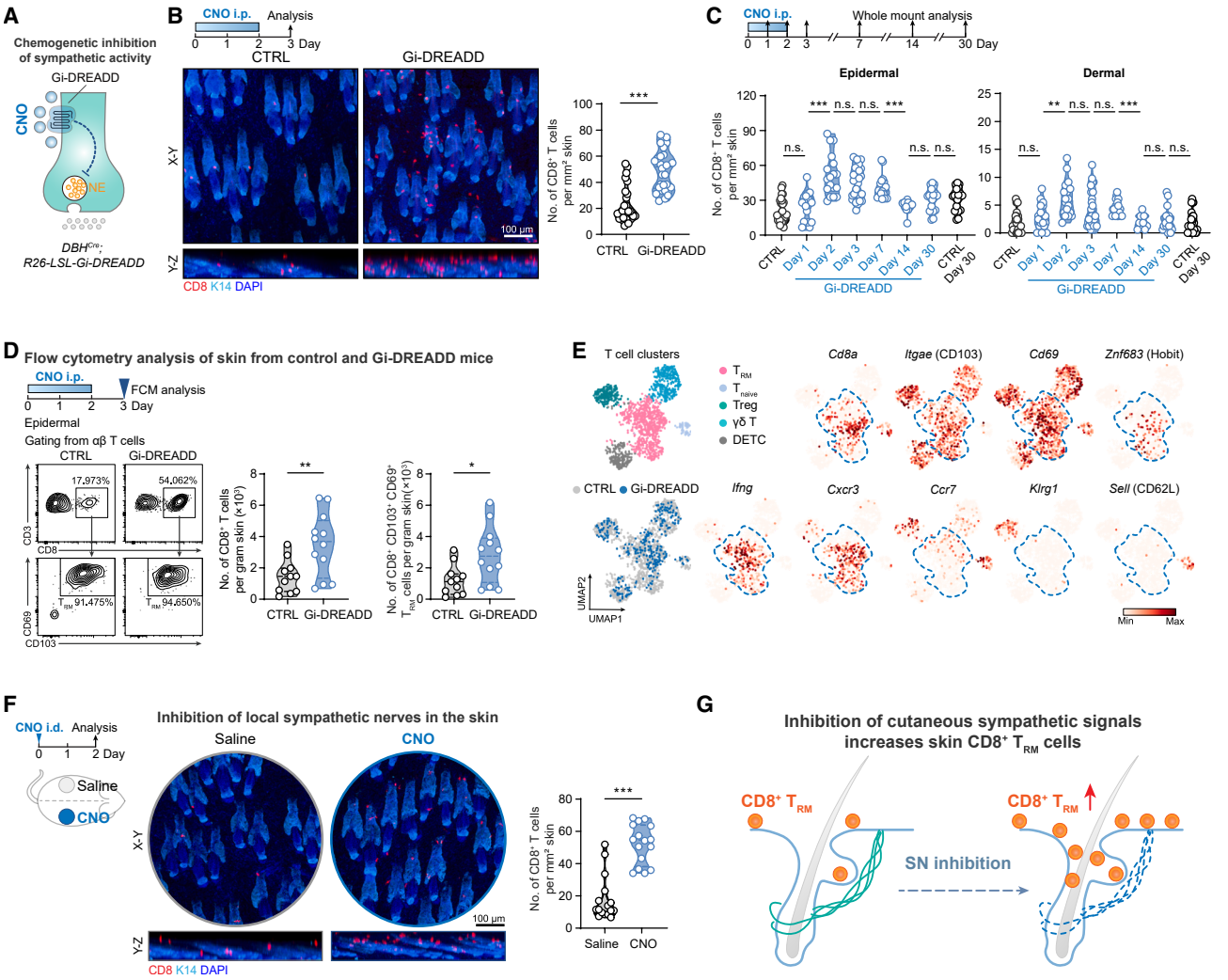

Figure 2. Inhibition of cutaneous sympathetic signals expands the skin CD8$^+$ T_{RM} cell pool

(A) Schematic of sympathetic inhibition using Gi-DREADD.

(B) Whole-mount staining and quantification of skin CD8$^+$ T cells in control and Gi-DREADD mice (n = 26–34 skin areas from 6–7 mice per group, two-tailed unpaired t test).

(C) Quantification of epidermal and dermal CD8$^+$ T cells in control and Gi-DREADD mice after CNO administration (n = 10–34 skin areas from 2–7 mice per group, two-tailed unpaired t test).

(D) Representative flow cytometry plots and quantification of epidermal CD8$^+$ T and T_{RM} cells in control and Gi-DREADD mice (n = 11–12 mice per group, two-tailed unpaired t test).

(E) scRNA-seq uniform manifold approximation and projection (UMAP) visualization and marker expression of T cell subsets isolated from the skin of control and Gi-DREADD mice (4 experimental replicates per group). T_{naive}, naive T cells; DETC, dendritic epidermal T cells; Treg, regulatory T cells.

(F) Whole-mount staining and quantification of CD8$^+$ T cells at intradermal injection sites of saline or CNO in Gi-DREADD mice (n = 16 skin areas from 3 mice per group, two-tailed unpaired t test).

(G) Schematic diagram illustrating that inhibiting cutaneous SN signals increases CD8$^+$ T_{RM} cells in the skin.

Violin plots show the distribution with individual data points; horizontal lines indicate the median and interquartile range; *$p < 0.05$, **$p < 0.01$, ***$p < 0.001$; n.s., not significant.

See also Figure S2.

the back skin. Nadolol treatment significantly increased CD8$^+$ T_{RM} cell numbers at the injected sites compared with contralateral saline-injected sites (Figure 3B). Like our chemogenetic experiments, this effect was also transient, with CD8$^+$ T_{RM} cells rising shortly after treatment and returning to baseline within approximately 1 week (Figure S3A). Conversely, blocking α-adrenergic receptor signaling in the skin did not alter local CD8$^+$ T_{RM} cell abundance (Figure S3B). These findings indicate that local NE signaling through β-adrenergic receptors constrains CD8$^+$ T_{RM} cell accumulation in the skin.

To identify the direct cellular target of NE in the skin responsible for modulating CD8$^+$ T_{RM} cells, we analyzed adrenergic

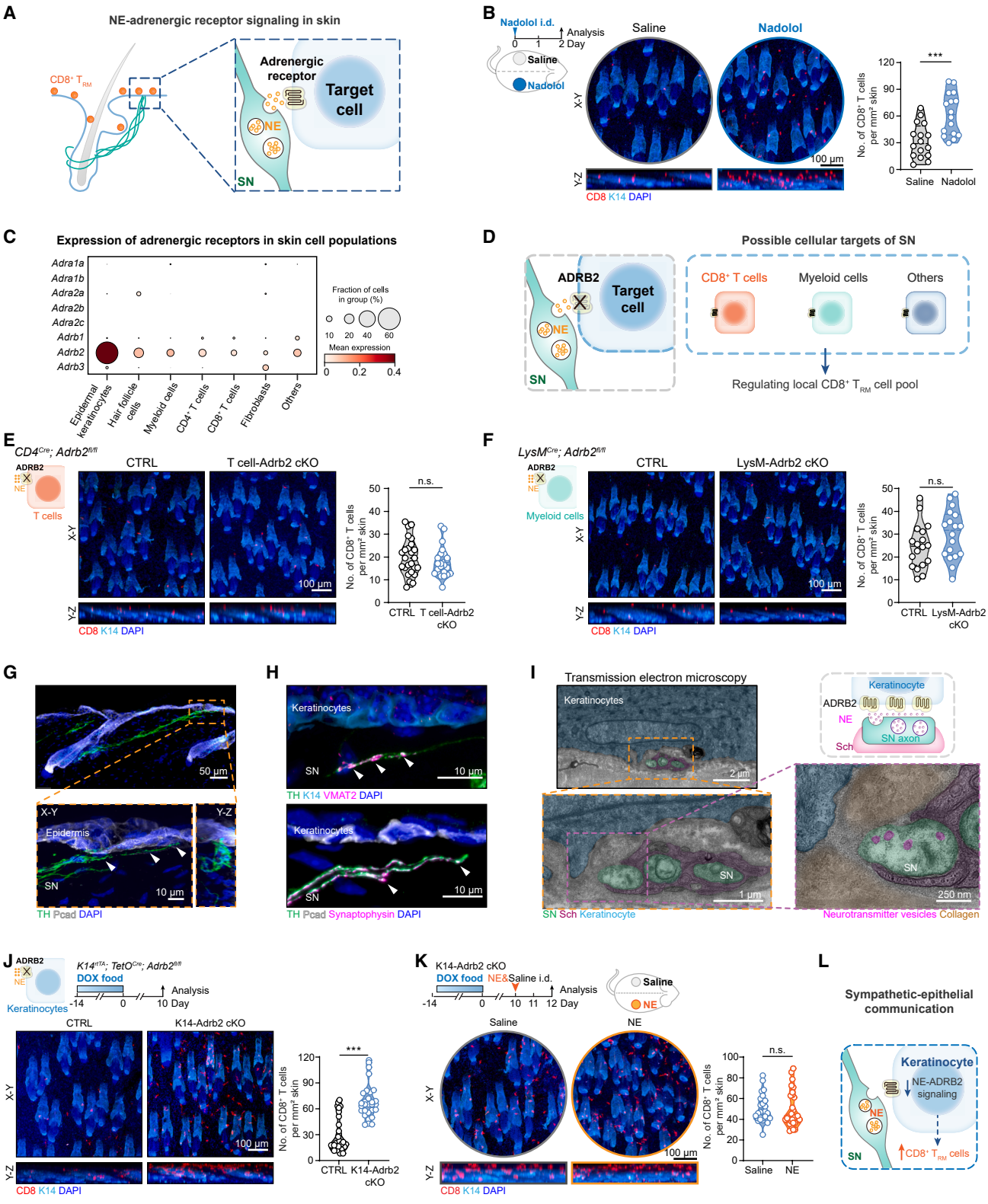

Figure 3. Sympathetic-epithelial communication governs local CD8$^+$ T_{RM} cell abundance

(A) Schematic of sympathetic regulation.

(B) Skin CD8$^+$ T cells after intradermal nadolol injection (n = 16 skin areas from 3 mice per group, two-tailed unpaired t test).

(legend continued on next page)

receptor expression across major skin cell types in mice using scRNA-seq (Figures S3C and S3D). Our results revealed the β2-adrenergic receptor (*Adrb2*) being most prominent (Figure 3C). We initially hypothesized that NE acts directly on immune cells through ADRB2 signaling to modulate CD8$^+$ T_{RM} cells. To test this, we systematically deleted *Adrb2* from distinct skin immune cell populations and examined whether this phenocopied sympathetic inhibition (Figure 3D). However, conditional *Adrb2* deletion in T cells using *CD4^{Cre}; Adrb2$^{fl/fl}$* mice,[52] regulatory T cells using *Foxp3^{Cre}; Adrb2$^{fl/fl}$* mice, dendritic cells using *CD11c^{Cre}; Adrb2$^{fl/fl}$* mice, or other myeloid populations using *LysM^{Cre}; Adrb2$^{fl/fl}$* mice (targeting primarily monocytes, macrophages, and neutrophils) did not alter skin CD8$^+$ T_{RM} cell numbers (Figures 3E, 3F, S3E, and S3F). These results indicate that sympathetic signals do not regulate CD8$^+$ T_{RM} cell abundance by directly targeting T cells or indirectly through myeloid cells.

Adrb2 was expressed at the highest levels and frequencies in epidermal keratinocytes, including the basal and suprabasal cells, suggesting that the skin epithelium may be the key intermediary (Figures 3C, S3G, and S3H). Following this link, we found that cutaneous sympathetic nerves primarily reside between the interfollicular epidermis and hair follicles, with a distinct subset of sympathetic axons terminating near the basal layer of epidermis (Figures 3G and S3I). These axons were separate from those innervating arrector pili muscles, exhibited swellings resembling axonal varicosities that store neurotransmitters, and co-localized with presynaptic marker vesicular monoamine transporter 2 (VMAT2) and synaptophysin (Figures 3H and S3J). Transmission electron microscopy further revealed synaptic vesicles within these sympathetic nerve endings (Figure 3I). These observations suggest that sympathetic nerves form synapse-like structures near epidermal keratinocytes and are poised to release the neurotransmitter NE onto them.

To investigate whether NE-ADRB2 signaling between sympathetic nerves and epidermal keratinocytes regulates skin CD8$^+$ T_{RM} cell abundance, we generated *K14^{rtTA}; TetO^{Cre}; Adrb2$^{fl/fl}$* mice, which allow keratinocyte-specific deletion of *Adrb2* upon doxycycline induction. Deletion of *Adrb2* in epidermal keratinocytes significantly increased skin CD8$^+$ T_{RM} cells, phenocopying sympathetic inhibition (Figure 3J). Flow cytometry confirmed an expansion of CD69$^+$ CD103$^+$ CD8$^+$ T_{RM} cells in these mice (Figure S3K). Importantly, local supplementation of NE by intradermal injection failed to reverse the elevated T_{RM} cell numbers in *K14^{rtTA}; TetO^{Cre}; Adrb2$^{fl/fl}$* mice, confirming that the phenotype results specifically from loss of ADRB2 in keratinocytes (Figure 3K). To further define the specificity of this pathway, we deleted *Adrb2* in hair follicle cells (*Lhx2^{CreER}; Adrb2$^{fl/fl}$* mice) or dermal fibroblasts (*Pdgfra^{CreER}; Adrb2$^{fl/fl}$* mice) and found no changes in skin CD8$^+$ T_{RM} cell numbers (Figures S3L and S3M). Intravital imaging revealed that transient sympathetic inhibition did not markedly alter local skin blood flow (Figure S3N). Collectively, these results indicate that cutaneous sympathetic nerves regulate local CD8$^+$ T_{RM} cell abundance indirectly by signaling to epidermal keratinocytes through ADRB2 (Figure 3L).

Sympathetic inhibition enhances circulating T cell recruitment to the skin

Next, we investigated how reduced NE-ADRB2 signaling in skin epithelium increases T_{RM} cells. One possibility was that existing T_{RM} cells proliferate *in situ* when sympathetic tone is low[20] (Figure 4A). To test this, we labeled proliferating CD8$^+$ T_{RM} cells in control and Gi-DREADD mice over a 48-h period by administering 5-ethynyl-2′-deoxyuridine (EdU, a thymidine analog that incorporates into dividing cell DNA) intraperitoneally every 6 h following CNO injection. However, the percentage of EdU$^+$ CD8$^+$ T_{RM} cells remained unchanged (Figure 4B). Similarly, Ki-67 staining showed no significant changes in T_{RM} cell proliferation (Figure S4A). These data suggest that the observed increase in CD8$^+$ T_{RM} cells upon sympathetic inhibition is unlikely attributed to their enhanced proliferation locally in the skin.

CD8$^+$ T_{RM} cells develop from circulating T cells that enter peripheral tissues and then adapt to the tissue microenvironment.[12,53] We therefore asked whether sympathetic inhibition enhances the recruitment of T cells from circulation into the skin, thereby enlarging the T_{RM} pool. To directly track incoming T cells, we intravenously transferred equal numbers of carboxyfluorescein succinimidyl ester (CFSE)-labeled activated CD8$^+$ T cells from ovalbumin (OVA) plus Complete Freund's Adjuvant (CFA)-pulsed OT-1 donor mice into control and Gi-DREADD mice. CNO-induced sympathetic inhibition significantly increased the number of CFSE$^+$ CD8$^+$ T cells homing to the skin (Figures 4C, S4B, and S4C). Pre-treatment with nadolol before transfer produced a similar increase (Figures S4D and S4E), indicating that local β-adrenergic blockade is sufficient to boost T cell recruitment. Among transferred OT-1 cells that entered the skin, those in the epidermis expressed lower levels of KLRG1 than those in the

(C) Dot plot showing adrenergic receptor expression in major skin cell types from scRNA-seq analysis. The color density represents the mean log-normalized expression, and the dot size indicates the percentage of cells expressing the gene.
(D) Possible cellular mechanisms.
(E and F) Skin CD8$^+$ T cells in control, *CD4^{Cre}; Adrb2$^{fl/fl}$* (T cell-Adrb2 conditional knockout [cKO]), and *LysM^{Cre}; Adrb2$^{fl/fl}$* (LysM-Adrb2 cKO) mice (n = 18–25 skin areas from 3–4 mice per group, two-tailed unpaired t test).
(G) Immunofluorescence staining of SN and skin epithelium. Arrowheads indicate sympathetic axon endings near epidermal keratinocytes. Pcad, p-cadherin.
(H) Sympathetic axon endings colocalize with presynaptic markers vesicular monoamine transporter 2 (VMAT2, purple) and synaptophysin (purple) when approaching epidermal keratinocytes. Arrowheads indicate accumulation of VMAT2 and synaptophysin in axonal varicosities.
(I) Transmission electron microscopy images showing SN form synapse-like structures near basal keratinocytes. Sch, Schwann cells.
(J) Skin CD8$^+$ T cells in control and *K14^{rtTA}; TetO^{Cre}; Adrb2$^{fl/fl}$* (K14-Adrb2 cKO) mice (n = 30 skin areas from 5 mice per group, two-tailed unpaired t test).
(K) Skin CD8$^+$ T cells in K14-Adrb2 cKO mice following intradermal injection of saline or NE (n = 29 skin areas from 5 mice per group, two-tailed unpaired t test).
(L) Schematic of sympathetic-epithelial communication regulating T_{RM}.
Violin plots show the distribution with individual data points; horizontal lines indicate the median and interquartile range; ***$p < 0.001$; n.s., not significant.
See also Figure S3.

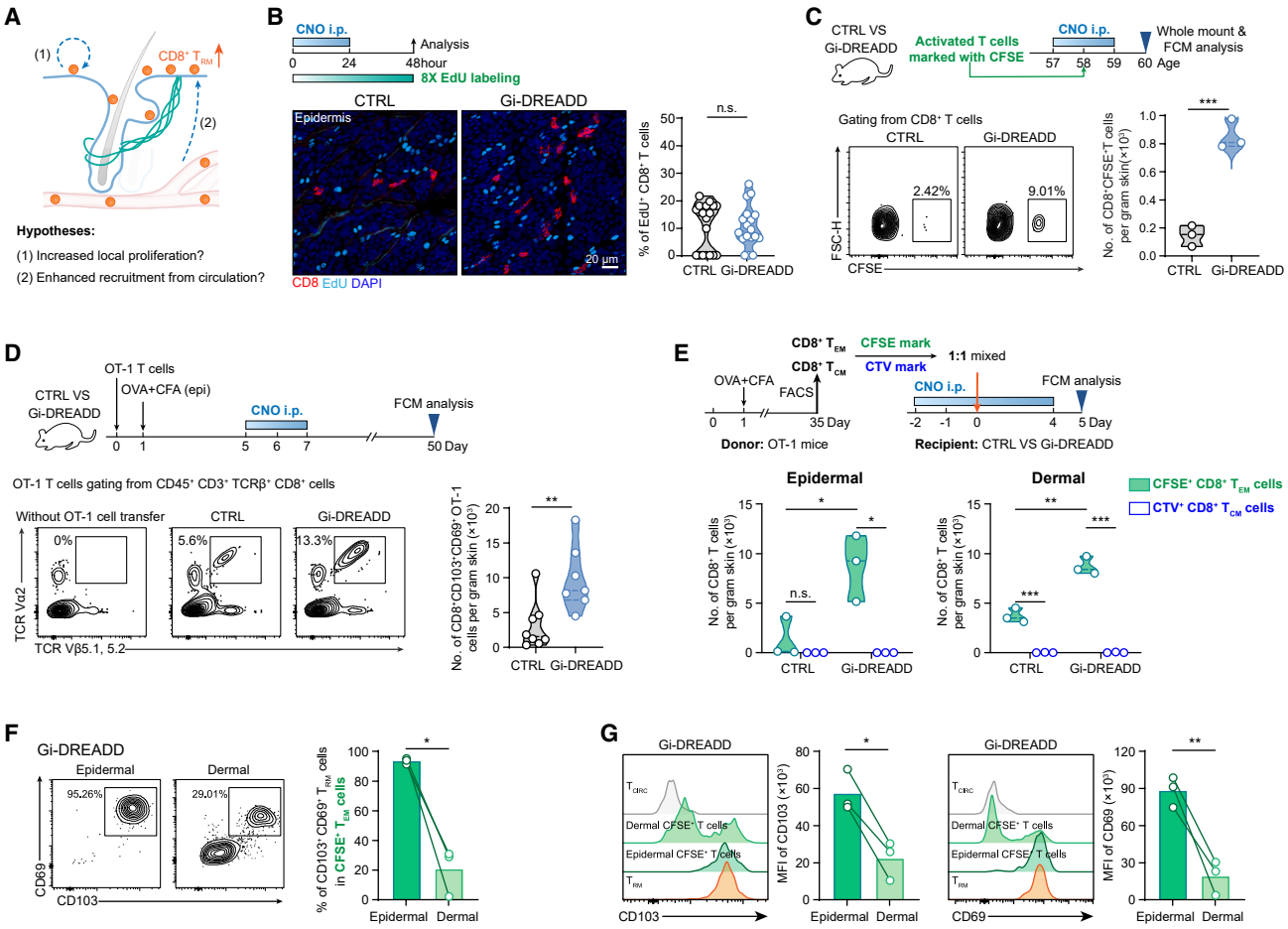

Figure 4. Sympathetic inhibition enhances the recruitment of circulating T cells to the skin

(A) Possible cellular mechanisms.

(B) EdU (light blue, labels proliferative cells) co-staining with CD8, with quantification of EdU-positive $CD8^+$ T cell percentage (n = 18 skin areas from 3 mice per group, two-tailed unpaired t test).

(C) Representative flow cytometry plots and quantification of $CFSE^+$ $CD8^+$ T cells in the skin of control and Gi-DREADD mice after CFSE-labeled activated $CD8^+$ T cell transfer and CNO treatment (n = 3 mice per group, unpaired two-tailed t test).

(D) Representative flow cytometry plots and quantification of OT-1 cells in the skin of control and Gi-DREADD mice after OT-1 cells transfer, OVA/CFA inoculation, and CNO treatment (n = 7–8 mice per group, two-tailed unpaired t test).

(E) Representative flow cytometry plots and quantification of $CFSE^+$ $CD8^+$ T_{EM} and CTV^+ T_{CM} cells in the epidermis and dermis of control and Gi-DREADD mice after adoptive co-transfer (n = 3 mice per group, two-tailed unpaired t test).

(F) Representative flow cytometry plots and quantification of $CD103^+$ $CD69^+$ $CFSE^+$ T cells in epidermis and dermis of Gi-DREADD mice (n = 3 mice per group, two-tailed unpaired t test).

(G) Representative flow cytometry histograms and mean fluorescence intensity (MFI) quantification of CD103 and CD69 expression on epidermal and dermal $CFSE^+$ $CD8^+$ T cells of Gi-DREADD mice (n = 3 mice per group, two-tailed unpaired t test).

Violin plots show the distribution with individual data points; horizontal lines indicate the median and interquartile range; $^*p < 0.05$, $^{**}p < 0.01$, $^{***}p < 0.001$; n.s., not significant.

See also Figure S4.

dermis (Figure S4F), consistent with the notion that epidermal entry is coupled to the acquisition of a tissue-resident memory phenotype.[12,54] To determine whether this transient enhanced recruitment promotes the formation of a durably larger pool of antigen-specific skin $CD8^+$ T_{RM} cells, we intravenously transferred equal numbers of naive OT-1 $CD8^+$ T cells into control and Gi-DREADD mice, then immunized both groups epicutaneously with OVA/CFA followed by CNO-mediated sympathetic inhibition.[23,55] 7 weeks post-inoculation, flow cytometry revealed a significant increase in OT-1 $CD8^+$ T_{RM} cells in the skin of Gi-DREADD mice (Figures 4D and S4G). Thus, transient blocking of cutaneous sympathetic signals during an active immune response drives the establishment of a larger, long-term pool of antigen-specific $CD8^+$ T_{RM} cells. Similar increases in OT-1 $CD8^+$ T_{RM} cells were observed in mice with sympathetic ablation (Figure S4H).

We also examined whether sympathetic tone differentially affects the recruitment of central memory (T_{CM}) and effector

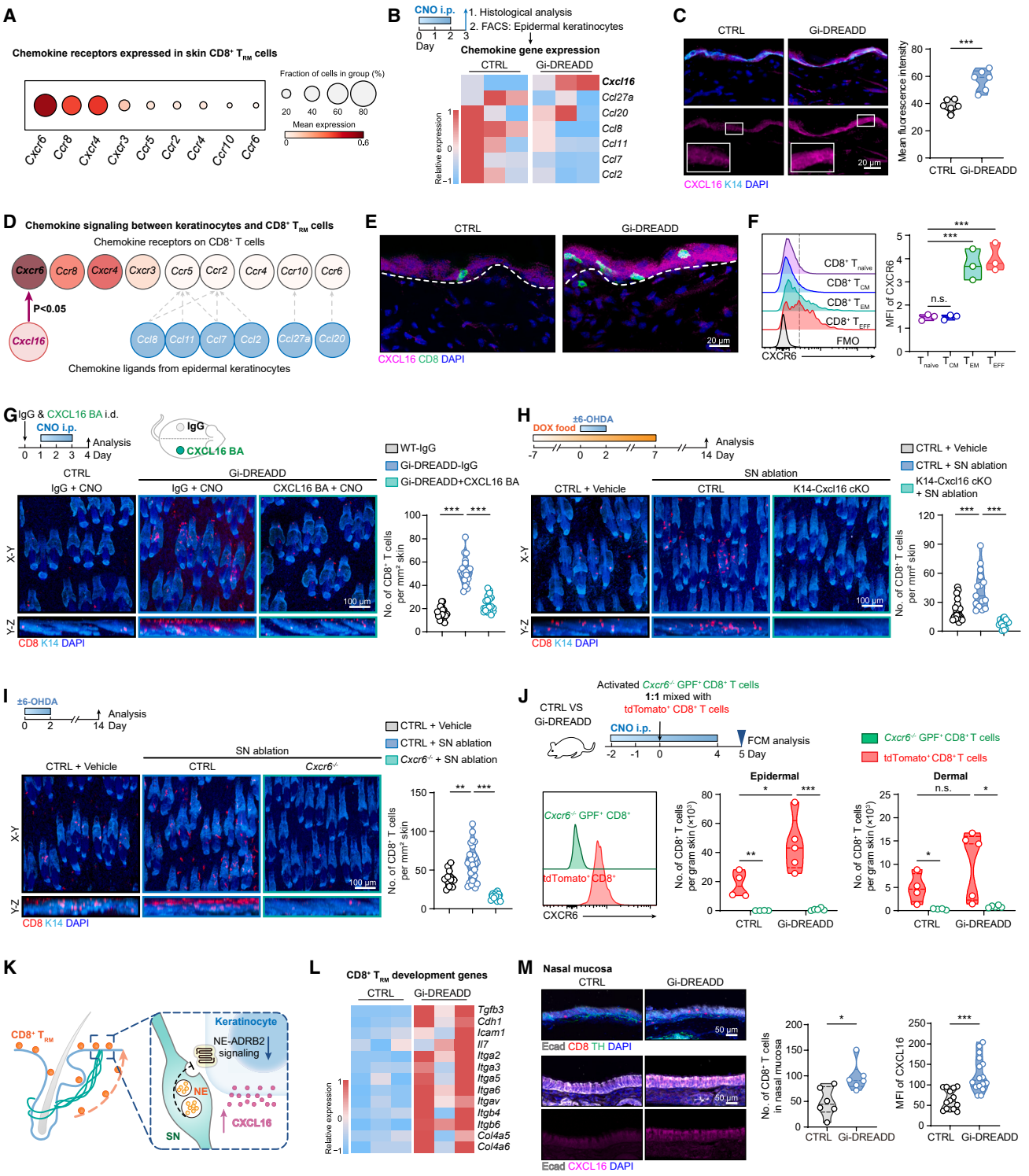

Figure 5. Epithelial-derived signals govern CD8$^+$ T_{RM} cell formation

(A) Dot plot of chemokine receptor gene expression in skin CD8$^+$ T_{RM} cells from scRNA-seq analysis.

(B) Heatmap of chemokine gene expression related to CD8$^+$ T cell recruitment in epidermal keratinocytes from control and Gi-DREADD mice.

(C) Immunofluorescence staining and MFI quantification of CXCL16 in the epidermis of control and Gi-DREADD mice ($n = 6$ skin areas, two-tailed unpaired t test).

(D) CellChat analysis of keratinocyte-expressed chemokines and T_{RM}-expressed chemokine receptors from scRNA-seq data.

(E) Co-staining of CD8 and CXCL16 in the skin of control and Gi-DREADD mice.

(legend continued on next page)

memory (T_{EM}) $CD8^+$ T cells. Purified OT-1 T_{CM} and T_{EM} cells were labeled with distinct dyes (CellTrace Violet, CTV, and CFSE, respectively) and co-transferred into recipient mice at a 1:1 ratio (Figures 4E, upper panels, and S4I). Sympathetic inhibition selectively increased T_{EM} recruitment into both the epidermis and dermis, whereas T_{CM} recruitment was minimal and unchanged (Figures 4E, S4J, and S4K). Recruited cells that entered the epidermis exhibited higher expression of canonical T_{RM} markers CD69 and CD103 compared with their dermal counterparts (Figures 4F, 4G, S4L, and S4M). In summary, inhibiting sympathetic signals enhances the recruitment of circulating T_{EFF} and T_{EM} cells to the skin and promotes their positioning within the epidermis, where they receive local cues to differentiate into T_{RM} cells.

Sympathetic inhibition increases epidermal CXCL16 to recruit and promote T_{RM} formation

T_{EFF} or T_{EM} cells enter barrier tissues through interactions between their migratory/homing receptors and tissue-specific chemokines, followed by maturation driven by tissue-specific molecular signals.[56–59] We reasoned that loss of ADRB2 signaling in keratinocytes might upregulate chemokines that attract circulating T cells and facilitate their retention. Our scRNA-seq data showed that skin $CD8^+$ T_{RM} cells express high levels of the chemokine receptor CXCR6,[48,60–62] among others (Figure 5A). Its ligand, CXCL16, can be produced by epithelial cells and exists in both soluble and membrane-tethered forms.[63] We asked whether sympathetic inhibition increases keratinocyte-derived CXCL16, thereby enhancing recruitment and positioning of $CD8^+$ T_{RM} cells in the epidermis. To test this, we FACS-purified keratinocytes from control and CNO-treated Gi-DREADD mice and performed RNA-seq (Figures S5A and S5B). *Cxcl16* transcripts increased approximately 2-fold in keratinocytes from CNO-treated skin compared with controls, while other chemokines decreased or remained unchanged (Figures 5B and S5C). Immunofluorescence staining and western blotting confirmed elevated CXCL16 protein (Figures 5C and S5D–S5F). The elevated CXCL16 was localized to keratinocytes in both basal and suprabasal layers, whereas other cell types in the skin, such as fibroblasts, endothelial cells, or dendritic cells,[64,65] showed little or no change in CXCL16 expression upon sympathetic inhibition (Figures S5G–S5I).

Multiple lines of evidence supported the importance of an enhanced CXCL16-CXCR6 axis in mediating $CD8^+$ T_{RM} recruitment following sympathetic inhibition. First, CellChat analysis of cell-cell communication revealed augmented CXCL16-CXCR6 signaling from epidermal keratinocytes to $CD8^+$ T_{RM} cells in sympathetically inhibited skin (Figure 5D). Consistently, $CD8^+$ T_{RM} cells expressed the highest *Cxcr6* levels among major skin immune populations (Figure S5J), and immunostaining confirmed that recruited $CD8^+$ T cells in CNO-treated skin often localized near CXCL16-high keratinocytes (Figure 5E). Moreover, T_{EFF} and T_{EM} cells, which were preferentially recruited, expressed high CXCR6, whereas T_{CM} cells, which failed to show increased recruitment, lacked CXCR6 (Figure 5F). Lastly, the rise in keratinocyte CXCL16 expression preceded $CD8^+$ T cell accumulation and returned to baseline within 2 weeks after CNO treatment, coinciding with the contraction of the T_{RM} pool (Figure S5K).

To validate whether CXCL16 is required for the T_{RM} increase, we intradermally injected either an anti-CXCL16 blocking antibody or an immunoglobulin G (IgG) isotype control into defined areas of the back skin of Gi-DREADD mice treated with CNO.[23] In IgG-treated sites, CNO-induced sympathetic inhibition increased $CD8^+$ T_{RM} cells, whereas this increase was suppressed at anti-CXCL16-treated sites (Figure 5G). To directly assess the role of epithelial-derived CXCL16, we generated *$K14^{rtTA}$; $TetO^{Cre}$; $Cxcl16^{fl/fl}$* mice, in which *Cxcl16* can be specifically deleted in epidermal keratinocytes. In these mice, sympathetic inhibition failed to increase skin T_{RM} cells (Figure 5H). Similarly, *$Cxcr6^{-/-}$* mice did not exhibit a T_{RM} increase after 6-OHDA sympathetic denervation (Figure 5I). Finally, we performed a competitive homing assay using a mixture of *in vitro* activated wild-type ($tdTomato^+$) and CXCR6-deficient (GFP^+) $CD8^+$ T cells co-transferred into control and Gi-DREADD mice. Upon sympathetic inhibition, $tdTomato^+$ control cells exhibited robust recruitment to the skin, whereas GFP^+ CXCR6-deficient T cells failed to do so (Figures 5J, S5L, and S5M). Together, these experiments show that keratinocyte-derived CXCL16 targets $CXCR6^+$ $CD8^+$ T cells and is the primary driver of enhanced $CD8^+$ T_{RM} cell recruitment when sympathetic signals are inhibited (Figure 5K).

Beyond chemokine-mediated recruitment, we also considered whether sympathetic signaling affects other molecules that govern T_{RM} differentiation and retention.[66–68] Skin $CD8^+$ T_{RM} cells require a constellation of local signals, including

(F) CXCR6 expression on the $CD8^+$ T_{EFF}, T_{EM}, T_{CM}, and T_{naive} cells from the spleens of steady-state mice (n = 3 mice per group, one-way ANOVA).
(G) Skin $CD8^+$ T cells in Gi-DREADD mice after intradermal CXCL16 blocking antibody (BA) and IgG injection (n = 20 skin areas from 3 mice per group, one-way ANOVA).
(H) Skin $CD8^+$ T cells in control, control with 6-OHDA treatment, and *$K14^{rtTA}$; $TetO^{Cre}$; $Cxcl16^{fl/fl}$* (K14-Cxcl16 cKO) mice with 6-OHDA treatment (n = 15–18 skin areas from 3 mice per group, one-way ANOVA).
(I) Skin $CD8^+$ T cells in control, control with 6-OHDA treatment, and *$Cxcr6^{-/-}$* mice with 6-OHDA treatment (n = 12–29 skin areas from 2–4 mice per group, one-way ANOVA).
(J) Flow cytometric quantification of co-transferred wild-type $tdTomato^+$ and *$Cxcr6^{-/-}$* GFP^+ $CD8^+$ T cells in the epidermis and dermis of control and Gi-DREADD mice (n = 4–5 mice per group, two-tailed unpaired t test).
(K) Schematic of the sympathetic-epithelial communication.
(L) Heatmap of skin T_{RM} development genes in epidermal keratinocytes from control and Gi-DREADD mice.
(M) $CD8^+$ T cells and CXCL16 expression in the nasal mucosa of control and Gi-DREADD mice (n = 6–15 mucosa areas from 5 mice per group, two-tailed unpaired t test).
Violin plots show the distribution with individual data points; horizontal lines indicate the median and interquartile range; $^*p < 0.05$, $^{**}p < 0.01$, $^{***}p < 0.001$; n.s., not significant.
See also Figure S5.

TGF-β,[69,70] IL-15, IL-7,[42] antigen exposure, and interactions with integrins and E-cadherin (*Cdh1*, a binding partner for CD103), to establish residency. Keratinocyte transcriptomic profiling revealed that sympathetic inhibition significantly upregulated multiple factors associated with T_{RM} development in skin epithelium, including TGF-β, E-cadherin, intercellular adhesion molecule 1 (ICAM-1),[71] IL-7, and several integrin- and collagen-encoding genes (Figure 5L). Human epidermal keratinocytes treated with β-blocker nadolol exhibited similar transcriptional changes (Figure S5N), suggesting that sympathetic regulation of epithelial T_{RM} factors is conserved across species.

To determine whether sympathetic inhibition similarly affects $CD8^+$ T_{RM} cells at other epithelial barriers, we examined the nasal mucosa and lung airways. Sympathetic innervation was readily observed near both the nasal and airway epithelium (Figures 5M and S5O). Upon sympathetic inhibition, epithelial CXCL16 expression increased, accompanied by a corresponding rise in $CD8^+$ T_{RM} cell numbers (Figures 5M and S5O). These results suggest that the neuro-epithelial-immune axis operates across multiple barrier tissues.

Sympathetic inhibition enhances local cancer immunosurveillance in the skin

$CD8^+$ T_{RM} cells are increasingly recognized as key players in anti-tumor immunity, particularly in the skin.[23,72] We therefore hypothesized that expanding the T_{RM} pool via sympathetic inhibition would strengthen immunosurveillance against nascent cancer cells in the epithelium. To test this, we employed an established epicutaneous melanoma transplantation model.[23] In this model, a low dose of B16 melanoma cells is inoculated into the skin epithelium, which induces a local $CD69^+$ $CD103^+$ $CD8^+$ T_{RM} population targeting melanoma cells. These T_{RM} cells help establish a durable tumor-immune equilibrium in the skin epithelium to restrict cancer progression, which allows a subset of mice to remain free of macroscopic skin lesions long after inoculation (“tumor-free” mice)[23] (Figures 6A and S6A). Sympathetic inhibition markedly improved local tumor control. By 6 weeks post-inoculation, the percentage of tumor-free mice doubled in the sympathetically inhibited group compared with controls (Figure 6B). Skin from these tumor-free mice contained abundant $CD8^+$ T_{RM} cells intermingled with melanoma cells throughout the epithelium, suggestive of ongoing immune surveillance or cytotoxic activity (Figure 6C). Furthermore, higher T_{RM} density correlated with fewer melanoma cells in the epithelium (Figure 6D). Flow cytometry confirmed increased $CD69^+$ $CD103^+$ $CD8^+$ T_{RM} cells in the skin but not T_{EFF} in draining lymph nodes (Figures 6E, S6B, and S6C). In mice that developed macroscopic tumors, the average tumor volume in the sympathetic inhibition group was significantly smaller (Figure 6F), with an improved survival rate rising from approximately 30% to 70% (Figure 6G). Since sympathetic inhibition increases T_{RM} cells in both the epidermis and dermis, beneficial anti-tumor responses were also observed when B16 cells were inoculated into the dermis (Figures S6D and S6E). Together, these results suggest that inhibiting sympathetic signaling in the skin enhances anti-tumor immunity by expanding the $CD8^+$ T_{RM} pool.

We next examined whether the enhanced tumor protection with sympathetic inhibition depends on CXCL16-mediated T_{RM} recruitment. We repeated the epicutaneous melanoma inoculation experiment with the anti-CXCL16 blocking antibody or the IgG isotype control (Figure 6H). In IgG-treated mice, sympathetic inhibition consistently increased the proportion of tumor-free mice, slowed tumor growth, and improved survival. However, blocking CXCL16 abolished these effects, resulting in faster tumor growth and larger tumor volumes (Figures 6H–6J). Therefore, elevated CXCL16 and the resultant local $CD8^+$ T_{RM} augmentation are essential for improved immunosurveillance against skin melanoma upon sympathetic inhibition.

Heightened sympathetic activity attenuates skin $CD8^+$ T_{RM} cell formation

We next examined whether heightened sympathetic signaling decreases the number of $CD8^+$ T_{RM} cells. To activate sympathetic nerves, we used *DBH^{Cre}; R26-LSL-Gq-DREADD* mice. CNO administration increased cFOS staining in sympathetic ganglia, confirming neuronal activation (Figure S7A). Enforced local sympathetic activation led to a significant reduction of skin $CD8^+$ T_{RM} cells (Figure 7A). This effect was transient, as T_{RM} numbers decreased shortly after CNO treatment, remained low for approximately 1 week, and then returned to baseline (Figure S7B). To confirm that this effect was mediated by elevated local NE-ADRB2 signaling, we intradermally injected NE into a small area of back skin, with saline injected contralaterally as a control. NE-injected sites showed a significantly lower density of $CD8^+$ T_{RM} cells (Figure 7B). A similar reduction was observed following intradermal injection of the β-adrenergic agonist isoproterenol (Figure S7C). Flow cytometry confirmed the decrease in skin $CD8^+$ T_{RM} cells upon sympathetic activation (Figures 7C and S7D–S7F). By contrast, intradermal injection of neuropeptide Y, acetylcholine, CGRP, or substance P did not impact $CD8^+$ T_{RM} cell numbers (Figure S7G). These results reinforce that elevated local NE-ADRB2 signaling reduces T_{RM} abundance.

We next examined whether heightened sympathetic activity suppresses epithelial-derived factors that attract and retain T_{RM}. Intradermal NE injection caused a pronounced decrease in keratinocyte CXCL16 expression (Figure 7D). Consistently, CXCL16 and TGF-β3 levels were decreased in cultured keratinocytes with activated ADRB2 signaling (Figures 7E and S7H). This trend extended to human skin, where NE exposure lowered CXCL16 and TGF-β3 expression (Figures 7F, 7G, and S7H). The effects of sympathetic hyperactivation were transient, as both CXCL16 and TGF-β3 levels declined rapidly following sympathetic activation and returned to baseline within 2 weeks after CNO injection (Figure S7I).

To test whether reduced CXCL16 mediates T_{RM} decrease upon sympathetic activation, we depleted CXCL16 either by intradermal injection of a CXCL16 blocking antibody or by doxycycline-induced *Cxcl16* deletion in *$K14^{rtTA}$; $TetO^{Cre}$; $Cxcl16^{fl/fl}$* mice. In both cases, skin $CD8^+$ T_{RM} cells decreased rapidly (Figures 7H and S7J). Conversely, co-injection of recombinant CXCL16 protein with NE rescued the reduction (Figure 7I). Consistently, keratinocyte-specific *Cxcl16* deletion was sufficient to accelerate melanoma progression without manipulating nerves (Figures S7K–S7M).

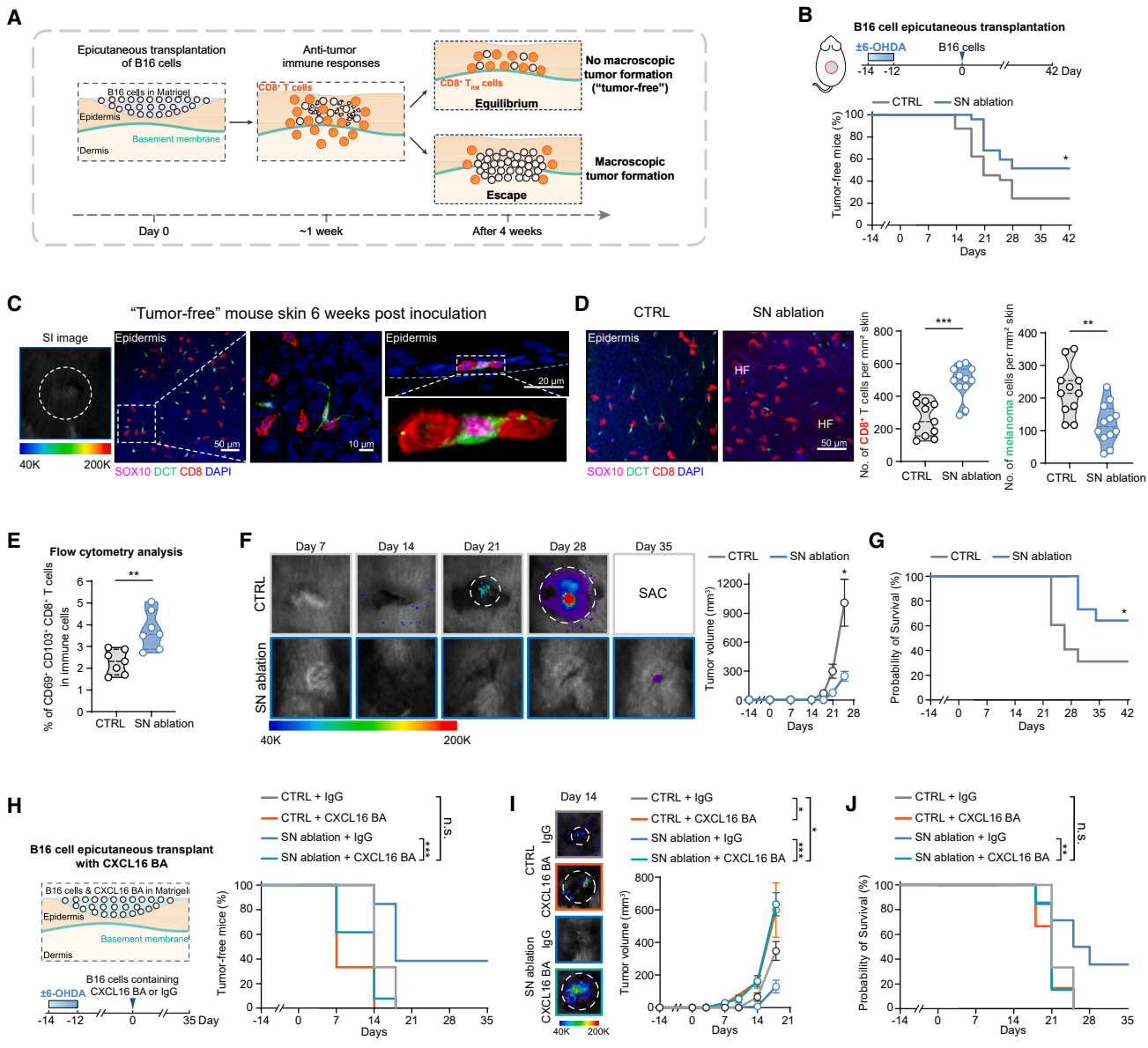

Figure 6. Sympathetic inhibition enhances local cancer immunosurveillance in skin

(A) Schematic of epicutaneous B16 transplantation.

(B) "Tumor-free" mice quantification in control and SN ablation groups after epicutaneous B16 transplantation (n = 24 per group, log-rank Mantel-Cox test).

(C) Bioluminescence and immunofluorescence staining of tumor-free skin for SOX10 and dopachrome tautomerase (DCT; melanoma markers) and CD8.

(D) $CD8^+$ T and B16 cells in tumor-free skin of control and SN ablation mice (n = 11–12 skin areas from 2 mice, two-tailed unpaired t test).

(E) Flow cytometric quantification of $CD8^+$ T_{RM} cells in control and SN ablation mouse skin post B16 epicutaneous inoculation (n = 7 per group, two-tailed unpaired t test).

(F) Tumor growth in control and SN ablation mouse skin (n = 4–7 per group, two-tailed unpaired t test).

(G) Kaplan-Meier survival curves of control and SN ablation mice with B16 epicutaneous inoculation (n = 10 per group, log-rank Mantel-Cox test).

(H–J) Control and SN ablation mice treated with IgG or anti-CXCL16 BA and B16 epicutaneous inoculation, showing tumor-free incidence (H), tumor growth curves (I), and Kaplan-Meier survival curves (J) (n = 6–13 per group, log-rank Mantel-Cox test or two-tailed unpaired t test).

In (F) and (I), mean ± SEM; in (D) and (E), violin plots show distributions with individual points; lines indicate the median and interquartile range; $^*p < 0.05$, $^{**}p < 0.01$, $^{***}p < 0.001$; n.s., not significant.

See also Figure S6.

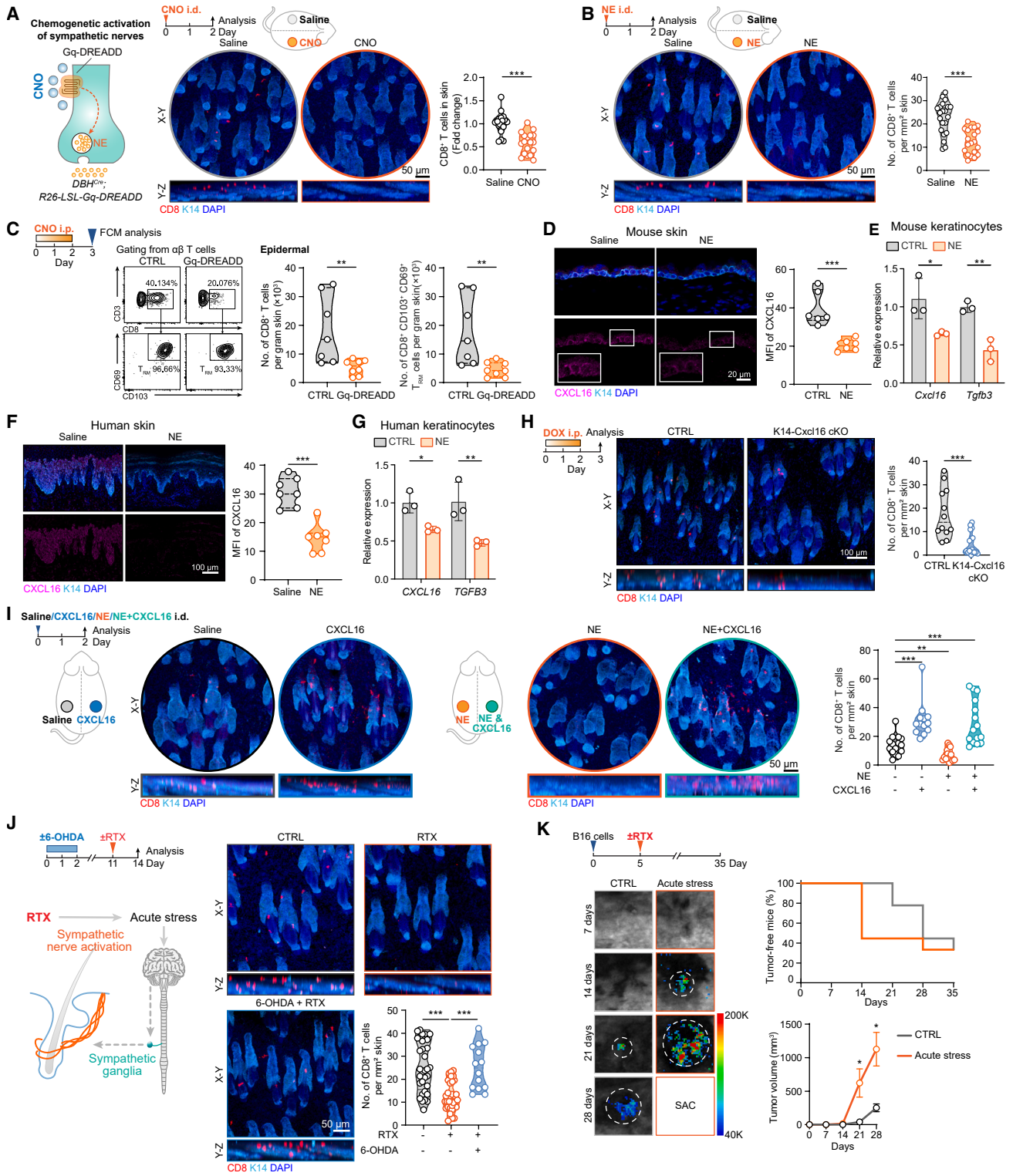

Figure 7. Heightened sympathetic signaling attenuates skin CD8⁺ T_{RM} cell formation

(A) Skin CD8⁺ T cells following intradermal injection of saline or CNO in Gq-DREADD mice (n = 18 skin areas from 3 mice per group, two-tailed unpaired t test).

(B) Skin CD8⁺ T cells after intradermal NE injection (n = 20 skin areas from 4 mice per group, two-tailed unpaired t test).

(C) Representative flow cytometry plots and quantification of epidermal CD8⁺ T and T_{RM} cells in control and Gq-DREADD mice (n = 7–8 mice per group, two-tailed unpaired t test).

(legend continued on next page)

During acute stress, the sympathetic nervous system is highly activated to trigger the fight-or-flight response.[73] In the skin, hyperactivation of cutaneous sympathetic nerves can be achieved using resiniferatoxin (RTX), a capsaicin analog that induces nociception and stimulates the sympathetic nervous system[43] (Figures 7J, left, and S7N). We investigated whether RTX-induced sympathetic hyperactivation dampens the skin CD8$^+$ T_{RM} pool. Following RTX injection, skin CD8$^+$ T_{RM} cells significantly reduced, an effect that was abolished by either sympathetic nerve ablation or sympathetic inhibition using Gi-DREADD (Figures 7J and S7O). Similar effects were observed under chronic stress models (Figure S7P). To assess its impact on immunosurveillance, we performed epicutaneous inoculation of B16 cells followed by RTX injection. Mice injected with RTX exhibited accelerated melanoma progression (Figure 7K). Taken together, these data suggest that acute stress-induced hyperactivation of cutaneous sympathetic nerves dampens the skin T_{RM} pool and compromises the containment of melanoma progression.

DISCUSSION

CD8$^+$ T_{RM} cells act as vigilant sentinels in barrier tissues, providing rapid protection against pathogens and malignancies. While an expanded T_{RM} pool confers stronger local immunity,[11,20,74] its dysregulated growth may trigger autoimmune or inflammatory diseases.[75] Thus, precise control over local CD8$^+$ T_{RM} abundance is critical for tissue homeostasis. Here, we reveal a regulatory axis in which the sympathetic nervous system coordinates with epithelial cells to govern local T_{RM} abundance in the skin. Tonic sympathetic signaling through β2-adrenergic receptors on keratinocytes restricts the recruitment and establishment of new T_{RM} cells, thereby tuning the size of the resident T cell pool. Sympathetic inhibition induces keratinocytes to upregulate CXCL16 and other factors, enhancing T cell homing to the epidermis and differentiation into T_{RM} cells. Conversely, sympathetic hyperactivation during acute stress downregulates epithelial CXCL16, impairing T_{RM} retention and leading to their loss. This neuro-epithelial-immune axis enables the sympathetic nervous system to function as a remote control for tissue-resident immunity, integrating systemic neural cues such as stress to dynamically shape the T_{RM} niche and calibrate local immune set points.

Sympathetic signaling is a key modulator of peripheral immunity.[76–80] For instance, during gut inflammation, heightened sympathetic signals suppress inflammatory responses by directly targeting ILC2s and macrophages via NE-ADRB2 signaling.[81,82] Here, we find that in the skin, tonic sympathetic signals fine-tune CD8$^+$ T_{RM} abundance and immunosurveillance through a distinct neuro-epithelial axis. Cutaneous sympathetic nerves form spatially restricted, synapse-like structures with immobilized epithelial cells, which collaboratively modulate the T_{RM} niche. Unlike transient interactions with migratory immune cells, this stable architecture provides a consistent and efficient conduit for neural control of local immunity, enabling the extensive epithelial network to amplify neural cues across the tissue barrier. As epithelial barriers are constantly exposed to perturbations, such as microbial invasion and neoplastic transformation, this mechanism likely enables the adaptive adjustment of local T_{RM} density to match surveillance demands without provoking chronic inflammation. Furthermore, in addition to modulating CD8$^+$ T_{RM} cells, sympathetic nerves also interact with tissue stem cells (such as hair follicle stem cells) in the skin, where heightened sympathetic tone promotes stem cell activation and tissue regeneration.[83] We speculate that this dual sympathetic regulation of tissue stem cells and resident immune cells may represent a coordinated strategy that balances local tissue regeneration and immune vigilance. During tissue regeneration, sympathetic-mediated temporal suppression of T_{RM} formation may reduce the risk of autoimmunity from self-antigen exposure during tissue remodeling. Together, our findings highlight the coordinated functions of peripheral nerves, epithelial cells, and tissue-resident immune cells in orchestrating effective local immunosurveillance and tissue homeostasis in barrier tissues.

Recent studies have revealed the critical role of CD8$^+$ T_{RM} cells in cancer immunosurveillance.[72] By maintaining a tumor-immune equilibrium within epithelial tissues, they restrain early-stage malignancies without fully eliminating cancerous cells. CD8$^+$ T_{RM} cells achieve this by recognizing tumor-specific antigens and cytotoxic killing, as well as by producing cytokines and chemokines, including IFN-γ and TNF-α, independently of tumor antigen recognition.[16,18,84] Our results show that inhibiting sympathetic signaling enhances this local immunosurveillance by promoting skin CD8$^+$ T_{RM} formation without inducing functional exhaustion.[85] Expansion of this resident pool is crucial for intercepting early tumors, as circulating T cells often struggle to penetrate peripheral tissues in the absence of strong inflammation at this stage.[11,86] Although the dependence on T_{RM} cells may decline as advanced tumors breach the epithelium and

(D) CXCL16 expression in saline- and NE-treated mouse skin (n = 6 skin areas per group, two-tailed unpaired t test).
(E) RT-qPCR of *Cxcl16* and *Tgfb3* expression in cultured mouse keratinocytes treated with saline or NE (n = 3 replicate treated wells per group, two-way ANOVA).
(F) CXCL16 expression in cultured human skin biopsies treated with saline or NE (n = 7 skin areas per group, two-tailed unpaired t test).
(G) RT-qPCR of *CXCL16* and *TGFB3* expression in cultured human keratinocytes treated with saline or NE (n = 3 replicate treated wells per group, two-way ANOVA).
(H) Skin CD8$^+$ T cells in control and K14-Cxcl16 cKO mice (n = 12–18 skin areas from 2–3 mice per group, two-tailed unpaired t test).
(I) CD8$^+$ T cells in skin areas intradermally treated with saline, CXCL16, NE, and NE + CXCL16 (n = 13–17 skin areas from 3 mice per group, two-tailed unpaired t test).
(J) Skin CD8$^+$ T cells in control, RTX, and 6-OHDA + RTX-treated mice (n = 14–35 skin areas from 3–7 mice per group, one-way ANOVA).
(K) Tumor-free incidence (n = 9 per group, log-rank Mantel-Cox test), bioluminescence images, and tumor growth curves (n = 4–5 per group, two-tailed unpaired t test) in mice with B16 epicutaneous inoculation together with RTX.
In (K), mean ± SEM; in other panels, bar graphs show mean ± SD; violin plots show the distribution with individual data points; horizontal lines indicate the median and interquartile range; $^*p < 0.05$, $^{**}p < 0.01$, $^{***}p < 0.001$; n.s., not significant.
See also Figure S7.

remodel their microenvironment, targeting epithelial T_{RM} cells remains a promising strategy for early tumor control. Conversely, stress-induced sympathetic hyperactivation suppresses T_{RM} development, impairing the eradication and confinement of early malignant cells. Given that mutated cells continuously arise from epithelial niches throughout life, this neural inhibition of immunosurveillance may contribute to increased cancer risk during stressful periods in humans.[87] Together, these findings underscore the importance of the neuro-epithelial-immune axis in maintaining lifelong tissue integrity.

Beyond tumor defense, $CD8^+$ T_{RM} cells are pivotal for pathogen protection at barrier tissues and have been implicated in multiple autoimmune disorders.[22,88–90] Our findings therefore suggest two potential therapeutic avenues. First, transient sympathetic inhibition (e.g., ADRB2 blockade) during vaccination could boost the generation of protective, long-lived T_{RM} cells and thereby strengthen local immunity against infections. Conversely, sympathetic activation or CXCL16 blockade reduces skin T_{RM} cells. With precise targeting, this strategy might be harnessed to ameliorate autoimmune diseases such as psoriasis or vitiligo. This hypothesis aligns with clinical observations that T cell recruitment in vitiligo is CXCL16 dependent,[91] and β blocker usage has been associated with worsened vitiligo outcomes.[92] A priority for future research is to define the mechanisms and kinetics underlying T_{RM} loss and to rigorously assess safety and tissue specificity. Such insights will be essential for evaluating strategies such as topical sympathetic agonists or CXCL16 pathway modulators.

Limitations of the study

Despite supporting a primary role for sympathetic nerves, this study does not rule out crosstalk from other cutaneous neural networks (e.g., peptidergic or cholinergic) under different contexts. While sympathetic inhibition increased $CD8^+$ T_{RM} numbers in aged and stressed mice, the broader systemic impact of these conditions on the neuro-immune axis requires further dissection. Future work should also clarify how specific keratinocyte subsets contribute to T_{RM} regulation.

RESOURCE AVAILABILITY

Lead contact

Further information and requests for resources and reagents should be directed to and will be fulfilled by the lead contact, Bing Zhang (zhangbing@westlake.edu.cn).

Materials availability

All unique reagents generated in this study are available from the lead contact.

Data and code availability

No original codes were generated in this study. The scRNA-seq and RNA sequencing data are available on the Gene Expression Omnibus under the accession numbers GEO: GSE279697 and GEO: GSE279510, respectively. Any additional information required to reanalyze the data reported in this paper is available from the lead contact upon request.

ACKNOWLEDGMENTS

We thank D. He, B. Li, Q. Ma, Y.-C. Hsu, and D. Li for discussions on the manuscript and the Laboratory Animal Resources Center, High-Performance Computing Center, Flow Cytometry Core, Genomic Core, and Microscopy Core at Westlake University for technical support. This work was supported in part by grants from the National Natural Science Foundation of China (project 32170850 to B.Z.), the Zhejiang Provincial Natural Science Foundation of China (project QKWL25C1201 to B.Z.), the SMART Investigator Program (40113-13011401225 to B.Z.), the Pioneer and "Leading Goose" R&D Program of the Department of Science and Technology of Zhejiang Province (2023SDXHDX0001 and 2024SSYS0034), the Noncommunicable Chronic Diseases-National Science and Technology Major Program (2023ZD0500402 to T.Z.), the Westlake Laboratory of Life Sciences and Biomedicine, the Research Center for Industries of the Future, and the Center of Synthetic Biology and Integrated Bioengineering at Westlake University.

AUTHOR CONTRIBUTIONS

Conceptualization, B.Z. and T.Z.; methodology, P.Z. and J.M.; investigation, P.Z., J.M., Haoyue Yu, Hualin Yu, C.L., L.Z., and P.Y.; validation, P.Z., J.M., and Haoyue Yu; formal analysis, P.Z. and J.M.; data curation, P.Z. and J.M.; resources, P.Z., J.M., B.Z., and T.Z.; visualization, P.Z. and J.M.; writing, B.Z. and T.Z.; supervision, B.Z. and T.Z.; funding acquisition, B.Z. and T.Z.

DECLARATION OF INTERESTS

A patent application covering the methods for controlling skin $CD8^+$ T_{RM} cell formation has been filed by Westlake University, listing B.Z., T.Z., P.Z., and J.M. as inventors.

STAR★METHODS

Detailed methods are provided in the online version of this paper and include the following:

- KEY RESOURCES TABLE
- EXPERIMENTAL MODEL AND STUDY PARTICIPANT DETAILS
  - Animal studies
- METHOD DETAILS
  - Drug treatments
  - Immunohistochemistry
  - Imaging and imaging analysis
  - Transmission electron microscopy
  - *In vivo* vascular imaging of Gi-DREADD mouse skin
  - Neurotransmitter and neuropeptide measurement
  - Flow cytometry analysis
  - Fluorescence-activated cell sorting (FACS) of skin
  - RNA sequencing library preparation
  - RNA sequencing analysis
  - Single-cell gene expression analysis sample preparation
  - Single-cell data pre-processing and quality control
  - Single-cell data batch effect correction and sample integration
  - Identification of cell types
  - Estimation of chemotaxis pairs in skin
  - T cell transfer
  - EdU tracing experiment
  - Cell lines, cell culture, transfections and culture additives
  - B16 melanoma cell transplantation
  - Blocking antibody treatments
  - Nasal mucosa and lung epithelia analysis
  - Culture of human skin biopsy *in vitro*
  - Chronic stress model
  - Quantitative reverse-transcription PCR
  - Western blot
- QUANTIFICATION AND STATISTICAL ANALYSIS
  - Statistical analysis

Received: February 18, 2025
Revised: November 6, 2025
Accepted: December 20, 2025
Published: January 29, 2026

REFERENCES

1. Veiga-Fernandes, H., and Mucida, D. (2016). Neuro-Immune Interactions at Barrier Surfaces. Cell *165*, 801–811. https://doi.org/10.1016/j.cell.2016.04.041.
2. Chu, C., Artis, D., and Chiu, I.M. (2020). Neuro-immune interactions in the tissues. Immunity *52*, 464–474. https://doi.org/10.1016/j.immuni.2020.02.017.
3. Klein Wolterink, R.G.J.K., Wu, G.S., Chiu, I.M., and Veiga-Fernandes, H. (2022). Neuroimmune Interactions in Peripheral Organs. Annu. Rev. Neurosci. *45*, 339–360. https://doi.org/10.1146/annurev-neuro-111020-105359.
4. Wallrapp, A., and Chiu, I.M. (2024). Neuroimmune Interactions in the Intestine. Annu. Rev. Immunol. *42*, 489–519. https://doi.org/10.1146/annurev-immunol-101921-042929.
5. Peng, J., Chen, H., and Zhang, B. (2022). Nerve–stem cell crosstalk in skin regeneration and diseases. Trends Mol. Med. *28*, 583–595. https://doi.org/10.1016/j.molmed.2022.04.005.
6. Mueller, S.N., and Mackay, L.K. (2016). Tissue-resident memory T cells: local specialists in immune defence. Nat. Rev. Immunol. *16*, 79–89. https://doi.org/10.1038/nri.2015.3.
7. Masopust, D., and Soerens, A.G. (2019). Tissue-Resident T Cells and Other Resident Leukocytes. Annu. Rev. Immunol. *37*, 521–546. https://doi.org/10.1146/annurev-immunol-042617-053214.
8. Szabo, P.A., Miron, M., and Farber, D.L. (2019). Location, location, location: Tissue resident memory T cells in mice and humans. Sci. Immunol. *4*, eaas9673. https://doi.org/10.1126/sciimmunol.aas9673.
9. Heath, W.R., and Carbone, F.R. (2013). The skin-resident and migratory immune system in steady state and memory: innate lymphocytes, dendritic cells and T cells. Nat. Immunol. *14*, 978–985. https://doi.org/10.1038/ni.2680.
10. Jiang, X., Clark, R.A., Liu, L., Wagers, A.J., Fuhlbrigge, R.C., and Kupper, T.S. (2012). Skin infection generates non-migratory memory CD8+ T(RM) cells providing global skin immunity. Nature *483*, 227–231. https://doi.org/10.1038/nature10851.
11. Gebhardt, T., Wakim, L.M., Eidsmo, L., Reading, P.C., Heath, W.R., and Carbone, F.R. (2009). Memory T cells in nonlymphoid tissue that provide enhanced local immunity during infection with herpes simplex virus. Nat. Immunol. *10*, 524–530. https://doi.org/10.1038/ni.1718.
12. Mackay, L.K., Rahimpour, A., Ma, J.Z., Collins, N., Stock, A.T., Hafon, M.-L., Vega-Ramos, J., Lauzurica, P., Mueller, S.N., Stefanovic, T., et al. (2013). The developmental pathway for CD103(+)CD8+ tissue-resident memory T cells of skin. Nat. Immunol. *14*, 1294–1301. https://doi.org/10.1038/ni.2744.
13. Skon, C.N., Lee, J.-Y., Anderson, K.G., Masopust, D., Hogquist, K.A., and Jameson, S.C. (2013). Transcriptional downregulation of S1pr1 is required for the establishment of resident memory CD8+ T cells. Nat. Immunol. *14*, 1285–1293. https://doi.org/10.1038/ni.2745.
14. Cheuk, S., Schlums, H., Gallais Sérézal, I., Martini, E., Chiang, S.C., Marquardt, N., Gibbs, A., Detlofsson, E., Introini, A., Forkel, M., et al. (2017). CD49a Expression Defines Tissue-Resident CD8+ T Cells Poised for Cytotoxic Function in Human Skin. Immunity *46*, 287–300. https://doi.org/10.1016/j.immuni.2017.01.009.
15. Scott, M.C., Steier, Z., Pierson, M.J., Stolley, J.M., O'Flanagan, S.D., Soerens, A.G., Wijeyesinghe, S.P., Beura, L.K., Dileepan, G., Burbach, B.J., et al. (2025). Deep profiling deconstructs features associated with memory CD8+ T cell tissue residence. Immunity *58*, 162–181.e10. https://doi.org/10.1016/j.immuni.2024.11.007.
16. Schenkel, J.M., Fraser, K.A., Vezys, V., and Masopust, D. (2013). Sensing and alarm function of resident memory CD8$^+$ T cells. Nat. Immunol. *14*, 509–513. https://doi.org/10.1038/ni.2568.
17. Enamorado, M., Iborra, S., Priego, E., Cueto, F.J., Quintana, J.A., Martínez-Cano, S., Mejías-Pérez, E., Esteban, M., Melero, I., Hidalgo, A., et al. (2017). Enhanced anti-tumour immunity requires the interplay between resident and circulating memory CD8+ T cells. Nat. Commun. *8*, 16073. https://doi.org/10.1038/ncomms16073.
18. Ariotti, S., Hogenbirk, M.A., Dijkgraaf, F.E., Visser, L.L., Hoekstra, M.E., Song, J.-Y., Jacobs, H., Haanen, J.B., and Schumacher, T.N. (2014). Skin-resident memory CD8$^+$ T cells trigger a state of tissue-wide pathogen alert. Science *346*, 101–105. https://doi.org/10.1126/science.1254803.
19. Slütter, B., Van Braeckel-Budimir, N., Abboud, G., Varga, S.M., Salek-Ardakani, S., and Harty, J.T. (2017). Dynamics of influenza-induced lung-resident memory T cells underlie waning heterosubtypic immunity. Sci. Immunol. *2*, eaag2031. https://doi.org/10.1126/sciimmunol.aag2031.
20. Park, S.L., Zaid, A., Hor, J.L., Christo, S.N., Prier, J.E., Davies, B., Alexandre, Y.O., Gregory, J.L., Russell, T.A., Gebhardt, T., et al. (2018). Local proliferation maintains a stable pool of tissue-resident memory T cells after antiviral recall responses. Nat. Immunol. *19*, 183–191. https://doi.org/10.1038/s41590-017-0027-5.
21. Christo, S.N., Park, S.L., Mueller, S.N., and Mackay, L.K. (2024). The Multifaceted Role of Tissue-Resident Memory T Cells. Annu. Rev. Immunol. *42*, 317–345. https://doi.org/10.1146/annurev-immunol-101320-020220.
22. Malik, B.T., Byrne, K.T., Vella, J.L., Zhang, P., Shabaneh, T.B., Steinberg, S.M., Molodtsov, A.K., Bowers, J.S., Angeles, C.V., Paulos, C.M., et al. (2017). Resident memory T cells in the skin mediate durable immunity to melanoma. Sci. Immunol. *2*, eaam6346. https://doi.org/10.1126/sciimmunol.aam6346.
23. Park, S.L., Buzzai, A., Rautela, J., Hor, J.L., Hochheiser, K., Effern, M., McBain, N., Wagner, T., Edwards, J., McConville, R., et al. (2019). Tissue-resident memory CD8+ T cells promote melanoma–immune equilibrium in skin. Nature *565*, 366–371. https://doi.org/10.1038/s41586-018-0812-9.
24. Edwards, J., Wilmott, J.S., Madore, J., Gide, T.N., Quek, C., Tasker, A., Ferguson, A., Chen, J., Hewavisenti, R., Hersey, P., et al. (2018). CD103+ Tumor-Resident CD8+ T Cells Are Associated with Improved Survival in Immunotherapy-Naïve Melanoma Patients and Expand Significantly During Anti–PD-1 Treatment. Clin. Cancer Res. *24*, 3036–3045. https://doi.org/10.1158/1078-0432.CCR-17-2257.
25. Hewavisenti, R., Ferguson, A., Wang, K., Jones, D., Gebhardt, T., Edwards, J., Zhang, M., Britton, W., Yang, J., Hong, A., et al. (2020). CD103+ tumor-resident CD8+ T cell numbers underlie improved patient survival in oropharyngeal squamous cell carcinoma. J. Immunother. Cancer *8*, e000452. https://doi.org/10.1136/jitc-2019-000452.
26. Kashem, S.W., Riedl, M.S., Yao, C., Honda, C.N., Vulchanova, L., and Kaplan, D.H. (2015). Nociceptive Sensory Fibers Drive Interleukin-23 Production from CD301b+ Dermal Dendritic Cells and Drive Protective Cutaneous Immunity. Immunity *43*, 515–526. https://doi.org/10.1016/j.immuni.2015.08.016.
27. Pinho-Ribeiro, F.A., Baddal, B., Haarsma, R., O'Seaghdha, M., Yang, N.J., Blake, K.J., Portley, M., Verri, W.A., Dale, J.B., Wessels, M.R., et al. (2018). Blocking neuronal signaling to immune cells treats streptococcal invasive infection. Cell *173*, 1083–1097.e22. https://doi.org/10.1016/j.cell.2018.04.006.
28. Tamari, M., Del Bel, K.L., Ver Heul, A.M., Zamidar, L., Orimo, K., Hoshi, M., Trier, A.M., Yano, H., Yang, T.-L., Biggs, C.M., et al. (2024). Sensory neurons promote immune homeostasis in the lung. Cell *187*, 44–61.e17. https://doi.org/10.1016/j.cell.2023.11.027.
29. Zhu, Y., Meerschaert, K.A., Galvan-Pena, S., Bin, N.-R., Yang, D., Basu, H., Kawamoto, R., Shalaby, A., Liberles, S.D., Mathis, D., et al. (2024). A chemogenetic screen reveals that Trpv1-expressing neurons control regulatory T cells in the gut. Science *385*, eadk1679. https://doi.org/10.1126/science.adk1679.
30. Huh, J.R., and Veiga-Fernandes, H. (2020). Neuroimmune circuits in inter-organ communication. Nat. Rev. Immunol. *20*, 217–228. https://doi.org/10.1038/s41577-019-0247-z.

31. Riol-Blanco, L., Ordovas-Montanes, J., Perro, M., Naval, E., Thiriot, A., Alvarez, D., Paust, S., Wood, J.N., and von Andrian, U.H. (2014). Nociceptive sensory neurons drive interleukin-23-mediated psoriasiform skin inflammation. Nature *510*, 157–161. https://doi.org/10.1038/nature13199.

32. Wallrapp, A., Riesenfeld, S.J., Burkett, P.R., Abdulnour, R.-E.E., Nyman, J., Dionne, D., Hofree, M., Cuoco, M.S., Rodman, C., Farouq, D., et al. (2017). The neuropeptide NMU amplifies ILC2-driven allergic lung inflammation. Nature *549*, 351–356. https://doi.org/10.1038/nature24029.

33. Talbot, J., Hahn, P., Kroehling, L., Nguyen, H., Li, D., and Littman, D.R. (2020). Feeding-dependent VIP neuron–ILC3 circuit regulates the intestinal barrier. Nature *579*, 575–580. https://doi.org/10.1038/s41586-020-2039-9.

34. Zhang, S., Edwards, T.N., Chaudhri, V.K., Wu, J., Cohen, J.A., Hirai, T., Rittenhouse, N., Schmitz, E.G., Zhou, P.Y., McNeil, B.D., et al. (2021). Nonpeptidergic neurons suppress mast cells via glutamate to maintain skin homeostasis. Cell *184*, 2151–2166.e16. https://doi.org/10.1016/j.cell.2021.03.002.

35. Wang, Z., Song, K., Kim, B.S., and Manion, J. (2024). Sensory neuroimmune interactions at the barrier. Mucosal Immunol. *17*, 1151–1160. https://doi.org/10.1016/j.mucimm.2024.10.001.

36. Udit, S., Blake, K., and Chiu, I.M. (2022). Somatosensory and autonomic neuronal regulation of the immune response. Nat. Rev. Neurosci. *23*, 157–171. https://doi.org/10.1038/s41583-021-00555-4.

37. Shin, H., and Iwasaki, A. (2012). A vaccine strategy that protects against genital herpes by establishing local memory T cells. Nature *491*, 463–467. https://doi.org/10.1038/nature11522.

38. Nizard, M., Roussel, H., Diniz, M.O., Karaki, S., Tran, T., Voron, T., Dransart, E., Sandoval, F., Riquet, M., Rance, B., et al. (2017). Induction of resident memory T cells enhances the efficacy of cancer vaccine. Nat. Commun. *8*, 15221. https://doi.org/10.1038/ncomms15221.

39. Rotrosen, E., and Kupper, T.S. (2023). Assessing the generation of tissue resident memory T cells by vaccines. Nat. Rev. Immunol. *23*, 655–665. https://doi.org/10.1038/s41577-023-00853-1.

40. Mackay, L.K., Stock, A.T., Ma, J.Z., Jones, C.M., Kent, S.J., Mueller, S.N., Heath, W.R., Carbone, F.R., and Gebhardt, T. (2012). Long-lived epithelial immunity by tissue-resident memory T (TRM) cells in the absence of persisting local antigen presentation. Proc. Natl. Acad. Sci. USA *109*, 7037–7042. https://doi.org/10.1073/pnas.1202288109.

41. Zaid, A., Mackay, L.K., Rahimpour, A., Braun, A., Veldhoen, M., Carbone, F.R., Manton, J.H., Heath, W.R., and Mueller, S.N. (2014). Persistence of skin-resident memory T cells within an epidermal niche. Proc. Natl. Acad. Sci. USA *111*, 5307–5312. https://doi.org/10.1073/pnas.1322292111.

42. Adachi, T., Kobayashi, T., Sugihara, E., Yamada, T., Ikuta, K., Pittaluga, S., Saya, H., Amagai, M., and Nagao, K. (2015). Hair follicle–derived IL-7 and IL-15 mediate skin-resident memory T cell homeostasis and lymphoma. Nat. Med. *21*, 1272–1279. https://doi.org/10.1038/nm.3962.

43. Zhang, B., Ma, S., Rachmin, I., He, M., Baral, P., Choi, S., Gonçalves, W.A., Shwartz, Y., Fast, E.M., Su, Y., et al. (2020). Hyperactivation of sympathetic nerves drives depletion of melanocyte stem cells. Nature *577*, 676–681. https://doi.org/10.1038/s41586-020-1935-3.

44. Roth, B.L. (2016). DREADDs for Neuroscientists. Neuron *89*, 683–694. https://doi.org/10.1016/j.neuron.2016.01.040.

45. Zhu, H., Aryal, D.K., Olsen, R.H.J., Urban, D.J., Swearingen, A., Forbes, S., Roth, B.L., and Hochgeschwender, U. (2016). Cre-dependent DREADD (Designer Receptors Exclusively Activated by Designer Drugs) mice. Genesis *54*, 439–446. https://doi.org/10.1002/dvg.22949.

46. Boddupalli, C.S., Nair, S., Gray, S.M., Nowyhed, H.N., Verma, R., Gibson, J.A., Abraham, C., Narayan, D., Vasquez, J., Hedrick, C.C., et al. (2016). ABC transporters and NR4A1 identify a quiescent subset of tissue-resident memory T cells. J. Clin. Investig. *126*, 3905–3916. https://doi.org/10.1172/JCI85329.

47. Mackay, L.K., and Kallies, A. (2017). Transcriptional Regulation of Tissue-Resident Lymphocytes. Trends Immunol. *38*, 94–103. https://doi.org/10.1016/j.it.2016.11.004.

48. Mackay, L.K., Minnich, M., Kragten, N.A.M., Liao, Y., Nota, B., Seillet, C., Zaid, A., Man, K., Preston, S., Freestone, D., et al. (2016). Hobit and Blimp1 instruct a universal transcriptional program of tissue residency in lymphocytes. Science *352*, 459–463. https://doi.org/10.1126/science.aad2035.

49. Buggert, M., Price, D.A., Mackay, L.K., and Betts, M.R. (2023). Human circulating and tissue-resident memory CD8+ T cells. Nat. Immunol. *24*, 1076–1086. https://doi.org/10.1038/s41590-023-01538-6.

50. Park, S.L., Christo, S.N., Wells, A.C., Gandolfo, L.C., Zaid, A., Alexandre, Y.O., Burn, T.N., Schröder, J., Collins, N., Han, S.-J., et al. (2023). Divergent molecular networks program functionally distinct CD8+ skin-resident memory T cells. Science *382*, 1073–1079. https://doi.org/10.1126/science.adi8885.

51. Karemaker, J.M. (2017). An introduction into autonomic nervous function. Physiol. Meas. *38*, R89–R118. https://doi.org/10.1088/1361-6579/aa6782.

52. Xu, Z., Chen, D., Hu, Y., Jiang, K., Huang, H., Du, Y., Wu, W., Wang, J., Sui, J., Wang, W., et al. (2022). Anatomically distinct fibroblast subsets determine skin autoimmune patterns. Nature *601*, 118–124. https://doi.org/10.1038/s41586-021-04221-8.

53. Ho, A.W., and Kupper, T.S. (2019). T cells and the skin: from protective immunity to inflammatory skin disorders. Nat. Rev. Immunol. *19*, 490–502. https://doi.org/10.1038/s41577-019-0162-3.

54. Herndler-Brandstetter, D., Ishigame, H., Shinnakasu, R., Plajer, V., Stecher, C., Zhao, J., Lietzenmayer, M., Kroehling, L., Takumi, A., Kometani, K., et al. (2018). KLRG1+ Effector CD8+ T Cells Lose KLRG1, Differentiate into All Memory T Cell Lineages, and Convey Enhanced Protective Immunity. Immunity *48*, 716–729.e8. https://doi.org/10.1016/j.immuni.2018.03.015.

55. Gaide, O., Emerson, R.O., Jiang, X., Gulati, N., Nizza, S., Desmarais, C., Robins, H., Krueger, J.G., Clark, R.A., and Kupper, T.S. (2015). Common clonal origin of central and resident memory T cells following skin immunization. Nat. Med. *21*, 647–653. https://doi.org/10.1038/nm.3860.

56. Casey, K.A., Fraser, K.A., Schenkel, J.M., Moran, A., Abt, M.C., Beura, L.K., Lucas, P.J., Artis, D., Wherry, E.J., Hogquist, K., et al. (2012). Antigen-Independent Differentiation and Maintenance of Effector-like Resident Memory T Cells in Tissues. J. Immunol. *188*, 4866–4875. https://doi.org/10.4049/jimmunol.1200402.

57. Zaid, A., Hor, J.L., Christo, S.N., Groom, J.R., Heath, W.R., Mackay, L.K., and Mueller, S.N. (2017). Chemokine Receptor–Dependent Control of Skin Tissue–Resident Memory T Cell Formation. J. Immunol. *199*, 2451–2459. https://doi.org/10.4049/jimmunol.1700571.

58. Wein, A.N., McMaster, S.R., Takamura, S., Dunbar, P.R., Cartwright, E.K., Hayward, S.L., McManus, D.T., Shimaoka, T., Ueha, S., Tsukui, T., et al. (2019). CXCR6 regulates localization of tissue-resident memory CD8 T cells to the airways. J. Exp. Med. *216*, 2748–2762. https://doi.org/10.1084/jem.20181308.

59. Kok, L., Masopust, D., and Schumacher, T.N. (2022). The precursors of CD8+ tissue resident memory T cells: from lymphoid organs to infected tissues. Nat. Rev. Immunol. *22*, 283–293. https://doi.org/10.1038/s41577-021-00590-3.

60. Hombrink, P., Helbig, C., Backer, R.A., Piet, B., Oja, A.E., Stark, R., Brasser, G., Jongejan, A., Jonkers, R.E., Nota, B., et al. (2016). Programs for the persistence, vigilance and control of human CD8+ lung-resident memory T cells. Nat. Immunol. *17*, 1467–1478. https://doi.org/10.1038/ni.3589.

61. Kumar, B.V., Ma, W., Miron, M., Granot, T., Guyer, R.S., Carpenter, D.J., Senda, T., Sun, X., Ho, S.-H., Lerner, H., et al. (2017). Human Tissue-Resident Memory T Cells Are Defined by Core Transcriptional and Functional Signatures in Lymphoid and Mucosal Sites. Cell Rep. *20*, 2921–2934. https://doi.org/10.1016/j.celrep.2017.08.078.

62. Heim, T.A., Ibrahim, O., Lin, Z., Schultz, A.C., Steele, M.M., Mudianto, T., and Lund, A.W. (2025). CXCR6 promotes dermal CD8+ T cell survival and transition to long-term tissue residence. J. Immunol. vkaf219. https://doi.org/10.1093/jimmun/vkaf219.

63. Scholz, F., Schulte, A., Adamski, F., Hundhausen, C., Mittag, J., Schwarz, A., Kruse, M.-L., Proksch, E., and Ludwig, A. (2007). Constitutive Expression and Regulated Release of the Transmembrane Chemokine CXCL16 in Human and Murine Skin. J. Investig. Dermatol. *127*, 1444–1455. https://doi.org/10.1038/sj.jid.5700751.

64. Vella, J.L., Molodtsov, A., Angeles, C.V., Branchini, B.R., Turk, M.J., and Huang, Y.H. (2021). Dendritic cells maintain anti-tumor immunity by positioning CD8 skin-resident memory T cells. Life Sci. Alliance *4*, e202101056. https://doi.org/10.26508/lsa.202101056.

65. Di Pilato, M.D., Kfuri-Rubens, R., Pruessmann, J.N., Ozga, A.J., Messemaker, M., Cadilha, B.L., Sivakumar, R., Cianciaruso, C., Warner, R.D., Marangoni, F., et al. (2021). CXCR6 positions cytotoxic T cells to receive critical survival signals in the tumor microenvironment. Cell *184*, 4512–4530.e22. https://doi.org/10.1016/j.cell.2021.07.015.

66. Hirai, T., Yang, Y., Zenke, Y., Li, H., Chaudhri, V.K., De La Cruz Diaz, J.S., Zhou, P.Y., Nguyen, B.A.-T., Bartholin, L., Workman, C.J., et al. (2021). Competition for active TGFβ cytokine allows for selective retention of antigen-specific tissue- resident Memory T Cells in the epidermal niche. Immunity *54*, 84–98.e5. https://doi.org/10.1016/j.immuni.2020.10.022.

67. Park, S.L., and Mackay, L.K. (2021). Decoding Tissue-Residency: Programming and Potential of Frontline Memory T Cells. Cold Spring Harb. Perspect. Biol. *13*, a037960. https://doi.org/10.1101/cshperspect.a037960.

68. Crowl, J.T., Heeg, M., Ferry, A., Milner, J.J., Omilusik, K.D., Toma, C., He, Z., Chang, J.T., and Goldrath, A.W. (2022). Tissue-resident memory CD8+ T cells possess unique transcriptional, epigenetic and functional adaptations to different tissue environments. Nat. Immunol. *23*, 1121–1131. https://doi.org/10.1038/s41590-022-01229-8.

69. Christo, S.N., Evrard, M., Park, S.L., Gandolfo, L.C., Burn, T.N., Fonseca, R., Newman, D.M., Alexandre, Y.O., Collins, N., Zamudio, N.M., et al. (2021). Discrete tissue microenvironments instruct diversity in resident memory T cell function and plasticity. Nat. Immunol. *22*, 1140–1151. https://doi.org/10.1038/s41590-021-01004-1.

70. Obers, A., Poch, T., Rodrigues, G., Christo, S.N., Gandolfo, L.C., Fonseca, R., Zaid, A., Kuai, J.E.Y., Lai, H., Zareie, P., et al. (2024). Retinoic acid and TGF-β orchestrate organ-specific programs of tissue residency. Immunity *57*, 2615–2633.e10. https://doi.org/10.1016/j.immuni.2024.09.015.

71. Cox, M.A., Barnum, S.R., Bullard, D.C., and Zajac, A.J. (2013). ICAM-1–dependent tuning of memory CD8 T-cell responses following acute infection. Proc. Natl. Acad. Sci. USA *110*, 1416–1421. https://doi.org/10.1073/pnas.1213480110.

72. Park, S.L., Gebhardt, T., and Mackay, L.K. (2019). Tissue-Resident Memory T Cells in Cancer Immunosurveillance. Trends Immunol. *40*, 735–747. https://doi.org/10.1016/j.it.2019.06.002.

73. Ulrich-Lai, Y.M., and Herman, J.P. (2009). Neural regulation of endocrine and autonomic stress responses. Nat. Rev. Neurosci. *10*, 397–409. https://doi.org/10.1038/nrn2647.

74. Schiffer, J.T., Abu-Raddad, L., Mark, K.E., Zhu, J., Selke, S., Koelle, D.M., Wald, A., and Corey, L. (2010). Mucosal host immune response predicts the severity and duration of herpes simplex virus-2 genital tract shedding episodes. Proc. Natl. Acad. Sci. USA *107*, 18973–18978. https://doi.org/10.1073/pnas.1006614107.

75. Hirai, T., Whitley, S.K., and Kaplan, D.H. (2020). Migration and Function of Memory CD8+ T Cells in Skin. J. Investig. Dermatol. *140*, 748–755. https://doi.org/10.1016/j.jid.2019.09.014.

76. Scheiermann, C., Kunisaki, Y., Lucas, D., Chow, A., Jang, J.-E., Zhang, D., Hashimoto, D., Merad, M., and Frenette, P.S. (2012). Adrenergic Nerves Govern Circadian Leukocyte Recruitment to Tissues. Immunity *37*, 290–301. https://doi.org/10.1016/j.immuni.2012.05.021.

77. Suzuki, K., Hayano, Y., Nakai, A., Furuta, F., and Noda, M. (2016). Adrenergic control of the adaptive immune response by diurnal lymphocyte recirculation through lymph nodes. J. Exp. Med. *213*, 2567–2574. https://doi.org/10.1084/jem.20160723.

78. Devi, S., Alexandre, Y.O., Loi, J.K., Gillis, R., Ghazanfari, N., Creed, S.J., Holz, L.E., Shackleford, D., Mackay, L.K., Heath, W.R., et al. (2021). Adrenergic regulation of the vasculature impairs leukocyte interstitial migration and suppresses immune responses. Immunity *54*, 1219–1230.e7. https://doi.org/10.1016/j.immuni.2021.03.025.

79. Wong, C.H.Y., Jenne, C.N., Lee, W.-Y., Léger, C., and Kubes, P. (2011). Functional Innervation of Hepatic iNKT Cells Is Immunosuppressive Following Stroke. Science *334*, 101–105. https://doi.org/10.1126/science.1210301.

80. Schiller, M., Azulay-Debby, H., Boshnak, N., Elyahu, Y., Korin, B., Ben-Shaanan, T.L., Koren, T., Krot, M., Hakim, F., and Rolls, A. (2021). Optogenetic activation of local colonic sympathetic innervations attenuates colitis by limiting immune cell extravasation. Immunity *54*, 1022–1036.e8. https://doi.org/10.1016/j.immuni.2021.04.007.

81. Moriyama, S., Brestoff, J.R., Flamar, A.-L., Moeller, J.B., Klose, C.S.N., Rankin, L.C., Yudanin, N.A., Monticelli, L.A., Putzel, G.G., Rodewald, H.-R., et al. (2018). β2-adrenergic receptor–mediated negative regulation of group 2 innate lymphoid cell responses. Science *359*, 1056–1061. https://doi.org/10.1126/science.aan4829.

82. Gabanyi, I., Muller, P.A., Feighery, L., Oliveira, T.Y., Costa-Pinto, F.A., and Mucida, D. (2016). Neuro-immune interactions drive tissue programming in intestinal macrophages. Cell *164*, 378–391. https://doi.org/10.1016/j.cell.2015.12.023.

83. Shwartz, Y., Gonzalez-Celeiro, M., Chen, C.-L., Pasolli, H.A., Sheu, S.-H., Fan, S.M.-Y., Shamsi, F., Assaad, S., Lin, E.T.-Y., Zhang, B., et al. (2020). Cell Types Promoting Goosebumps Form a Niche to Regulate Hair Follicle Stem Cells. Cell *182*, 578–593.e19. https://doi.org/10.1016/j.cell.2020.06.031.

84. Schenkel, J.M., Fraser, K.A., Beura, L.K., Pauken, K.E., Vezys, V., and Masopust, D. (2014). T cell memory. Resident memory CD8 T cells trigger protective innate and adaptive immune responses. Science *346*, 98–101. https://doi.org/10.1126/science.1254536.

85. Globig, A.-M., Zhao, S., Roginsky, J., Maltez, V.I., Guiza, J., Avina-Ochoa, N., Heeg, M., Araujo Hoffmann, F., Chaudhary, O., Wang, J., et al. (2023). The β1-adrenergic receptor links sympathetic nerves to T cell exhaustion. Nature *622*, 383–392. https://doi.org/10.1038/s41586-023-06568-6.

86. Gebhardt, T., Palendira, U., Tscharke, D.C., and Bedoui, S. (2018). Tissue-resident memory T cells in tissue homeostasis, persistent infection, and cancer surveillance. Immunol. Rev. *283*, 54–76. https://doi.org/10.1111/imr.12650.

87. Moore, J.X., Andrzejak, S.E., Bevel, M.S., Jones, S.R., and Tingen, M.S. (2022). Exploring racial disparities on the association between allostatic load and cancer mortality: A retrospective cohort analysis of NHANES, 1988 through 2019. SSM Popul. Health *19*, 101185. https://doi.org/10.1016/j.ssmph.2022.101185.

88. Boyman, O., Hefti, H.P., Conrad, C., Nickoloff, B.J., Suter, M., and Nestle, F.O. (2004). Spontaneous Development of Psoriasis in a New Animal Model Shows an Essential Role for Resident T Cells and Tumor Necrosis Factor-α. J. Exp. Med. *199*, 731–736. https://doi.org/10.1084/jem.20031482.

89. Cheuk, S., Wikén, M., Blomqvist, L., Nylén, S., Talme, T., Ståhle, M., and Eidsmo, L. (2014). Epidermal Th22 and Tc17 Cells Form a Localized Disease Memory in Clinically Healed Psoriasis. J. Immunol. *192*, 3111–3120. https://doi.org/10.4049/jimmunol.1302313.

90. Povoleri, G.A.M., Durham, L.E., Gray, E.H., Lalnunhlimi, S., Kannambath, S., Pitcher, M.J., Dhami, P., Leeuw, T., Ryan, S.E., Steel, K.J.A., et al. (2023). Psoriatic and rheumatoid arthritis joints differ in the composition of CD8+ tissue-resident memory T cell subsets. Cell Rep. *42*, 112514. https://doi.org/10.1016/j.celrep.2023.112514.

91. Li, S., Zhu, G., Yang, Y., Jian, Z., Guo, S., Dai, W., Shi, Q., Ge, R., Ma, J., Liu, L., et al. (2017). Oxidative stress drives CD8+ T-cell skin trafficking in patients with vitiligo through CXCL16 upregulation by activating the unfolded protein response in keratinocytes. J. Allergy Clin. Immunol. *140*, 177–189.e9. https://doi.org/10.1016/j.jaci.2016.10.013.

92. Schallreuter, K.U. (1995). Beta-adrenergic blocking drugs may exacerbate vitiligo. Br. J. Dermatol. *132*, 168–169. https://doi.org/10.1111/j.1365-2133.1995.tb08660.x.

93. Schindelin, J., Arganda-Carreras, I., Frise, E., Kaynig, V., Longair, M., Pietzsch, T., Preibisch, S., Rueden, C., Saalfeld, S., Schmid, B., et al. (2012). Fiji: an open-source platform for biological-image analysis. Nat. Methods *9*, 676–682. https://doi.org/10.1038/nmeth.2019.

94. Chen, S., Zhou, Y., Chen, Y., and Gu, J. (2018). fastp: an ultra-fast all-in-one FASTQ preprocessor. Bioinformatics *34*, i884–i890. https://doi.org/10.1093/bioinformatics/bty560.

95. Kim, D., Paggi, J.M., Park, C., Bennett, C., and Salzberg, S.L. (2019). Graph-based genome alignment and genotyping with HISAT2 and HISAT-genotype. Nat. Biotechnol. *37*, 907–915. https://doi.org/10.1038/s41587-019-0201-4.

96. Liao, Y., Smyth, G.K., and Shi, W. (2014). featureCounts: an efficient general purpose program for assigning sequence reads to genomic features. Bioinformatics *30*, 923–930. https://doi.org/10.1093/bioinformatics/btt656.

97. Robinson, M.D., McCarthy, D.J., and Smyth, G.K. (2010). edgeR: a Bioconductor package for differential expression analysis of digital gene expression data. Bioinformatics *26*, 139–140. https://doi.org/10.1093/bioinformatics/btp616.

98. Dolgalev, I. (2022). Msigdbr: MSigDB Gene Sets for Multiple Organisms in a Tidy Data Format. R Package Version 2023.1.1. https://cran.r-project.org/web/packages/msigdbr/msigdbr.pdf.

99. Hao, Y., Stuart, T., Kowalski, M.H., Choudhary, S., Hoffman, P., Hartman, A., Srivastava, A., Molla, G., Madad, S., Fernandez-Granda, C., et al. (2024). Dictionary learning for integrative, multimodal and scalable single-cell analysis. Nat. Biotechnol. *42*, 293–304. https://doi.org/10.1038/s41587-023-01767-y.

100. Wolf, F.A., Angerer, P., and Theis, F.J. (2018). SCANPY: large-scale single-cell gene expression data analysis. Genome Biol. *19*, 15. https://doi.org/10.1186/s13059-017-1382-0.

101. Hao, Y., Hao, S., Andersen-Nissen, E., Mauck, W.M., Zheng, S., Butler, A., Lee, M.J., Wilk, A.J., Darby, C., Zager, M., et al. (2021). Integrated analysis of multimodal single-cell data. Cell *184*, 3573–3587.e29. https://doi.org/10.1016/j.cell.2021.04.048.

102. Gur-Cohen, S., Yang, H., Baksh, S.C., Miao, Y., Levorse, J., Kataru, R.P., Liu, X., de la Cruz-Racelis, J., Mehrara, B.J., and Fuchs, E. (2019). Stem cell–driven lymphatic remodeling coordinates tissue regeneration. Science *366*, 1218–1225. https://doi.org/10.1126/science.aay4509.

103. Joost, S., Annusver, K., Jacob, T., Sun, X., Dalessandri, T., Sivan, U., Sequeira, I., Sandberg, R., and Kasper, M. (2020). The Molecular Anatomy of Mouse Skin during Hair Growth and Rest. Cell Stem Cell *26*, 441–457.e7. https://doi.org/10.1016/j.stem.2020.01.012.

104. Cillo, A.R., Cardello, C., Shan, F., Karapetyan, L., Kunning, S., Sander, C., Rush, E., Karunamurthy, A., Massa, R.C., Rohatgi, A., et al. (2024). Blockade of LAG-3 and PD-1 leads to co-expression of cytotoxic and exhaustion gene modules in CD8+ T cells to promote antitumor immunity. Cell *187*, 4373–4388.e15. https://doi.org/10.1016/j.cell.2024.06.036.

105. Supp, D.M., Hahn, J.M., Combs, K.A., McFarland, K.L., and Powell, H.M. (2022). Isolation and feeder-free primary culture of four cell types from a single human skin sample. Star Protoc. *3*, 101172. https://doi.org/10.1016/j.xpro.2022.101172.

106. Liu, W.-Z., Zhang, W.-H., Zheng, Z.-H., Zou, J.-X., Liu, X.-X., Huang, S.-H., You, W.-J., He, Y., Zhang, J.-Y., Wang, X.-D., et al. (2020). Identification of a prefrontal cortex-to-amygdala pathway for chronic stress-induced anxiety. Nat. Commun. *11*, 2221. https://doi.org/10.1038/s41467-020-15920-7.

STAR★METHODS

KEY RESOURCES TABLE

REAGENT or RESOURCE	SOURCE	IDENTIFIER
Antibodies		
Rat monoclonal anti CD8a	eBioscience	Cat# 14-0081-82; RRID: AB_2167274
Chicken polyclonal anti Krt14	Biolegend	Cat# 906004; RRID: AB_2616962
Rabbit polyclonal anti Tyrosine Hydroxylase	Millipore Sigma	Cat# AB152; RRID: AB_390204
Chicken polyclonal anti Tyrosine Hydroxylase	Abcam	Cat# ab76442; RRID: AB_1524535
Goat Polyclonal anti P-Cad	R&D Systems	Cat# AF761; RRID: AB_355581
Goat polyclonal anti CD140a	R&D Systems	Cat# AF1062; RRID: AB_2236897
Rat monoclonal anti-Mouse CD31	BD Biosciences	Cat# 550274; RRID: AB_393571
Rabbit polyclonal anti c-FOS	Abcam	Cat# ab190289; RRID: AB_2737414
FITC Goat polyclonal anti GFP	Abcam	Cat# ab6662; RRID: AB_305635
Rabbit polyclonal anti RFP	ROCKLAND	Cat# 600-401-379; RRID: AB_2209751
Rabbit polyclonal VMAT2	Synaptic Systems	Cat# 138 313; RRID: AB_2619826
Rabbit polyclonal anti CXCL16	HUABIO	Cat# ER1906-85
Guinea Pig anti DCT	HUABIO	Custom-made
Rabbit monoclonal anti β-Actin	Cell Signaling Technology	Cat# 4970; RRID: AB_2223172
APC anti-mouse CD8a (clone S18018E)	BioLegend	Cat# 162306; RRID: AB_2832225
PE/Cyanine7 anti-mouse CD8a (clone S18018E)	BioLegend	Cat# 100722; RRID: AB_312761
PE anti-mouse CD103 (clone W19396D)	BioLegend	Cat# 110904; RRID: AB_2927994
Brilliant Violet 785 anti-mouse CD326 (Ep-CAM, clone G8.8)	BioLegend	Cat# 118245; RRID: AB_2860639
PE anti-mouse CD200 (clone OX-90)	BioLegend	Cat# 123808; RRID: AB_2073942
eFluor 660 anti-mouse CD34 (clone RAM34)	eBioscience	Cat# 50-0341-82; RRID: AB_10596826
Biotin anti-mouse CD45 (clone 30-F11)	BioLegend	Cat# 103104; RRID: AB_312969
Biotin anti-mouse CD140a (clone APA5)	eBioscience	Cat# 13-1401-82; RRID: AB_466607
PerCP-Cy5.5 anti-mouse Sca1 (clone D7)	eBioscience	Cat# 45-5981-82; RRID: AB_914372
Alexa Fluor 700 anti-mouse CD45.2 (clone 104)	BioLegend	Cat# 109822; RRID: AB_493731
FITC anti-mouse CD45.1 Antibody (clone A20)	BioLegend	Cat# 110706; RRID: AB_313495
Alexa Fluor 700 anti-mouse CD45 (clone I3/2.3)	BioLegend	Cat# 147716; RRID: AB_2750449
Brilliant Violet 605 anti-mouse CD3 (clone 17A2)	BioLegend	Cat# 100237; RRID: AB_2562039
Brilliant Violet 785 anti-mouse CD3 (clone 17A2)	BioLegend	Cat# 100231; RRID: AB_11218805
APC/Fire 750 anti-mouse TCR β chain (clone H57-597)	BioLegend	Cat# 109246; RRID: AB_2629697
PE anti-mouse TCR Vα2 (clone B20.1)	BioLegend	Cat# 127808; RRID: AB_1134183
PerCP/Cyanine5.5 anti-mouse TCR Vβ5.1, 5.2 (clone MR9-4)	BioLegend	Cat# 139510; RRID: AB_2566807
Alexa Fluor 488 anti-mouse TCR γ/δ (clone GL3)	BioLegend	Cat# 118128; RRID: AB_2562771
PE anti-mouse CD4 (clone GK1.5)	BioLegend	Cat# 100408; RRID: AB_312693
PE-Cyanine5 anti-mouse FOXP3 Monoclonal Antibody (clone FJK-16s)	eBioscience	Cat# 15-5773-82; RRID: AB_468806
PE/Cyanine5 anti-mouse CD69 (clone H1.2F3)	BioLegend	Cat# 104510; RRID: AB_313113
FITC anti-mouse CD69 (clone H1.2F3)	BioLegend	Cat# 104506; RRID: AB_313109
Pacific Blue anti-mouse CD103 (clone 2E7)	BioLegend	Cat# 121418; RRID: AB_2128619
PE/Dazzle 594 anti-mouse CD186 (CXCR6, clone SA051D1)	BioLegend	Cat# 151117; RRID: AB_2721700
APC anti-mouse CD186 (CXCR6, clone SA051D1)	BioLegend	Cat# 151106; RRID: AB_2572143

(*Continued on next page*)

Continued

REAGENT or RESOURCE	SOURCE	IDENTIFIER
APC/Fire 750 anti-mouse/human CD44 (clone IM7)	BioLegend	Cat# 103062; RRID: AB_2616727
PE anti-mouse CD127 (clone A7R34)	BioLegend	Cat# 135009; RRID: AB_1937252
Brilliant Violet 785 anti-mouse CD62L (clone MEL-14)	BioLegend	Cat# 104440; RRID: AB_2629685
PerCP/Cyanine5.5 anti-mouse/human KLRG1 (clone 2F1/KLRG1)	BioLegend	Cat# 138418; RRID: AB_2563015
Brilliant Violet 605 anti-mouse CD279 (PD-1, clone 29F.1A12)	BioLegend	Cat# 135220; RRID: AB_2562616
Brilliant Violet 421 anti-mouse CD366 (Tim-3, clone RMT3-23)	BioLegend	Cat# 119723; RRID: AB_2616908
PE/Cyanine7 anti-mouse TNF-α (clone MP6-XT22)	BioLegend	Cat# 506324; RRID: AB_2256076
Brilliant Violet 711 anti-mouse IFN-γ (clone XMG1.2)	BioLegend	Cat# 505835; RRID: AB_11219588
PerCP/Cyanine5.5 anti-mouse IL-17A (clone TC11-18H10.1)	BioLegend	Cat# 506920; RRID: AB_961384
Brilliant Violet 711 anti-mouse CD90.2 (clone 30-H12)	BioLegend	Cat# 105349; RRID: AB_2800564
Brilliant Violet 650 anti-mouse/human CD11b (clone M1/70)	BioLegend	Cat# 101239; RRID: AB_11125575
Alexa Fluor® 647 anti-mouse CD11c (clone N418)	BioLegend	Cat# 117312; RRID: AB_389328
PerCP/Cyanine5.5 anti-mouse I-A/I-E (clone M5/114.15.2)	BioLegend	Cat# 107626; RRID: AB_2191071
Fc Receptor Binding Inhibitor Polyclonal Antibody	eBioscience	Cat# 14-9162-42; RRID: AB_2572935
Biotin anti mouse CD11b (clone M1/70)	BioLegend	Cat# 101204; RRID: AB_312787
Biotin anti mouse CD11c (clone N418)	BioLegend	Cat# 117304; RRID: AB_313773
Biotin anti mouse CD19 (clone 104)	BioLegend	Cat# 152420; RRID: AB_2936614
Biotin anti mouse CD4 (clone GK1.5)	BioLegend	Cat# 100404; RRID: AB_312689
Rat Anti-Mouse Cxcl16 Monoclonal antibody (clone 142417)	R&D Systems	Cat# MAB503; RRID: AB_2276752
InVivoPlus rat IgG2a isotype control (clone 2A3)	Bio X Cell	Cat# BE0089; RRID: AB_1107769
Ultra-LEAF™ Purified anti-mouse CD3ε(clone 145-2C11)	BioLegend	Cat# 100340; RRID: AB_11149115
Ultra-LEAF™ Purified anti-mouse CD28	BioLegend	Cat# 102116; RRID: AB_11147170
Chemicals, peptides, and recombinant proteins		
Tamoxifen	Sigma-Aldrich	Cat# T5648
Corn oil	Bide Pharmatech	Cat# BD122284
6-hydroxydopamine hydrobromide	Sigma-Aldrich	Cat# 162957
Ascorbic acid	Sigma	Cat# A92902
Clozapine N-oxide	Sigma-Aldrich	Cat# C0832
Diphtheria Toxin from Corynebacterium diphtheriae	Sigma-Aldrich	Cat# D0564
Resiniferatoxin, RTX	CFW	Cat# 57444-62-9
Doxycycline	MCE	Cat# HY-N0565
Dox food 200ppm	Sysebio	Custom-made
Collagenase II	Gibco	Cat# 17101015
Collagenase IV	Worthington	Cat# LS004189
DNase I	Roche	Cat# 11284932001

(*Continued on next page*)

Continued

REAGENT or RESOURCE	SOURCE	IDENTIFIER
Liberase™ TL	Roche	Cat# 5401020001
BASIC DMEM, High Glucose, Pyruvate	Gibco	Cat# C11995500BT
BASIC RPMI 1640 Medium	Gibco	Cat# C11875500BT
Superior fetal bovine serum	CellMax	Cat# SA211.02
Fetal bovine serum	Sigma-Aldrich	Cat# F8318
0.25% Trypsin-EDTA	Gibco	Cat# 2520056
Insulin	MedChemExpress	Cat# HY-P0035
Antibiotics-antimycotic	MACKLIN	Cat# A6533
A8301	Tocris	Cat# 379762
DMH-1	Tocris	Cat# 813305
Y27632	Tocris	Cat# 1254/10
Matrigel Matrix	Corning	Cat# 356234
EGF Protein, Human, Recombinant (ECD), HPLC-verified	SinoBiologica	Cat# 10605-HNAE
D-Luciferin potassium salt	Beyotime	Cat# ST196
Albumin from chicken egg white	Sigma	Cat# A5503
Complete Freund's adjuvant	InvivoGen	Cat# vac-cfa-10
TRIzol™ LS	Thermo Fisher Scientific	Cat# 10296028
BD GolgiPlug™ Protein Transport Inhibitor	BD Biosciences	Cat# 555029
Nadolol	MCE	Cat# HY-B0804
Yohimbine	MCE	Cat# HY-12715
Norepinephrine bitartrate monohydrate	MCE	Cat# HY-13715B
Isoprenaline hydrochloride	Sigma-Aldrich	Cat# I5627
Neuropeptide Y	Tocris	Cat# 1153/200U
CGRP	Censcript	Cat# RP11095
Substance P	Tocris	Cat# 1156/5
Acetylcholine	MCE	Cat# HY-B0282
CXCL16	SinoBiological	Cat# 50142-M08H
Carboxyfluorescein succinimidyl ester	BioLegend	Cat# 423801
CellTrace™ Violet	Thermo Fisher Scientific	Cat# C34557
DAPI	Sigma	Cat# D9542
DAPI Fluoromount-G®	SouthernBiotech	Cat# 0100-20
Protease inhibitor cocktail	MedChemExpress	Cat# HY-K0010
Benzyl alcohol	Shanghai yuanye Bio-Technology	Cat# S24194
Benzyl benzoate	Shanghai yuanye Bio-Technology	Cat# S24209
4%-20% gradient SDS-PAGE gel	Haoke	Cat# HKW3G42015
Critical commercial assays		
Mouse Biotin Positive Selection Kit II	STEMCELL	Cat# 17665
Zombie Aqua™ Fixable Viability Kit-BV510	Biolegend	Cat# 423101
BD Cytofix/Cytoperm™ Fixation/ Permeabilization Kit	BD Biosciences	Cat# 554714
RNeasy Plus Micro Kit	Qiagen	Cat# 74034
Single Cell Full Length mRNA-Amplification Kit	Vazyme	Cat# N712
TruePrep DNA Library Prep Kit V2 for Illumina	Vazyme	Cat# TD503
PrimeScript™ RT Master Mix kit	Takara	Cat# RR036A
SteadyPure RNA Extraction Kit	Accurate Biology	Cat# AG21024
Click-iT™ EdU Alexa Fluor™ 488 Imaging Kit	Invitrogen	Cat# C10337
Norepinephrine ELISA Kit	Abnova	Cat# KA3836

(*Continued on next page*)

Continued

REAGENT or RESOURCE	SOURCE	IDENTIFIER
Mouse CGRP1 ELISA Kit	Thermo	Cat# EEL090
ACH (Acetylcholine) ELISA Kit	Elabscience	Cat# E-EL-0081
5-HT ELISA Kit	Absin	Cat# abs554104-96T
Deposited data		
RNA-seq data	This paper	GEO: GSE279510
scRNA-seq data	This paper	GEO: GSE279697
Experimental models: Organisms/strains		
Mouse: C57BL/6J	The Jackson Laboratory	JAX: 000664
Mouse: *B6.Cg-Dbh$^{tm3.2(cre)Pjen}$/J*	The Jackson Laboratory	JAX: 033951
Mouse: *B6.129P2-Lyz2$^{tm1(cre)Ifo}$/J*	The Jackson Laboratory	JAX: 004781
Mouse: *B6.129(Cg)-Scn10a$^{tm2(cre)Jwo/TjpJ}$*	The Jackson Laboratory	JAX: 036564
Mouse: *Lhx2$^{tm1.1(cre/ERT2)Zjh}$/J*	The Jackson Laboratory	JAX: 036293
Mouse: *B6N.Cg-Tg(Pdgfra-cre/ERT)467Dbe/J*	The Jackson Laboratory	JAX: 018280
Mouse: *B6.Cg-Tg(Itgax-cre)1-1Reiz/J*	The Jackson Laboratory	JAX: 008068
Mouse: *B6.129(Cg)-Foxp3$^{tm4(YFP/icre)Ayr}$/J*	The Jackson Laboratory	JAX: 016959
Mouse: *FVB-Tg(KRT14-rtTA)F42Efu/J*	The Jackson Laboratory	JAX: 008099
Mouse: *B6.Cg-Tg(tetO-cre)1Jaw/J*	The Jackson Laboratory	JAX: 006234
Mouse: *C57BL/6Smoc-Trpv1$^{em1(Myc-IRES-Cre)Smoc}$*	Shanghai Model Organisms	NM-KI-200139
Mouse: *B6.Cg-Tg(Cd4-cre)1Cwi/BfluJ*	The Jackson Laboratory	JAX: 022071
Mouse: *C57BL/6-Gt(ROSA) 26Sor$^{tm1(HBEGF)Awai}$/J*	The Jackson Laboratory	JAX: 007900
Mouse: *B6.129-Gt(ROSA) 26Sor$^{tm1(CAG-CHRM4*,-mCitrine)Ute}$/J*	The Jackson Laboratory	JAX: 026219
Mouse: *B6N;129-Tg(CAG-CHRM3*,-mCitrine)1Ute/J*	The Jackson Laboratory	JAX: 026220
Mouse: *Gt(ROSA) 26Sor$^{tm4(ACTB-tdTomato,- EGFP)Luo}$/J*	The Jackson Laboratory	JAX: 007576
Mouse: *B6.Cg-Gt(ROSA) 26Sor$^{tm9(CAG-tdTomato)Hze}$/J*	The Jackson Laboratory	JAX: 007909
Mouse: *B6.129S-Gt(ROSA) 26Sor$^{tm34.1(CAG-Syp/tdTomato)Hze}$/J*	The Jackson Laboratory	JAX: 012570
Mouse: *B6.SJL-Ptprc^{a} Pepc^{b}/BoyJ*	The Jackson Laboratory	JAX: 002014
Mouse: B6.129P2-*Cxcr6^{tm1Litt}*/J	The Jackson Laboratory	JAX: 005693
Mouse: C57BL/6JGpt-Cxcl16^{em1Cflox}/Gpt	GemPharmatech	T015127
Mouse: *C57BL/6JGpt-Adrb2^{em1Cflox}/Gpt*	GemPharmatech	T052308
Oligonucleotides		
Primer: Mouse *Cxcl16* Forward: CCTTGTCTCTTGCGTTCTTCC	PrimerBank	12963541a1
Primer: Mouse *Cxcl16* Reverse: TCCAAAGTACCCTGCGGTATC	PrimerBank	12963541a1
Primer: Mouse *Tgfb3* Forward: ATGACCCACGTCCCCTATCA	This paper	N/A
Primer: Mouse *Tgfb3* Reverse: CAGACGGCCAGTTCATTGTG	This paper	N/A
Primer: Human *CXCL16* Forward: GCCATCGGTTCAGTTCA	This paper	N/A
Primer: Human *CXCL16* Reverse: CAATCCCCGAGTAAGCAT	This paper	N/A
Primer: Human *IL-7* Forward: TCCCCTGATCCTTGTTCTGTTG	This paper	N/A

(*Continued on next page*)

Continued

REAGENT or RESOURCE	SOURCE	IDENTIFIER
Primer: Human *IL-7* Reverse: CGATGCTGACCATTAGAACACTC	This paper	N/A
Primer: Human *IL-15* Forward: TTTGGGCTGTTTCAGTGCAG	This paper	N/A
Primer: Human *IL-15* Reverse: ACTTTGCAACTGGGGTGAAC	This paper	N/A
Primer: Human *TGFB1* Forward: CGCGTGCTAATGGTGGAAAC	This paper	N/A
Primer: Human *TGFB1* Reverse: CCGGTAGTGAACCCGTTGAT	This paper	N/A
Primer: Human *TGFB2* Forward: CGAAACTGTCTGCCCAGTTG	This paper	N/A
Primer: Human *TGFB2* Reverse: AAGGAGAGCCATTCGCCTTC	This paper	N/A
Primer: Human *TGFB3* Forward: GGCTGTTGAGAAGAGAGTCCAA	This paper	N/A
Primer: Human *TGFB3* Reverse: GACCTAGCCATTGGGCAGTA	This paper	N/A
Primer: Human *CDH1* Forward: TGGACCGAGAGAGTTTCCCT	This paper	N/A
Primer: Human *CDH1* Reverse: CAAAATCCAAGCCCGTGGTG	This paper	N/A
Software and algorithms		
Fiji (ImageJ)	Schindelin et al.[93]	https://imagej.net/Fiji
FlowJo	FlowJo, LLC	https://www.flowjo.com
ZEN Black/Blue	Zeiss	N/A
Imaris	Bitplane Oxford Instruments	https://imaris.oxinst.com/
GraphPad Prism	GraphPad Software, Inc	https://www.graphpad.com
fastp	Chen et al.[94]	https://github.com/OpenGene/fastp
HISAT2	Kim et al.[95]	https://github.com/DaehwanKimLab/hisat2
featurecounts	Liao et al.[96]	http://subread.sourceforge.net/
edgeR (v3.38.4)	Robinson et al.[97]	https://github.com/jianjinxu/edgeR
Msigdbr (v7.5.1)	Dolgalev[98]	https://CRAN.R-project.org/package=msigdbr
CellRanger (v7.2.0)	10× Genomics	https://www.10xgenomics.com/support/software/cell-ranger/latest
Single-cell variational inference (scVI) (v1.1.5)	Hao et al.[99]	https://satijalab.org/seurat
Scanpy (v1.10.2)	Wolf et al.[100]	https://scanpy.readthedocs.io/en/stable
Anndata (0.10.8)	Wolf et al.[100]	https://anndata.readthedocs.io/en/latest
Seurat (v5.0.0)	Hao et al.[101]	https://satijalab.org/seurat
Python (v3.9.19)	Python™	https://www.python.org
R (v4.2.2)	The R Project for Statistical Computing	http://www.r-project.org

EXPERIMENTAL MODEL AND STUDY PARTICIPANT DETAILS

Animal studies

C57BL/6J, *DBH*^{Cre}, *LysM*^{Cre}, *CD4*^{Cre}, *CD11c*^{Cre}, *Foxp3*^{Cre}, *Lhx2*^{CreER}, *Pdgfra*^{CreER}, *K14*^{rtTA}, *TetO*^{Cre}, *R26-iDTR*, *R26-LSL-Gi-DREADD*, *R26-LSL-Gq-DREADD*, *R26-LSL-tdTomato*, *R26-mTmG*, *R26-Syp/tdTomato*, Cxcr6$^{-/-}$, CD45.1 and OT-1 mouse strains were obtained from the Jackson Laboratory. *Adrb2*^{flox} and *Cxcl16*^{flox} mouse strains were obtained from the GemPharmatech. *Trpv1*^{Cre} mice were generated by Shanghai Model Organisms and provided by D. He (Westlake University). All mice were maintained under specific-pathogen-free conditions at 22°C, 40–70% humidity, with a 12-hour light/dark cycle. All experiments were conducted on both male and female mice of comparable age, with age-matched littermates serving as controls. Mice older than 2 years were

defined as "aged mice." Unless specified, experiments were initiated during the telogen phase of the hair follicle cycle in 6 to 10-week-old mice. The experimental protocols were approved by the Institutional Animal Care and Use Committee of Westlake University (AP#23-077-ZB) and adhered to all relevant ethical regulations.

METHOD DETAILS

Drug treatments

To ablate sympathetic nerves, 6-hydroxydopamine hydrobromide (6-OHDA, Sigma-Aldrich 162957) was freshly prepared by dissolving in 0.1% ascorbic acid in 0.9% sterile NaCl solution (saline) and administered intraperitoneally at a dose of 250 mg/kg body weight around postnatal day (P) 40, followed by daily doses of 100 mg/kg body weight consecutively for two days. Control mice received equivalent amounts of vehicle solution. To ablate sympathetic nerves genetically, diphtheria toxin (0.25 mg/kg body weight) was administered intraperitoneally into *DBH^{Cre}; Rosa^{iDTR}* mice for six consecutive days, starting around P40. To ablate cutaneous sensory nerves, diphtheria toxin (0.25 mg/kg body weight) was administered intraperitoneally to *Trpv1^{Cre}; Rosa^{iDTR}* and *Nav1.8^{Cre}; Rosa^{iDTR}* mice for seven consecutive days, starting around P21. To manipulate sympathetic activities systemically, 250 μg/kg clozapine-N-oxide (CNO, Sigma-Aldrich C0832) was administered intraperitoneally into *DBH^{Cre}; R26-LSL-Gi-DREADD* or *DBH^{Cre}; R26-LSL-Gq-DREADD* mice for 3 consecutive days unless otherwise specified. To manipulate sympathetic activities locally in the skin, a single dose of 100 μL of CNO (5 μg/mL in saline) was administered intradermally into the dorsal skin to avoid systemic effects. This produced a small, localized bleb that resolved within 10 minutes. This approach is well tolerated in mice. Vehicle (saline) of equivalent volume was administered into the contralateral side. For tamoxifen treatment, tamoxifen (Sigma-Aldrich T5648) was prepared in corn oil (Bide Pharmatech BD122284) at 20 mg/ml and injected intraperitoneally at 200mg/kg for 6–8 days. For β-adrenergic receptor blockade, nadolol (MCE HY-B0804) was freshly dissolved in saline containing 0.1% ascorbic acid to achieve a final concentration of 2.5 mM. A single dose of 100 μL was administered intradermally to the right dorsal skin of mice, with an equivalent volume of vehicle (saline with 0.1% ascorbic acid) injected into the contralateral side. For α2-adrenergic receptor blockade, yohimbine (MCE HY-127715) was freshly dissolved in saline containing 0.1% ascorbic acid to achieve a final concentration of 2.5 mM. A single dose of 100 μL was administered intradermally into the right dorsal skin of mice, with an equivalent volume of vehicle injected into the contralateral side. For norepinephrine injection, norepinephrine bitartrate monohydrate (NE, MCE HY-13715B) was freshly dissolved in saline containing 0.1% ascorbic acid to achieve a final concentration of 2 mM. A single dose of 100 μL was administered intradermally into the right dorsal skin of mice, with an equivalent volume of vehicle injected into the contralateral side. For adrenergic agonist injection, isoprenaline hydrochloride (ISO, MCE HY-13715B) was dissolved in saline containing 0.1% ascorbic acid to a final concentration of 10 mg/mL. A single dose of 100 μL was administered intradermally into the right dorsal skin of mice, with an equivalent volume of vehicle injected into the contralateral side. For local administration of cholinergic agonists and neuropeptides, acetylcholine (MCE HY-B0282), neuropeptide Y (R&D 1153), CGRP (Censcript RP11095), and substance P (Tocris 1156/5) were dissolved in saline to final concentrations of 0.4 mg/mL, 10 μg/mL, 5 μg/mL, and 100 nM, respectively. A single dose of 100 μL of each compound solution was administered intradermally into the right dorsal skin of mice, with an equal volume of vehicle injected into the contralateral side. To specifically knock out *Adrb2* and *Cxcl16* in the keratinocytes, mice were fed a doxycycline-containing rodent diet (SYSE C11300-0200) from P35 to P50. For acute knockout of *Cxcl16* in the keratinocytes, doxycycline (MCE HY-N0565) was dissolved in corn oil at 20 mg/mL and administered intraperitoneally at 10 μL per gram of body weight for three consecutive days before euthanasia. For local treatment of CXCL16, 1 μg CXCL16 was dissolved in 100 μL of saline and injected intradermally into the right dorsal skin in a single dose. An equal volume of vehicle was injected into the contralateral side. For co-injection of CXCL16 and NE, 1 μg of CXCL16 was dissolved in 100 μL of 2 mM NE solution (prepared as described above) and injected intradermally into the right dorsal skin in a single dose, while the same volume of NE solution was injected into the contralateral side. For the nociceptive-induced acute stress model, mice received a single subcutaneous injection of resiniferatoxin (RTX, 50 μg/kg, CFW 57444-62-9) into the right dorsal skin, and skin samples were collected three days later.

Immunohistochemistry

Mouse skin samples were fixed in 4% paraformaldehyde (PFA) for 15 minutes at room temperature, washed with PBS, and then immersed in 30% sucrose overnight at 4°C. The samples were subsequently embedded in optimal cutting temperature (OCT) compound (Sakura Finetek 4583). For immunofluorescent staining, slides were fixed in 4% PFA for 2 minutes, washed with PBS and 0.3% Tween-20 in PBS, then blocked for 1–2 hours at room temperature in blocking buffer (5% donkey serum, 1% BSA, and 2% cold-water fish gelatin in 0.3% Triton X-100 in PBS). Primary antibodies were applied overnight at 4°C, and secondary antibodies were applied for 2-4 hours at room temperature. For cFOS staining, sympathetic ganglia were fixed in 4% PFA overnight at 4°C, then washed with PBS and embedded in OCT compound. 10-μm thick sections were fixed in 2% PFA for 5 minutes, washed in 0.3% Triton X-100 in PBS, and incubated with 0.1 M glycine for 5 minutes. Slides were then washed, blocked for 1.5 hours at room temperature, incubated with the primary cFOS antibody overnight at 4°C, and then incubated with the secondary antibody overnight at 4°C. Images were captured using a Zeiss 800 confocal microscope and analyzed with Zen software. Whole-mount staining was conducted as previously described,[102] with some modifications. Briefly, dorsal skin was collected following Nair treatment, fixed in 4% PFA for 1 hour at room temperature, and then extensively washed in PBS overnight at 4°C. The skin was subsequently trimmed to the desired size and permeabilized in 0.3% Triton X-100 in PBS for at least 5 hours, followed by incubation in blocking

buffer for an additional 4 hours. The samples were stained with primary antibodies for 24 hours at room temperature, and washed with 0.3% Triton X-100 in PBS for 5 hours. Samples were then incubated for another 24 hours at room temperature with secondary antibodies conjugated to Alexa Fluor 488, Cy3, or 647 (1:400, Jackson ImmunoResearch), along with DAPI (0.2 μg/mL, Sigma D9542), all under gentle shaking. After washing with PBS containing 0.3% Triton X-100, the samples were refixed in 4% PFA for 1 hour at 4°C. Subsequently, the samples were dehydrated using a sequential series of 25%, 50%, 75%, and 100% methanol, followed by tissue clearing with benzyl alcohol and benzyl benzoate. Images were captured using a Zeiss 800 confocal microscope and analyzed with Zen software. Antibodies used: CD8a (rat, eBioscience 14-0081-82, 1:100), CD8a-APC (rat, BioLegend 162306, 1:200), Krt14 (chicken, BioLegend 906004, 1:300), TH (rabbit, Millipore Sigma AB152, 1:1000), Pcad (goat, R&D Systems AF761, 1:200), CD140a (goat, R&D Systems AF1062, 1:100), CD31 (rat, BD Biosciences 550274, 1:500), CD11c-AF647 (Armenian hamster, BioLegend 117312, 1:200), CD103-PE (rat, BioLegend 110904, 1:100), cFOS (rabbit, Abcam ab190289, 1:1000), GFP (goat, Abcam ab6662, 1:1000), RFP (rabbit, ROCKLAND 600-401-379, 1:1000), VMAT2 (rabbit, Synaptic Systems 138313, 1:500), and CXCL16 (rabbit, HUABIO ER1906-85, 1:500).

Imaging and imaging analysis

Fluorescent images were acquired using a Zeiss LSM 800 confocal microscope equipped with ×10, ×20, or ×63 objective lenses. Unless otherwise stated, images were displayed as maximum intensity projections. For whole-mount staining samples, images were captured at 10× magnification, covering an area of 1.28 mm × 1.28 mm. $CD8^+$ T cell quantification was performed using ImageJ software.

Transmission electron microscopy

To visualize neurotransmitter-positive vesicles in skin, mice were perfused transcardially with a solution containing 4% glutaraldehyde and 2% paraformaldehyde before harvesting dorsal skin. The skin samples were sliced into small pieces (1 mm × 2 mm) and fixed by 2.5% glutaraldehyde and 2.5% paraformaldehyde in 0.1 M sodium cacodylate buffer at 4 °C. After washing in 0.1 M cacodylate buffer, they were post-fixed with 1% osmium tetroxide in 1.5% potassium ferrocyanide for 1 hour, washed twice in water and once in maleate buffer (MB), followed by incubation in MB containing 1% uranyl acetate for 1 hour before two final water washes. The samples were subsequently dehydrated in a graded series of ethanol solutions (10 minutes each at 50%, 70%, 90%, and twice at 100%), then placed in propylene oxide for 1 hour and infiltrated overnight in pure resin. The following day, the samples were embedded in the same resin. Ultra-thin sections (approximately 70 nm) were cut using an ultramicrotome, mounted on copper grids, and stained with 3% uranyl acetate for 30 minutes and Sato's lead solution for 3 minutes. Transmission electron microscope images were recorded with a Thermo Scientific Talos L120C G2 transmission electron microscope.

In vivo vascular imaging of Gi-DREADD mouse skin

The Gi-DREADD mouse was anesthetized with isoflurane. After gentle hair removal, the skin was cleansed with a cotton swab. Evans Blue was administered intravenously via the tail vein 10 minutes before each imaging session. The mouse was then placed laterally on a custom-made stage and secured with medical tape. A drop of sterile saline was applied to the skin surface, covered with a coverslip, and immobilized on the stage, ensuring neither compression of vessels nor excessive looseness. Sterile water was added on the coverslip before imaging under a 25× objective. Blood vessels were identified and their spatial coordinates recorded to enable precise relocalization in subsequent sessions. Imaging was performed at four time points: 10 minutes before intraperitoneal CNO injection, and at 0.5, 24, and 48 hours post-injection. All images were acquired using an IVM-CMS3 microscope system. Vascular diameter and blood flow velocity were quantified with ImageJ software.

Neurotransmitter and neuropeptide measurement

Neurotransmitter and neuropeptide release from skin explants was measured as described previously with minor modifications.[27] Briefly, full-thickness skin punch biopsies (12 mm in diameter) were collected from the flank region. Tissues were immediately transferred to 24-well plates containing 1 mL DMEM and incubated ex vivo at 32°C with gentle shaking (150 rpm) for 45 min. After incubation, culture supernatants were collected for subsequent analysis. For measurement of plasma neurotransmitter and neuropeptide levels, whole blood was drawn from the mouse orbital sinus using heparin sodium as an anticoagulant. Plasma was isolated by centrifugation and stored at –80°C until analysis. Concentrations of NE, CGRP, acetylcholine, and serotonin were quantified using ELISA according to the manufacturers' protocols with the following kits: Norepinephrine ELISA Kit (Abnova KA3836), Mouse CGRP1 ELISA Kit (Thermo EEL090), ACH (Acetylcholine) ELISA Kit (Elabscience E-EL-0081), and 5-HT ELISA Kit (Absin abs554104-96T).

Flow cytometry analysis

Mouse dorsal skin was harvested after shaving, and subcutaneous connective tissues were carefully removed using forceps. For whole-skin digestion, the skin was minced into small fragments and digested in an enzyme solution containing 1 mg/mL Collagenase II (Gibco 17101015), 2 mg/mL Collagenase IV (Worthington LS004189), and 10 μg/mL DNase I (Roche 11284932001) for 80 min at 37 °C on a shaker. The digested tissue was centrifuged, and the pellet was resuspended in 0.25% Trypsin-EDTA (Gibco 25200056) for an additional 10 min at 37 °C. The reaction was stopped by adding FBS, and the resulting cell suspension was filtered through 70-μm and 40-μm cell strainers to obtain single cells.

For separate digestion of the epidermis and dermis, skin sheets were first incubated in 0.25% Trypsin-EDTA with the dermal side facing down for 20 min at 37 °C on a shaker. The trypsin solution was then removed and replaced with 0.25% Liberase™ TL (Roche, 5401020001) for a further 20 min digestion at 37 °C on a shaker. The epidermal layer was gently scraped off and subsequently digested in 0.25% Liberase™ TL solution for an additional 10 min before collection, while the remaining dermal sheets were minced into fragments smaller than 1 mm^2 and digested in 10 mL enzyme cocktail containing 2 mg/mL Collagenase IV, 1 mg/mL Collagenase II, and 10 μg/mL DNase I for 30 min at 37 °C. Both epidermal and dermal digests were passed through 70-μm and 40-μm cell strainers to obtain single-cell suspensions. For samples from male mice, all digestion times were approximately doubled.

For flow cytometry analysis, Zombie Aqua™ Fixable Viability Kit-BV510 (BioLegend 423101) was used to stain the dead cells for 20 minutes at room temperature. Cell suspensions were then incubated with an Fc receptor binding inhibitor polyclonal antibody (eBioscience 14-9162-42) for 20 minutes at 4°C, followed by fluorophore-conjugated antibodies against specific cell surface markers for 30 minutes at 4°C. For TNFα, IFNγ, and IL-17A staining, cell suspensions were first incubated with GolgiPlug (1:1000, BD Biosciences 555029) for 4 hours at 37°C before staining for dead cells and antibodies. Cells were then fixed and permeabilized using the Cytofix/Cytoperm kit (BD Biosciences 554714) and stained for cytokines at 4°C for 60 minutes. Fluorescence spectra were acquired using a Cytek Aurora and analyzed with FlowJo (Version 10).

Fluorophore-conjugated antibodies used: CD45-Alexa Fluor 700 (BioLegend 147716, 1:200), CD45.1-FITC (BioLegend 110706, 1:200), CD8α-PE/Cyanine7 (BioLegend 100722, 1:100), CD8α-APC (BioLegend 162305, 1:100), CD4-PE (BioLegend 100408, 1:200), TCRβ-APC/Fire 750 (BioLegend 109246, 1:200), CD3e-Brilliant Violet 605 (BioLegend 100237, 1:200), CD3e-Brilliant Violet 785 (BioLegend 100231, 1:200), IFNγ-Brilliant Violet 711 (BioLegend 505835, 1:200), TNFα-PE/Cyanine7 (BioLegend 506324, 1:200), IL-17A-PerCP/Cyanine5.5 (BioLegend 506920, 1:200), CD103-Pacific Blue (BioLegend 121418, 1:200), CD69-PE/Cyanine5 (BioLegend 104510, 1:200), CD69-FITC (BioLegend 104506, 1:200), CD11b-Brilliant Violet 650 (BioLegend 101239, 1:200), FOXP3-PE-Cyanine5 (eBioscience 15-5773-82, 1:200), CD11c-Alexa Fluor 647 (BioLegend 117312, 1:200), I-A/I-E-PerCP/Cyanine5.5 (BioLegend 107626, 1:200), CD366-Brilliant Violet 421 (TIM3, BioLegend 119723, 1:200), CD279-Brilliant Violet 605 (PD-1, BioLegend 135220, 1:200), CD90.2-Brilliant Violet 711 (BioLegend 105349, 1:200), CD44-APC/Fire 750 (BioLegend 103062, 1:100), CD62L-BV785 (BioLegend 104440, 1:200), CD127-PE (BioLegend 135009, 1:100), CXCR6-APC (BioLegend 151106, 1:100), and CXCR6-PE/Dazzle 594 (BioLegend 151117, 1:100).

Fluorescence-activated cell sorting (FACS) of skin

Mouse dorsal skin was dissected into small pieces and digested in an enzyme solution containing 1 mg/mL Collagenase II, 2 mg/mL Collagenase IV, and 10 μg/mL DNase I for 80 min at 37 °C on a shaker. After digestion, the suspension was centrifuged at 500g at 4°C for 10 minutes. The pellet was further digested with 0.25% Trypsin-EDTA at 37°C for 15 minutes. The resulting suspension was sequentially filtered through 70-μm and 40-μm filters and centrifuged at 500g and 4°C for 10 minutes. Cells were resuspended in 5% FBS-DPBS and stained with fluorescent dye-conjugated antibodies at 4°C for 30 minutes. Cell sorting was performed using a BD FACSAria Fusion sorter. Antibodies used included: EpCAM-BV785 (BioLegend 118245, 1:400), CD200-PE (BioLegend 123808, 1:400), CD34-EF660 (eBioscience 50-0341-82, 1:100), CD45-Biotin (eBioscience 13-0451-82, 1:400), CD140a-Biotin (eBioscience 13-1401-82, 1:200), Sca1-PerCP-Cy5.5 (eBioscience 45-5981-82, 1:1000), Streptavidin-FITC (eBioscience 11-4317-87, 1:400), and CD8-APC (BioLegend 162306, 1:200).

RNA sequencing library preparation

Epidermal keratinocytes ($CD140a^-$, $CD45^-$, $CD200^-$, $EpCAM^+$, $Sca1^+$) were isolated from Gi-DREADD and littermate control mice via FACS. Total RNA was extracted from the sorted cells using Trizol followed by purification with the RNeasy Plus Micro Kit (Qiagen 74034). RNA-seq libraries were prepared using the Single Cell Full Length mRNA Amplification Kit (Vazyme N712) and the TruePrep DNA Library Prep Kit V2 for Illumina (Vazyme TD503). Paired-end sequencing reads were generated using the Illumina NovaSeq 6000 platform.

RNA sequencing analysis

Sequencing reads from the RNA-seq libraries were trimmed using fastp; paired reads containing more than 10% N bases, over 50% low-quality bases ($Q \leq 5$), or adapter sequences were excluded. The trimmed reads were aligned to the mouse reference transcriptome (mm10) using HISAT2, and quantification was performed using featureCounts. Transcripts per million (TPM) values were calculated from the gene read counts. Principal component analysis (PCA) was conducted using R software. Gene expression levels were normalized, and differential expression analysis was performed using the EdgeR package in R. Differentially expressed genes between the Gi-DREADD and control samples were identified based on the following criteria: log2 fold change > 1, false discovery rate (FDR) < 0.05, and a total TPM sum across all groups > 10.

Single-cell gene expression analysis sample preparation

Biological replicates from n = 4 pooled mice (Gi-DREADD and control groups) were processed. Dorsal and abdominal skin was digested using the established FACS protocol. At the single-cell suspension stage, equal numbers of cells from each replicate were pooled. The following cell populations were sorted and purified: $CD8^+$ T cells ($CD45^+$, $CD3^+$, $TCR\beta^+$, $CD8^+$), γδ T cells, dermal resident T cells ($CD45^+$, $CD3^+$, $TCR\beta^-$), non-T immune cells ($CD45^+$, $CD3^-$), and non-immune cells ($CD45^-$). Purified cells from each

population were mixed, and 10,000 cells from the pooled sorted sample were loaded onto the 10x Genomics Chromium System for single-cell RNA sequencing.

Library preparation was conducted using the 10x Genomics Chromium Next GEM Single Cell 5' Kit v2 reagents according to the manufacturer's instructions by Novogene. Libraries passing quality control were processed in the Chromium Controller to generate single-cell gel bead-in-emulsions (GEMs) for barcoding. Pooled libraries were sequenced on an Illumina NovaSeq X Plus platform.

Single-cell data pre-processing and quality control

Cell Ranger v7.2 was utilized to demultiplex the FASTQ reads, align them to the GRCm39 mouse transcriptome, and extract the corresponding cell and unique molecular identifier (UMI) barcodes. The output of this pipeline produced a digital gene expression (DGE) matrix for each sample, which records the number of UMIs associated with each gene for each cell barcode. For each cell, we quantified the number of genes and UMIs, retaining high-quality cells that met the criteria of more than 100 genes and fewer than 25,000 UMIs. Cells exhibiting an unusually high detection rate of mitochondrial gene expression (pct_counts_mt > 10) were excluded. Following the initial dimensional reduction, we first removed red blood cells (Hbb-expressing cells). We then filtered out potential doublets by excluding clusters with abnormally high numbers of genes and UMIs that were not in a cycling state, as well as those specifically co-expressing more than two types of cellular marker genes. Clusters with very low numbers of genes or UMIs were also discarded, as they were likely associated with empty partitions or dead cells.

Single-cell data batch effect correction and sample integration

Single-cell variation inference (scVI, v1.1.5) from the scvi-tools was utilized to normalize data across individual samples and to perform dimensionality reduction. The scRNA-seq data were processed using Scanpy (v1.10.2) and Anndata (v0.10.8). Initially, the top 2,000 highly variable genes were identified, followed by the removal of *Tcr, Ig, Hsp* (heat shock protein family), histocompatibility, histone, ribosomal, and mitochondrial genes. A variational autoencoder from scVI was employed to reduce dimensionality to a 30-dimensional latent space, utilizing 128 nodes per hidden layer and two layers with a dropout rate of 10%, considering individual samples as a potential confounding variable. This resulting 30-dimensional latent space was subsequently used for the generation of UMAPs and clustering using the igraph algorithm. Both scvi-tools and Scanpy were implemented in Python (v3.10).

Identification of cell types

To identify cell types, we mapped cell clusters to canonical marker genes, as previously described.[103,104] Each cluster was defined by the specific expression of the following genes: epidermal cells: Epidermal cells (*Krt14, Ly6a, Cd200, Sfn, Mgst1*); HFSCs (*Cd34, Lhx2, Grem1*); fibroblasts (*Twist2, Col1a1, Dcn, Col1a2, Col3a1*); Schwann cells (*S100a1, Plp1, Sox10, Gap43*); mast cells (*Ms4a2, Cpa3, Mcpt4, Fcer1a*); macrophages (*Lyz2, Mrc1, Pf4, C1qb*); Langerhans cells (*Itgax, Cd74, Cd207, Epcam*); canonical dendritic cells (*Flt3, Clec9a*, *Irf8*); type 2 innate immune cells (*Il7r, Kit, Icos, Il5*); and T cell clusters (*Cd3d, Cd3e, Thy1*, along with *Cd8a* and *Cd8b1* for $CD8^+$ T cells; *Cd4* for helper T cells; *Foxp3* and *Ctla4* for regulatory T cells; *Trgv6* for γδ T cells; and *Trgv5* for dermal resident T cells). To further refine the identity of the $CD8^+$ T cell cluster, we trained scVI to generate a latent representation of a published skin $CD8^+$ T cell dataset.[50] After integration, the $CD8^+$ T cells in this study predominantly co-localized with $CD8^+$ T_{RM} cells, thereby clarifying their identities.

Estimation of chemotaxis pairs in skin

We utilized CellChat (v1.5) to infer cell-cell communication by analyzing ligand-receptor pairs and downstream signaling mediators derived from our scRNA-seq data. Normalized counts were loaded, and standard parameters were applied to evaluate secreted signaling between different cell types.

T cell transfer

For adoptive transfer of naïve OT-I cells, splenocyte suspensions were administered intravenously at a dose of 1×10^7 cells per mouse. One day after transfer, 1 μg of endotoxin-free ovalbumin (OVA, Sigma A5503) emulsified in an equal volume of complete Freund's adjuvant (CFA, InvivoGen vac-cfa-10) was inoculated onto gently abraded dorsal skin. In the sympathetic nerve ablation model, 6-OHDA was administered 2 weeks prior to OT-I cell transfer. Full-thickness skin from the inoculation site was collected for immune profiling analysis more than 30 days after OVA challenge. In the Gi-DREADD model, mice received consecutive intraperitoneal injections of CNO from day 5 to 7 post-OVA inoculation. Skin tissue was harvested 50 days after inoculation for subsequent immune profiling.

For antigen-activated $CD8^+$ T cell transfer, naïve female OT-I mice (7–8 weeks old) were immunized intradermally with 1 μg of OVA protein emulsified in an equal volume of CFA. One week later, inguinal lymph nodes were collected and mechanically dissociated through a 70-μm nylon cell strainer to prepare single-cell suspensions. $CD8^+$ T cells were isolated by negative selection using a magnetic sorting kit (STEMCELL 17665) with the following biotinylated antibodies: anti-CD11b (BioLegend 101204), anti-CD11c (BioLegend 117304), anti-CD19 (BioLegend 152420), and anti-CD4 (BioLegend 100404). The purified OT-T cells were labeled with carboxyfluorescein succinimidyl ester (CFSE, BioLegend 423801). A total of 1×10^6 isolated $CD8^+$ T cells were intravenously injected

into age-matched *DBH^{Cre}; R26-LSL-Gi-DREADD* and control mice. Recipient mice received two intraperitoneal injections of CNO prior to T cell transfer, followed by a third injection on day 2. All mice were euthanized on day 3 for flow cytometric analysis and whole-mount immunofluorescence staining.

For memory CD8$^+$ T cell transfer, naïve female OT-I mice (7-8 weeks old) were immunized intradermally with 1 μg OVA emulsified in CFA. One month later, spleens and inguinal lymph nodes were harvested from immunized mice. Single-cell suspensions were prepared from these tissues, and CD8$^+$ T cells were initially enriched using a mouse CD8$^+$ T Cell Isolation Kit (Stemcell Technologies 19853). Subsequently, CD8$^+$ central memory T cells (T_{CM}, CD44$^+$CD127$^+$CD62L$^+$) and CD8$^+$ effector memory T cells (T_{EM}, CD44$^+$CD127$^+$CD62L$^-$) were isolated by FACS on a BD FACSAria Fusion sorter. The following antibody panel was used for sorting: anti-CD8-APC (BioLegend 162306), anti-CD44-APC/Fire™ 750 (BioLegend 103062), anti-CD62L-BV785 (BioLegend 104440), and anti-CD127-PE (BioLegend 135009), with DAPI (Sigma D9542) for live/dead discrimination. Purified CD8$^+$ T_{CM} and T_{EM} populations were differentially labeled with CellTrace™ Violet (CTV, Thermo Fisher Scientific C34557) and CFSE, respectively. After washing, equal numbers of CTV-labeled T_{CM} and CFSE-labeled T_{EM} cells were combined at a 1:1 ratio, and a total of 2×10^6 cells were adoptively transferred into each recipient mouse via intravenous injection.

For *in vitro* activated CD8$^+$ T cell transfer, splenocytes from *Cxcr6$^{-/-}$* and *R26-mTmG* mice were processed into single-cell suspensions. CD8$^+$ T cells were isolated by negative selection using a mouse CD8$^+$ T Cell Isolation Kit (Stemcell Technologies 19853). Purified T cells were activated for 48 h on 6-well plates pre-coated with anti-CD3 (5 μg/mL, BioLegend 100340) and anti-CD28 (5 μg/mL, BioLegend 102116) antibodies, followed by a 48h expansion in medium supplemented with recombinant human IL-2 (10 ng/mL, Peprotech 200-02). Live, activated lymphocytes were enriched by density gradient centrifugation (Dakewe Biotech DKW33-R0100). Subsequently, *Cxcr6$^{-/-}$* CD8$^+$ T cells were labeled with CFSE, and *R26-mTmG* CD8$^+$ T cells were labeled with CTV. Labeled cells were washed three times with PBS, mixed at a 1:1 ratio, and a total of 4×10^6 cells were intravenously injected into Gi-DREADD mice and their littermate controls.

EdU tracing experiment

5-Ethynyl-2′-deoxyuridine (EdU, 25 mg/kg) was intraperitoneally administered every 6 hours for a total of 8 doses over 48 hours, starting from the first CNO treatment in *DBH^{Cre}; R26-LSL-Gi-DREADD* mice. Skin samples were collected 6 hours after the final EdU injection. Whole-mount staining was performed to co-stain EdU and CD8 following the manufacturer's protocol (Invitrogen C10337). The percentage of EdU-positive cells among CD8$^+$ T cells was quantified.

Cell lines, cell culture, transfections and culture additives

B16F10 cells expressing an acetyltransferase/luciferase fusion protein (B16-Luc) were employed in this study. To generate B16-Luc cells, we transduced B16F10 cells using a lentiviral system that expresses the fusion protein. Following transduction, single clones were selected, and substrate assays were conducted to identify and isolate the B16-Luc cells for further experimentation. These cells were cultured in RPMI-1640 medium (Thermo Fisher C11875500BT) supplemented with 10% fetal bovine serum (CellMax SA211.02) and 1× penicillin-streptomycin (Macklin Q6532). All cultures were maintained at 37°C in a 5% CO_2 atmosphere and kept at low passage (2–5 passages) before inoculation into mice.

For isolation of mouse keratinocytes, dorsal and abdominal skin was harvested from newborn C57BL/6J mouse pups. The skin was disinfected with 70% ethanol, and excess fat and blood vessels were removed. After rinsing in DPBS to flatten the tissue, the skin was placed in a 6-well plate containing 4 ml of 0.25% Trypsin-EDTA, with the epidermis facing up and incubated overnight at 4°C. The following day, the epidermis was separated and further digested with 0.25% Trypsin-EDTA. The cell suspension was filtered through a 40 μm filter to remove debris, centrifuged at 1000 rpm for 5 minutes, and resuspended in E medium supplemented with 1 μM A8301 (Tocris 379762), 1 μM DMH-1 (Tocris 813305), 10 μM Y27632 (Tocris 1254/10), and antibiotics for cell expansion at 37°C in a 5% CO_2 atmosphere.

Human keratinocytes were isolated as previously described.[105] Fresh skin samples from healthy donors were collected during surgeries, cleaned with 70% ethanol, and trimmed of excess fat and connective tissue. The skin was cut into small pieces and incubated in 0.25% Trypsin-EDTA at 37°C for 30 minutes to separate the epidermis. The epidermis was gently scraped from the dermis, collected, and further digested in fresh trypsin for 10–15 minutes to achieve a single-cell suspension. The suspension was filtered through a 40 μm mesh, centrifuged, and resuspended in E medium supplemented with 1 μM A8301, 1 μM DMH-1, 10 μM Y27632, recombinant human EGF, and antibiotics. Cells were cultured at 37°C in a humidified 5% CO_2 atmosphere. The study was approved by the Westlake University Ethics Committee (Approval number: 20240722ZB001).

For drug treatment experiments, 1-2 $\times 10^4$ keratinocytes were seeded into 12-well plates and allowed to grow until they reached 60% confluency. Nadolol treatments were performed at a concentration of 3 mM for 12 hours. For NE and ISO treatments, keratinocytes were exposed to 0.5 mM and 2 mM, respectively, for 12 hours. All treatments were conducted in supplemented medium under standard culture conditions.

B16 melanoma cell transplantation

The B16 cell epicutaneous transplant model was adapted from a previous study.[23] Briefly, mice were anesthetized with isoflurane, shaved, and a 1 × 1 cm^2 area on the mid-back skin was lightly abraded using a power tool with a grindstone attachment for 10–15 seconds. The abraded area was wiped with a PBS-soaked cotton-tipped applicator, followed by application of 2×10^5 B16-Luc cells

suspended in 10 μL PBS mixed with 10 μL Matrigel matrix (Corning 356234). For the RTX-treated B16 cell epicutaneous transplant model, both the control and RTX groups were inoculated with a reduced dose of 1.5×10^5 B16-Luc cells. Mice were then placed on a 37 °C warming pad for 10 minutes to allow Matrigel solidification. The wound was covered with a bandage and secured with surgical tape, which was removed after 4 days. To monitor early tumor development, *in vivo* bioluminescence imaging was performed. Mice were intraperitoneally injected with 150 mg/kg D-luciferin potassium salt (Beyotime ST196) in saline, rested for 10 minutes, anesthetized with isoflurane, and shaved before imaging. Images were acquired using a small animal imaging system (Spectral Instruments Imaging, AMI) with a 90-second exposure time. Tumor dimensions were measured with a digital caliper once visible, and tumor volume was calculated using the formula: volume = $(\text{width}^2 \times \text{length})/2$. For the intradermal transplantation of B16-Luc cells, 2×10^5 B16-Luc cells were suspended in a mixture of 100 μL PBS and Matrigel matrix and administered intradermally into the middle area of the skin using a 29G needle. The dimensions of the tumors were measured with a digital caliper using the formula: volume = $((\text{width}^2 \times \text{length})/2)$. Measurements were recorded twice weekly.

Blocking antibody treatments

CXCL16 blocking antibody (R&D Systems MAB503) was freshly prepared by dissolving in saline to a final concentration of 200 μg/mL. For intradermal administration, a single 100 μL dose of CXCL16 blocking antibody was injected into the right dorsal skin of mice, while the contralateral side received an equal volume of rat IgG2a (200 μg/mL, Bio X Cell BE0089) as a control. Mice were then intraperitoneally injected with CNO for three consecutive days.

In the B16 cell epicutaneous transplant model, each mouse was inoculated with a mixture containing 10 μg CXCL16 antibody in 10 μL saline, 2×10^5 B16-Luc cells in 10 μL PBS, and 20 μL Matrigel. The mixture was thoroughly mixed before being applied to the abraded mouse skin. Control mice received an equivalent volume and dose of rat IgG2a.

Nasal mucosa and lung epithelia analysis

Both Gi-DREADD mice and their littermate controls received intraperitoneal injections of CNO as mentioned before, prior to sacrifice. Mice were perfused transcardially with PBS before collecting all organs. The lungs were dissected and fixed in 4% PFA at RT for 4 hours. The upper respiratory tract was perfused intranasally with 4% PFA, fixed for 15 minutes at RT, and then washed once with 0.1 M glycine. The nasal cavities were subsequently decalcified in 250 mM EDTA (pH7.4) at RT for at least 4 days, followed by dehydration in 30% sucrose and embedding in OCT compound, as described previously. Cryosection and IHC were performed using the same procedures as for the skin sample.

Culture of human skin biopsy *in vitro*

Fresh human skin samples from healthy donors were collected during surgeries. The samples were thoroughly washed with PBS containing antibiotics at least five times, each wash lasting 15 minutes. The cleaned skin was then evenly divided into two portions, ensuring that both samples were of similar size and surface area. The two samples were cultured in DMEM with one medium supplemented with 2 mM norepinephrine. After 12 hours of culture, the samples were fixed in 4% PFA for 1 hour for subsequent cryosection and immunofluorescence staining. This study was approved by the Westlake University Ethics Committee (Approval number: 20240722ZB001).

Chronic stress model

To induce chronic stress, mice were confined daily in well-ventilated 50 mL conical polypropylene tubes for 2 hours per day over one consecutive month.[106] The dimensions of the tubes were similar to the size of the animal, allowing only minimal movement. 6-OHDA was administered two weeks prior to the restraint stress treatment.

Quantitative reverse-transcription PCR

Quantitative reverse transcription PCR (RT-qPCR) was performed using the PrimeScript™ RT Master Mix (Takara, RR036A) on Bio-Rad CFX Connect and Jena qTOWER384G real-time PCR systems. For human and mouse samples, cycle threshold (Ct) values were normalized to the endogenous controls *GAPDH* and *Gapdh*, respectively.

Western blot

Two weeks post sympathetic ablation, epidermal keratinocytes were purified by FACS and lysed in RIPA buffer (25 mM Tris, pH 7.4, 150 mM NaCl, 0.5% sodium deoxycholate, 0.1% SDS, 1% Triton X-100) supplemented with a protease inhibitor cocktail (MCE HY-K0010). Protein extracts were separated using a 4%-12% gradient SDS-PAGE gel (Haoke HKW3G42015) and transferred to a nitrocellulose membrane. The membrane was blocked with 5% non-fat milk and probed with primary antibodies, followed by an Alexa Fluor 647-conjugated secondary antibody. Antibodies used: β-Actin (rabbit, Cell Signaling Technology #4970, 1:1000), CXCL16 (rabbit, HUABIO ER1906-85, 1:500), and Donkey Anti-Rabbit-647 (Jackson ImmunoResearch 711-605-152, 1:100).

QUANTIFICATION AND STATISTICAL ANALYSIS

Statistical analysis

All statistical analyses were performed using GraphPad Prism and R software. For comparisons between two groups, unpaired two-tailed Student's t-tests were used. For comparisons involving more than two groups or conditions, One-way ANOVA and Two-way ANOVA were utilized. Tumor-free mice curves and overall survival curves were analyzed using log-rank (Mantel-Cox) tests. Statistical significance was defined as $p < 0.05$, with significance levels indicated as follows: $^{***}p < 0.001$, $^{**}p < 0.01$, $^{*}p < 0.05$. Detailed information on statistical tests can be found in the figure legends. Data are presented as the mean ± standard deviation (s.d.), unless otherwise noted.

Supplemental figures

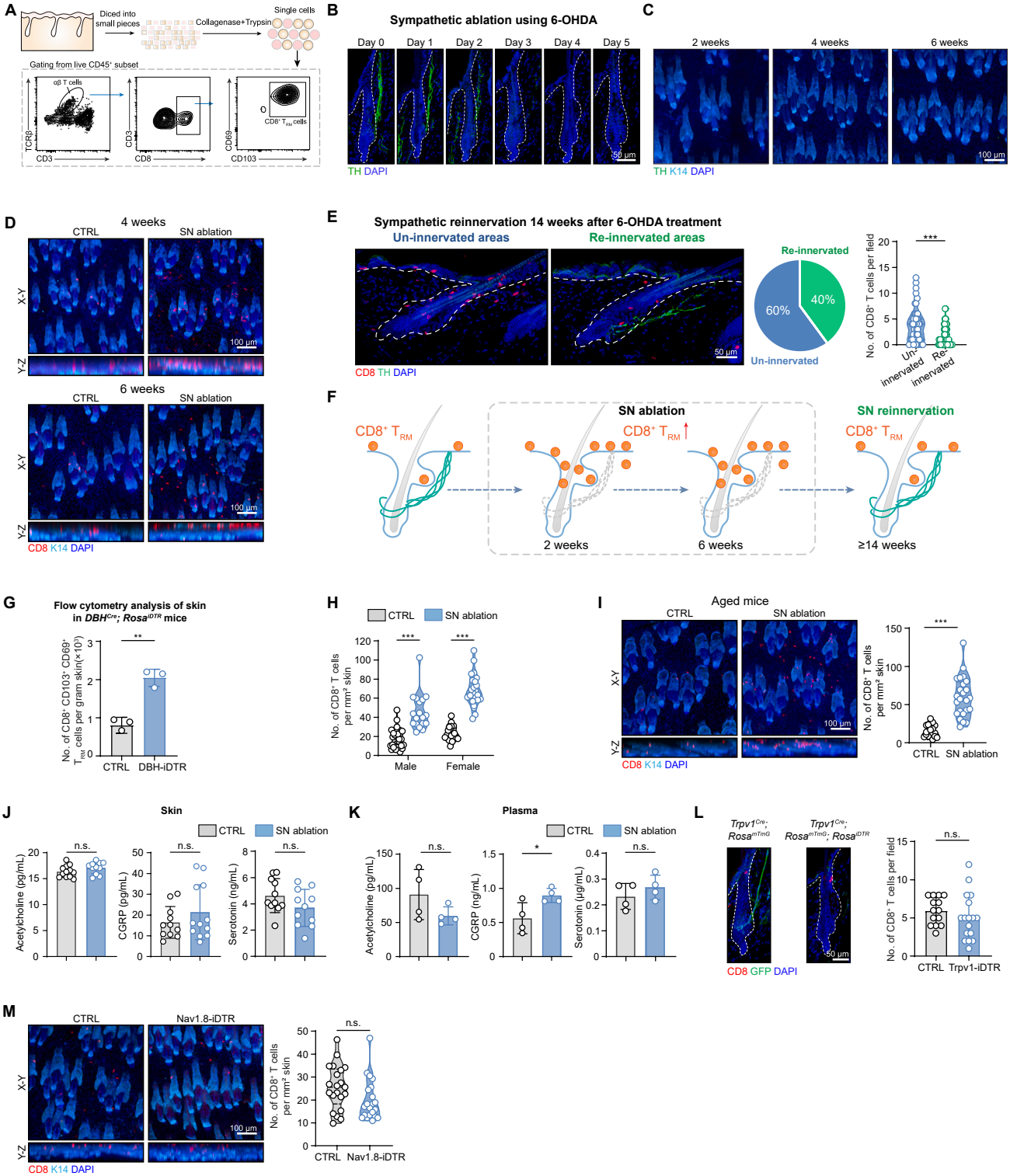

(legend on next page)

Figure S1. Ablation of SNs increases CD8$^+$ T_{RM} cells in skin, related to Figure 1

(A) Flow cytometry workflow and gating strategy for skin immune profiling.

(B) Skin sympathetic nerve ablation using 6-OHDA.

(C and D) Whole-mount staining of skin SNs and CD8$^+$ T cells post 6-OHDA treatment.

(E) Sympathetic re-innervation and CD8$^+$ T cell quantification 14 weeks post 6-OHDA (n = 47 skin areas from 3 mice per group, two-tailed unpaired t test).

(F) Schematic of skin sympathetic innervation and CD8$^+$ T cell dynamics following 6-OHDA treatment.

(G) Flow cytometric quantification of skin CD8$^+$ T_{RM} cells in control and *DBH^{Cre}; R26-iDTR* (DBH-iDTR) mice (n = 3 mice per group, two-tailed unpaired t test).

(H) Skin CD8$^+$ T cell quantification in male and female mice (n = 18–27 skin areas from 3–4 mice per group, two-way ANOVA).

(I) Skin CD8$^+$ T cells in aged mice (>2 years old, n = 18–24 skin areas from 3–4 mice per group, two-tailed unpaired t test).

(J and K) ELISA measurement of acetylcholine, calcitonin gene-related peptide (CGRP), and serotonin (skin: n = 11–12 samples from 3 mice per group; plasma: n = 4 mice per group, two-tailed unpaired t test).

(L and M) Skin sensory nerve ablation and CD8$^+$ T cell quantification (n = 14–21 skin areas from 2–4 mice per group, two-tailed unpaired t test).

Bar graphs show mean ± SD; violin plots show distributions with individual points; lines indicate the median and interquartile range; $^*p < 0.05$, $^{**}p < 0.01$, $^{***}p < 0.001$; n.s., not significant.

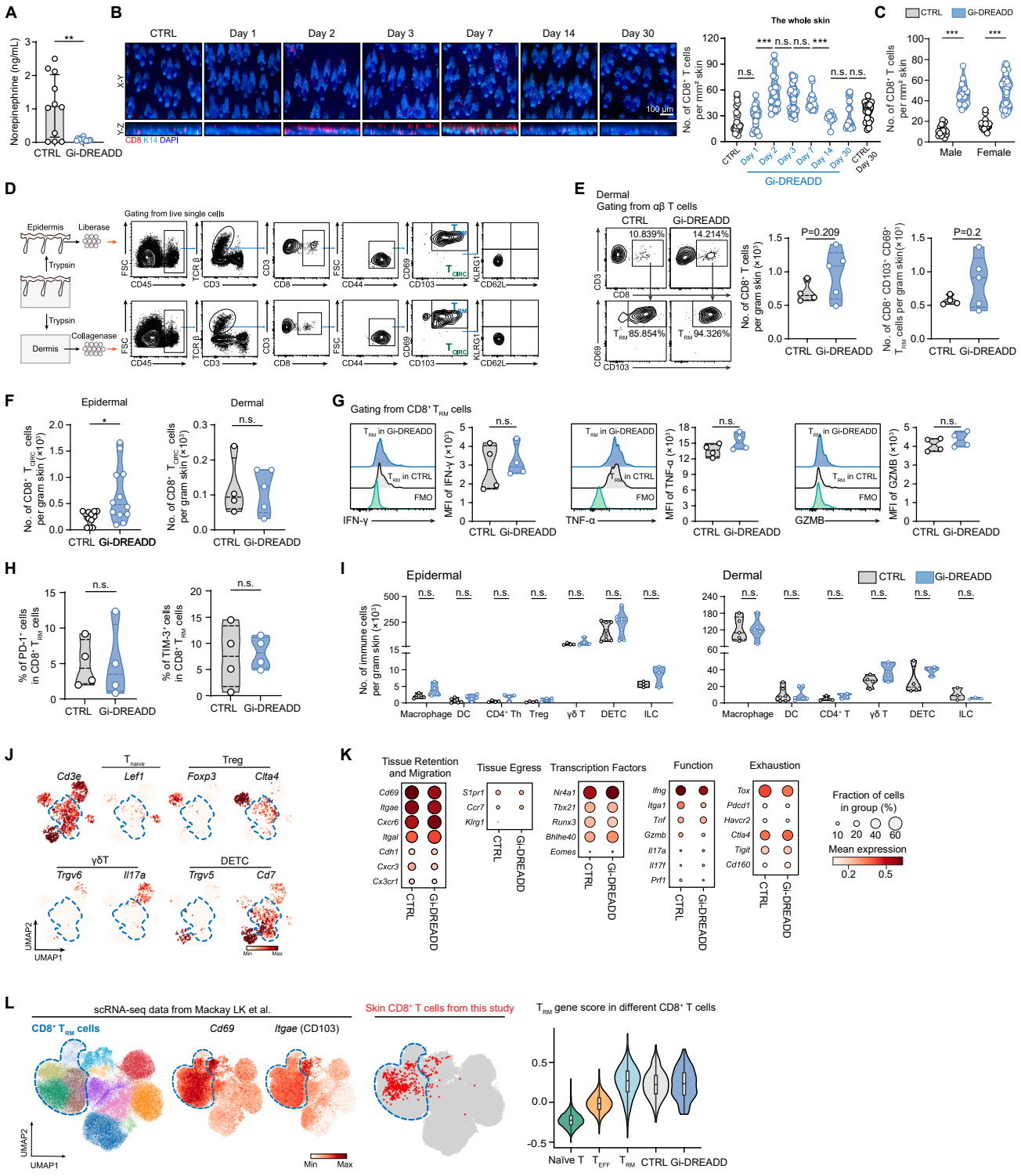

Figure S2. Inhibition of cutaneous sympathetic signals expands the skin CD8$^+$ T_{RM} cell pool, related to Figure 2

(A) ELISA measurement of skin NE levels release from skin (n = 11–12 samples from 3 mice per group, two-tailed unpaired t test).

(B) Skin CD8$^+$ T cells after CNO administration (n = 10–34 skin areas from 2–7 mice per group, two-tailed unpaired t test).

(C) CD8$^+$ T cells in male and female Gi-DREADD mice (n = 12–34 skin areas from 2–7 mice per group, two-tailed unpaired t test).

(D) Flow cytometry workflow and gating strategy for epidermal and dermal immune profiling.

(E) Representative flow cytometry plots and quantification of dermal CD8$^+$ T and T_{RM} cells (n = 4–5 mice per group, two-tailed unpaired t test).

(legend continued on next page)

(F) Flow cytometric quantification of epidermal (n = 11–12 mice per group, two-tailed unpaired t test) and dermal (n = 4–5 mice per group, two-tailed unpaired t test) circulating CD8$^+$ T cells (T_{CIRC}).
(G and H) Flow cytometric quantification of IFN-γ, TNF-α, and granzyme B (GZMB) expression, and PD-1$^+$ and TIM-3$^+$ CD8$^+$ T cells (n = 4 mice per group, two-tailed unpaired t test).
(I) Quantification of skin immune cells (n = 3–8 mice per group, two-tailed unpaired t test).
(J) UMAP visualization of T cell subsets.
(K) Dot plot visualization of skin CD8$^+$ T_{RM} cell marker gene expression.
(L) Mapping and gene score calculation of skin CD8$^+$ T cells to scRNA-seq data from Mackay et al.
Bar graphs show mean ± SD; violin plots show the distribution with individual data points; horizontal lines indicate the median and interquartile range; $^*p < 0.05$, $^{***}p < 0.001$; n.s., not significant.

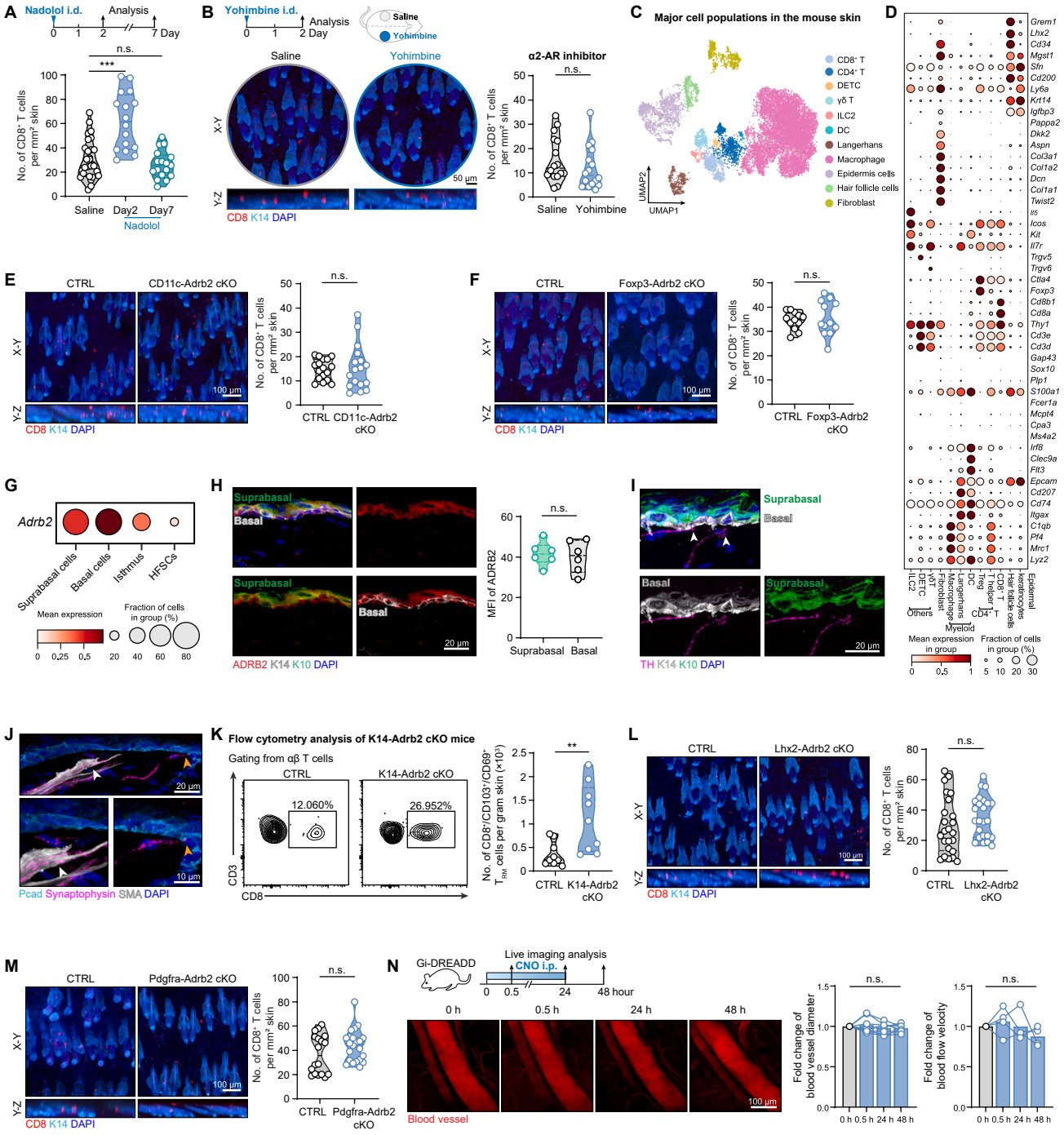

Figure S3. Sympathetic-epithelial communication governs local CD8⁺ T_{RM} cell abundance, related to Figure 3

(A) Skin CD8⁺ T cell quantification after nadolol treatment (n = 16–31 skin areas from 3–6 mice per group, one-way ANOVA).

(B) Skin CD8⁺ T cells after yohimbine treatment (n = 16 skin areas from 3 mice per group, two-tailed unpaired t test).

(C) UMAP visualization of major skin cell populations.

(D) Dot plot of marker gene expression.

(E and F) Skin CD8⁺ T cells in control, *CD11c*^{Cre}*; Adrb2*$^{fl/fl}$ (CD11c-Adrb2 cKO), and *Foxp3*^{Cre}*; Adrb2*$^{fl/fl}$ (Foxp3-Adrb2 cKO) mice (n = 12–17 skin areas from 2–3 mice per group, two-tailed unpaired t test).

(G) *Adrb2* expression in skin epithelial cell subsets from scRNA-seq analysis.

(H) MFI quantification of ADRB2 expression in skin epidermis (n = 6 skin areas, two-tailed unpaired t test).

(I) Immunofluorescence staining of SN, suprabasal, and basal layers of the epidermis. White arrowheads indicate SN innervation with basal keratinocytes.

(legend continued on next page)

(J) Sympathetic innervation of epidermal keratinocytes (yellow arrowheads) and arrector pili muscle (white arrowheads).
(K) Representative flow cytometry plots and quantification of skin $CD8^+$ T_{RM} cells in control and K14-Adrb2 cKO mice (n = 9 mice per group, two-tailed unpaired t test).
(L and M) $CD8^+$ T cells in control, *Lhx2*^{CreER}*; Adrb2*$^{fl/fl}$ (Lhx2-Adrb2 cKO), and *Pdgfra*^{CreER}*; Adrb2*$^{fl/fl}$ (Pdgfra-Adrb2 cKO) mice (n = 18–24 skin areas from 3–4 mice per group, two-tailed unpaired t test).
(N) Live imaging and quantification of blood vessels and blood flow velocity in Gi-DREADD mice (n = 4–8 blood vessels per group, two-tailed unpaired t test).
Violin plots show distributions with individual points; lines indicate the median and interquartile range; $^{**}p < 0.01$, $^{***}p < 0.001$; n.s., not significant.

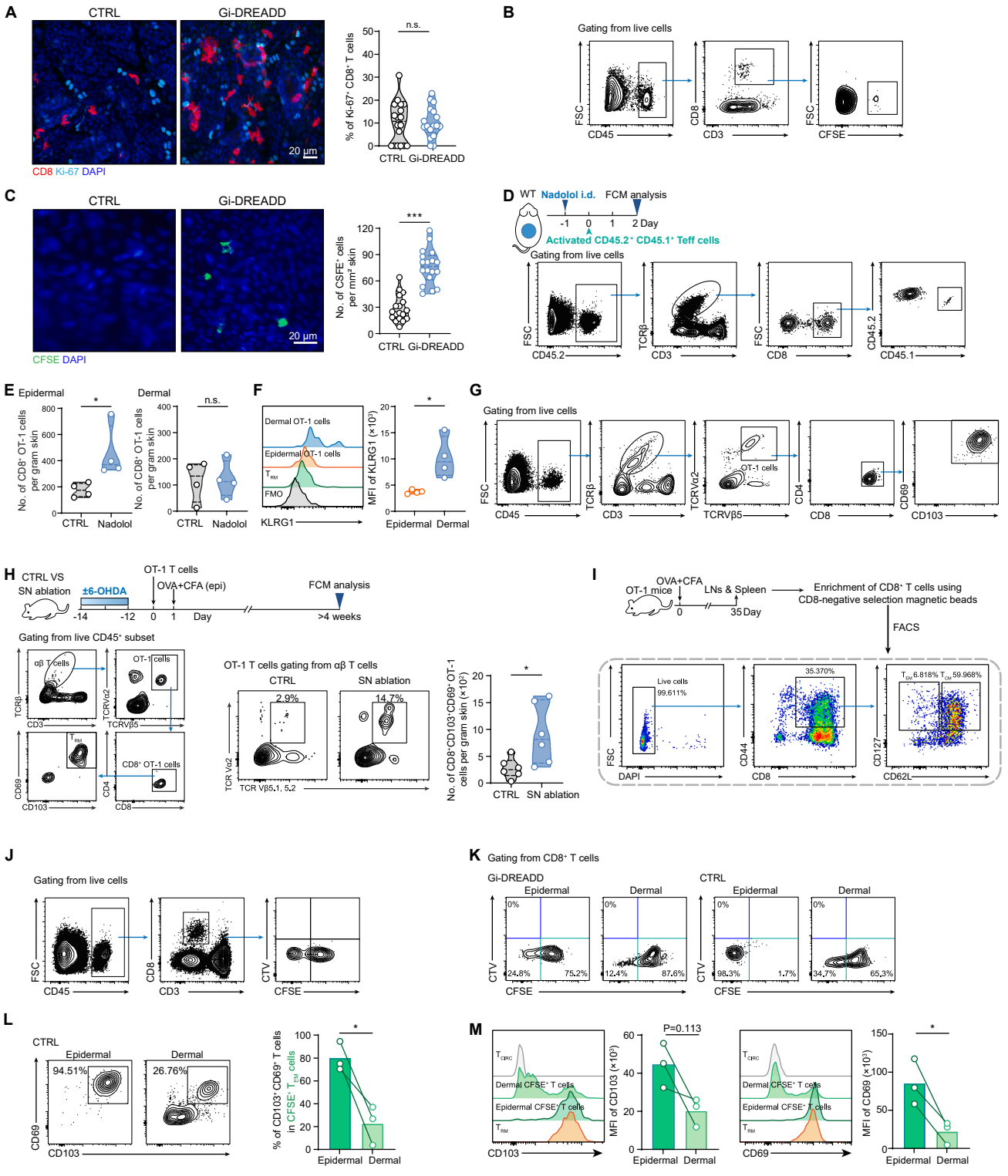

Figure S4. Sympathetic inhibition enhances the recruitment of circulating T cells to the skin, related to Figure 4

(A) Ki-67 staining with skin CD8$^+$ T cells and quantification of Ki-67$^+$ CD8$^+$ T cells (n = 17 skin areas from 3 mice per group).

(B) Gating strategy of skin CFSE$^+$ CD8$^+$ T cells.

(C) CFSE$^+$ cells in the epidermis (n = 18 skin areas from 3 mice per group, two-tailed unpaired t test).

(legend continued on next page)

(D–F) Flow cytometric quantification and KLRG1 expression of CD45.1$^+$ OT-1 cells after activated CD45.1$^+$ OT-1 cell transfer and nadolol treatment (n = 4 mice per group, two-tailed unpaired t test).
(G) Gating strategy of skin OT-1 T_{RM} cells.
(H) Left: gating strategy for skin OT-1 cells. Right: representative flow cytometry plots and quantification of skin OT-1 T_{RM} cells in control and SN ablation mice (n = 6 mice per group, two-tailed unpaired t test).
(I) FACS strategy to purify CD8$^+$ T_{EM} and T_{CM} cells from pooled lymph nodes and spleens of OT-I mice.
(J) Gating strategy for CFSE$^+$ CD8$^+$ T_{EM} and CTV$^+$ T_{CM} cells in the skin.
(K) Representative flow cytometry plots of CD8$^+$ T_{EM} and T_{CM} cells in the epidermal and dermal layers.
(L) Representative flow cytometry plots and quantification of CD103$^+$ CD69$^+$ CFSE$^+$ CD8$^+$ T cells in the epidermis and dermis of control mice (n = 3 mice per group, two-tailed unpaired t test).
(M) Representative flow cytometry histograms and MFI quantification of CD103 and CD69 expression on epidermal and dermal CFSE$^+$ CD8$^+$ T cells of control mice (n = 3 mice per group, two-tailed unpaired t test).
Violin plots show distributions with individual points; lines indicate the median and interquartile range; $^*p < 0.05$, $^{***}p < 0.001$; n.s., not significant.

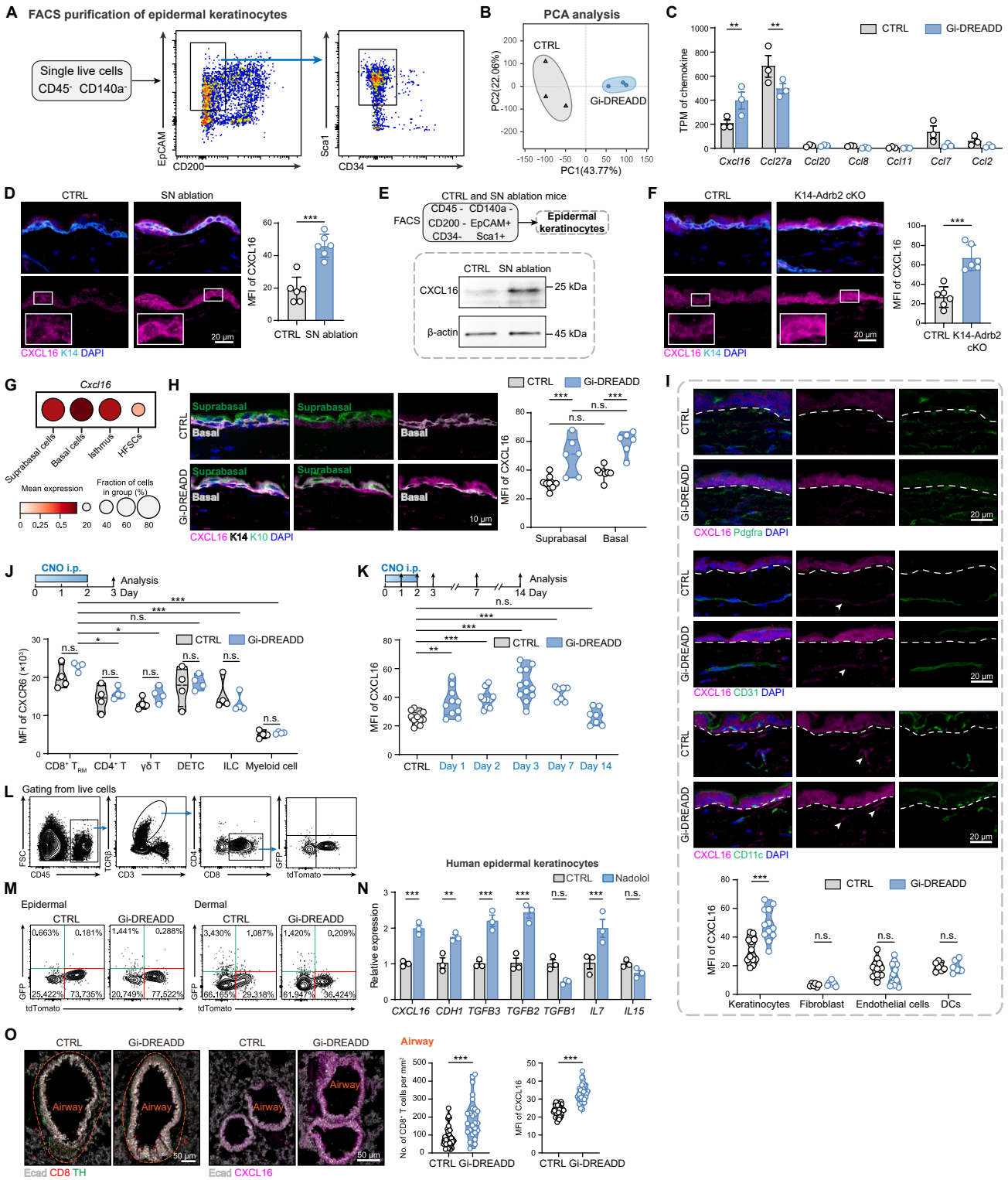

Figure S5. Epithelial-derived signals govern CD8⁺ T_{RM} cell formation, related to Figure 5

(A) FACS strategy for purifying epidermal keratinocytes.

(B) Principal-component analysis (PCA) of gene expression variation.

(C) Transcripts per million (TPM) of chemokine gene expression related to CD8⁺ T cell recruitment in epidermal keratinocytes (n = 3 mice per group, two-way ANOVA).

(legend continued on next page)

(D) CXCL16 expression in epidermal keratinocytes in control and sympathetic-ablated mice (n = 6 skin areas, two-tailed unpaired t test).
(E) Western blot of CXCL16 in epidermal keratinocytes.
(F) CXCL16 expression in epidermal keratinocytes in K14-Adrb2 cKO mice (n = 6 skin areas, two-tailed unpaired t test).
(G) Dot plot of *Cxcl16* expression in skin epithelial cell subsets from scRNA-seq analysis.
(H) MFI quantification of CXCL16 expression in skin epidermis (n = 6 skin areas per group, two-way ANOVA).
(I) CXCL16 expression in fibroblasts, endothelial cells, and DCs (n = 5–12 skin areas per group, two-way ANOVA).
(J) Flow cytometric quantification of CXCR6 in the skin immune cell subsets (n = 4 mice per group, two-way ANOVA).
(K) Epidermal CXCL16 expression in Gi-DREADD mice after CNO administration (n = 7–12 skin areas per group, one-way ANOVA).
(L and M) Flow cytometry analysis of skin *Cxcr6*$^{-/-}$ GFP^{+} and wild-type (WT) tdTomato^{+} CD8^{+} T cells.
(N) RT-qPCR of T_{RM} development genes in human keratinocytes treated with saline or nadolol (n = 3 replicate treated wells per group, two-way ANOVA).
(O) CD8^{+} T cells and CXCL16 expression in the lung airways of control and Gi-DREADD mice (n = 27–36 areas from 5 mice per group, two-tailed unpaired t test).
Bar graphs show mean ± SD; violin plots show distributions with individual points; lines indicate the median and interquartile range; $^{*}p < 0.05$, $^{**}p < 0.01$, $^{***}p < 0.001$; n.s., not significant.

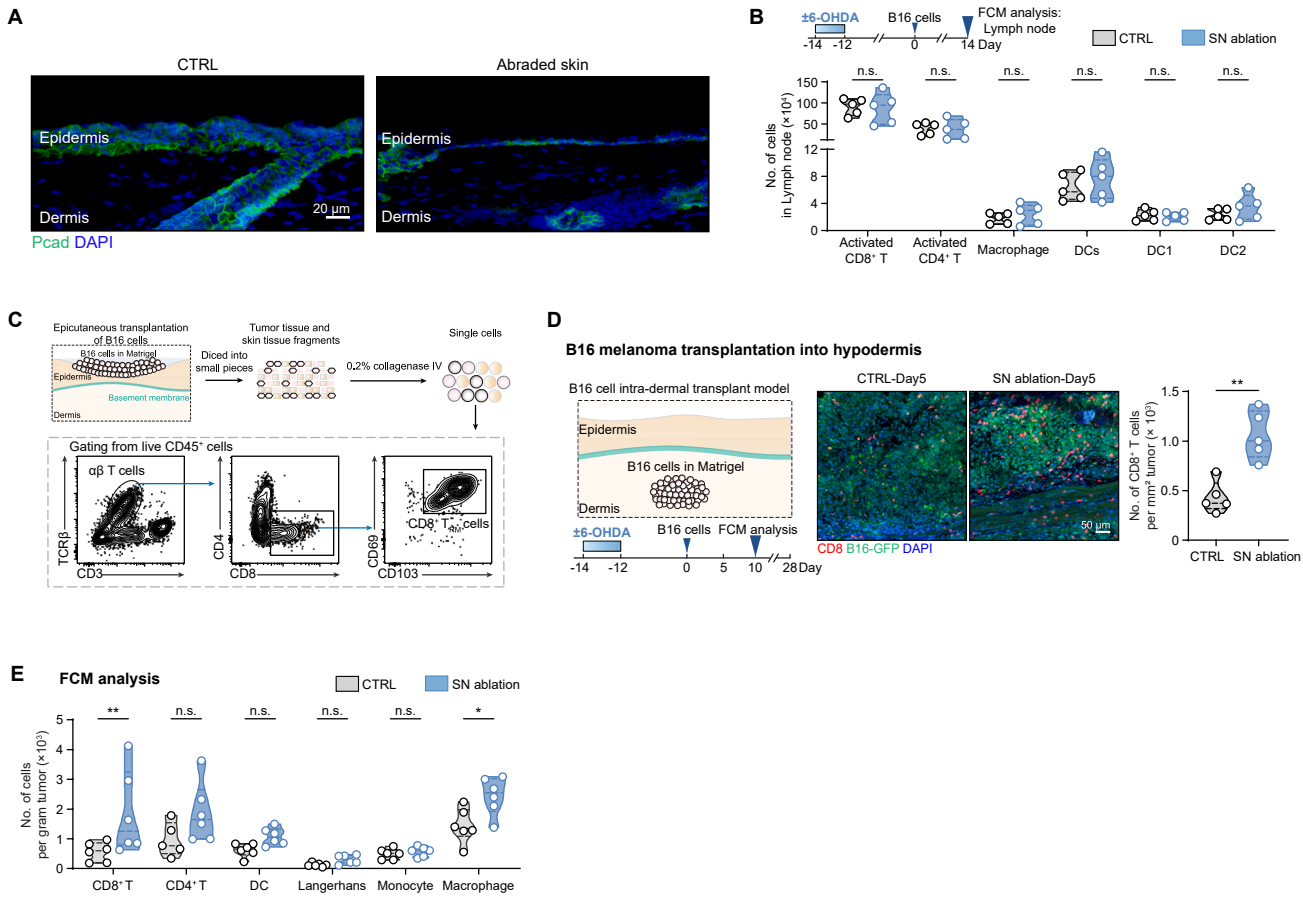

Figure S6. Sympathetic inhibition enhances local cancer immunosurveillance in skin, related to Figure 6

(A) Skin abrasion for epicutaneous transplantation.

(B) Immune profiling of lymph nodes in control and SN-ablated mice with B16 epicutaneous transplantation (n = 5 mice per group, two-way ANOVA).

(C) Flow cytometry workflow.

(D) CD8$^+$ T cells in control and SN ablation mice with B16 dermal transplantation (n = 5 tumor areas, two-tailed unpaired t test).

(E) Immune profiling of control and SN-ablated mice with B16 dermal transplantation (n = 5–6 mice, two-way ANOVA).

Violin plots show distributions with individual points; lines indicate the median and interquartile range; *p < 0.05, **p < 0.01; n.s., not significant.

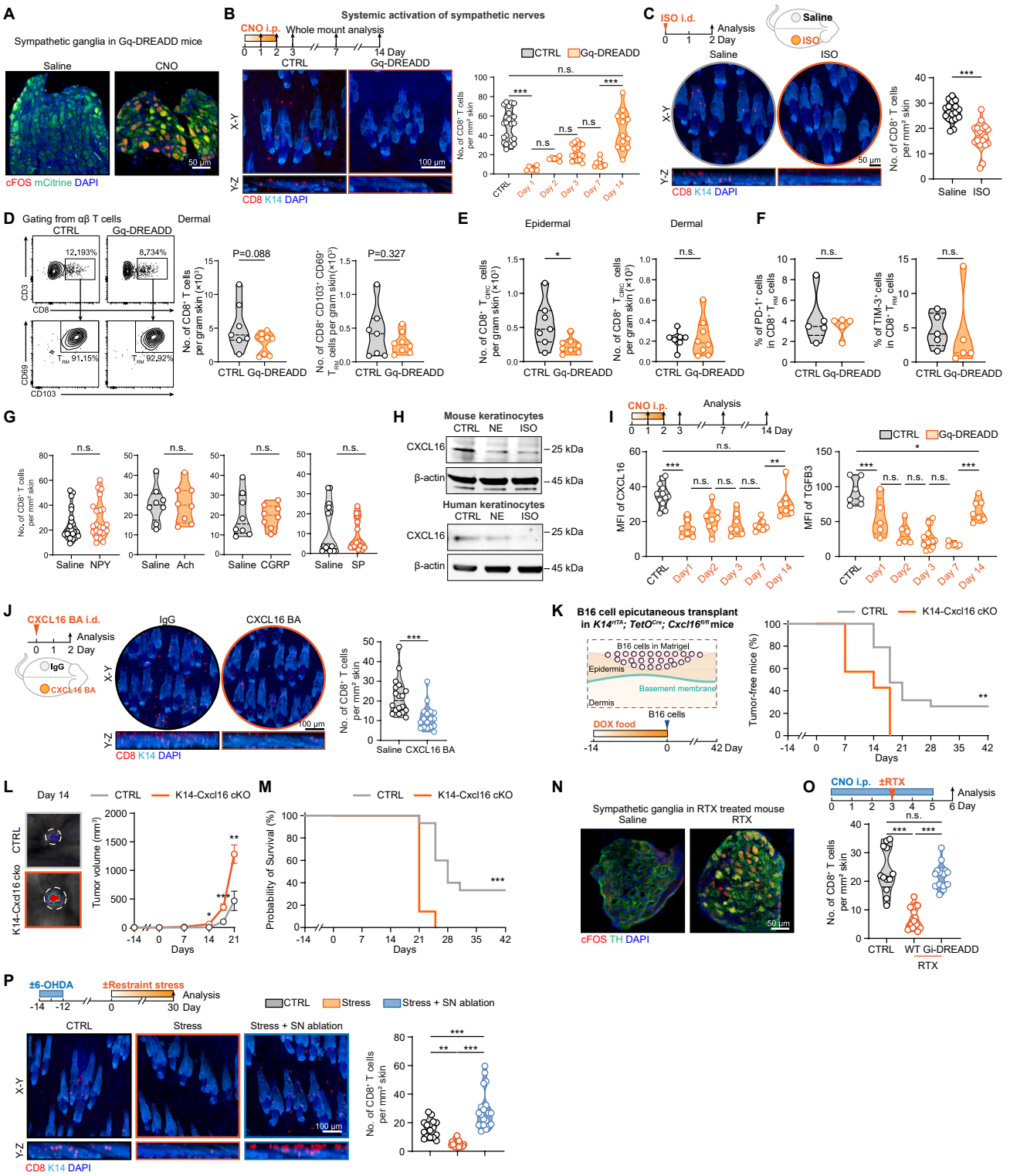

Figure S7. Heightened sympathetic signaling attenuates skin CD8$^+$ T_{RM} cell formation, related to Figure 7

(A) cFOS in sympathetic ganglia of Gq-DREADD mice with saline or CNO treatment.

(B) Skin CD8$^+$ T cells in control and Gq-DREADD mice following CNO administration (n = 6–23 skin areas, one-way ANOVA).

(C) Skin CD8$^+$ T cells after isoprenaline hydrochloride (ISO) and saline intradermal treatment (n = 18 skin areas from 3 mice per group, two-tailed unpaired t test).

(legend continued on next page)

(D) Representative flow cytometry plots and quantification of dermal $CD8^+$ T and T_{RM} cells in control and Gq-DREADD mice (n = 7–8 mice per group, two-tailed unpaired t test).
(E and F) Flow cytometric quantification of T_{CIRC} and PD-1^+ and TIM-3^+ $CD8^+$ T cells in control and Gq-DREADD mice (n = 5–8 mice per group, two-tailed unpaired t test).
(G) Skin $CD8^+$ T cells after intradermal injection of Neuropeptide Y (NPY), acetylcholine (Ach), CGRP, and substance P (SP, n = 8–22 skin areas per group, two-tailed unpaired t test).
(H) Western blot of CXCL16 in mouse and human cultured keratinocytes treated with saline, NE, or ISO.
(I) Epidermal CXCL16 and TGFB3 expression in Gq-DREADD mice after CNO administration (n = 5–14 skin areas per group, one-way ANOVA).
(J) Skin $CD8^+$ T cells after intradermal CXCL16 BA and IgG injection (n = 17–18 skin areas from 3 mice per group, two-tailed unpaired t test).
(K–M) Tumor-free incidence (K), bioluminescence images with tumor growth curves (L), and Kaplan-Meier survival curves (M) in control and K14-Cxcl16 cKO mice with B16 epicutaneous transplantation (n = 7–19 mice per group, log-rank Mantel-Cox test or two-tailed unpaired t test).
(N) cFOS in sympathetic ganglia of saline- or RTX-treated mice.
(O) Skin $CD8^+$ T cells in control and Gi-DREADD mice with RTX treatment (n = 12–17 skin areas from 2–4 mice per group, one-way ANOVA).
(P) Skin $CD8^+$ T cells in control and restraint stress mice with 6-OHDA treatment (n = 16–21 skin areas from 3–4 mice per group, one-way ANOVA).
In (L), mean ± SEM; all other panels, violin plots show distributions with individual points; lines indicate the median and interquartile range; $^*p < 0.05$, $^{**}p < 0.01$, $^{***}p < 0.001$; n.s., not significant.